Impacts of Meteoric Material on Earth’s Atmosphere

Laboratory Studies with Atmospheric Implications

Alexander James

Submitted in accordance with the requirements for the degree of
Doctor of Philosophy

The University of Leeds
School of Chemistry

September 2016

The candidate confirms that the work submitted is his own, except where work which has formed part of jointly-authored publications has been included. The contribution of the candidate and other authors to this work has been explicitly indicated below. The candidate confirms that appropriate credit has been given within the thesis where reference has been made to the work of others.

Acknowledgements

There are a lot of people without whom this work would not have been possible. An attempt has been made to thank them each here. To my supervisors Prof. John M. C. Plane and Prof. Benjamin J. Murray, who instigated the work and who have been supportive throughout I would like to say a huge thank you. I don’t think I can imagine a better balanced supervisory team, asking those probing and insightful questions, giving advice and putting your collective feet down from time to time. I am very grateful for the funding, the time and the chance to pursue this research topic, to collaborate with a wide range of scientists, both local and internationally renowned, on the CODITA project.

To all the other researchers which whom I have collaborated (in Leeds: Juan Carlos, David, James, Vicki, Russell, Wuhu, Tamsin, Theo, Daniel O’Sulivan, Sam, Anna, Erin, Juan Diego, Hannah Price, Pascale, Daniel Moon, Tom Mangan, Tasha and at other institutions: Prof. Hinrich Grothe and co-workers, Dr Ralf Weigel, Dr Robert Wagner, Dr Martin Schnaiter, Prof. Ottmar Moehler and co-workers, Dr Josep Trigo-Rodriguez and co-workers). I would like to thank you for sharing your experience, insights, facilities and time with me. I have met many interesting, knowledgeable and inspiring people throughout my PhD and am grateful to them all. To those who gave me technical support (in particular: Dr Algy Kazlauciunas, Dr Alexander Kulak, Mrs Lesley Neve and Dr Mike Ward) I would like to express a similar thanks. Leeds has been a good place to work, with a professional yet friendly atmosphere.

I’m particularly grateful to Sam, Anna, Erin, Juan Diego, Tom and Tasha (and all the other PhD students) for being in it together. It’s nice to know there’s always at least one other person around who can empathise and sympathise with whichever challenges you’re meeting. I would also like to thank the post docs with whom I’ve worked, JC and Mark Blitz for their incredible breadth of informed and personal advise, Vicki for getting through it together, David Bones for being a wonderful human being and James for putting up with me bothering him all the time.

To my dear Ruthy and my many friends in Leeds I would like to say that you have been an invaluable part of the process. No-one ever claims that a PhD will be easy but there are times when emotional support, be that dinners cooked, days out or a simple cup of tea or pint of beer shared are the only thing that will get you through. I can honestly say that the people around me have carried me through the process and deserve a lot of the credit for the completion of this work. I think the many strong relationships I have formed outside and around work have been the real reason why I made it through my time here and why I now consider Yorkshire to be at least as much my home as Scotland.

My family – Mum, Dad, Ruby and the various aunts, uncles and cousins – who have been there for me throughout my life deserve many many mentions. For shaping the person I am, helping me get through life and for putting up with the weird scientist that I am; thank you. Seeing you each go through your own challenges in life, overcome them and still have time for a blether when it’s needed is always an inspiration.

My own contributions and those of other researchers, fully and explicitly indicated in the thesis, have been:

In synthesising the IDP and MSP analogues (Chapter 2):

- Sourcing and grinding meteorites and terrestrial minerals.
- Synthesising and characterising candidate analogues for MSPs (Initial work was performed by Drs Russell Saunders and Victoria Frankland).
- Characterising these analogues by electron microscopy (assisted by Victoria Frankland, Mike Ward, Algy Kazlauciunas and Alex Kulak) X-ray Diffraction (assisted by Lesley Neve) and all other techniques mentioned in Chapter 2.
- Interpretation of the results, comparison to the literature and targeting of analogue materials was carried out in extensive collaboration with Juan Carlos Gomez-Martin.

In measuring and implementing kinetics of reactive uptake (Chapter 3):

- These laboratory studies were led by Victoria Frankland (HNO_3), Pascale Lakey and Daniel Moon (HO_2) My contributions were in providing samples of MSP analogues and assisting with data analysis and interpretation of the results of experiments.
- The global model was set up and run by Wuhu Feng. My contribution was to interpret output, producing figures and discussion of the results.

In measuring kinetics of nucleation relevant to polar stratospheric clouds (Chapter 4) I performed all laboratory experiments, carried out data analysis, developed and interpreted the 1-D box model.

Throughout these studies I was supervised, managed and directed by Profs John Plane and Ben Murray.

Abstract

Analogues were developed for Interplanetary Dust Particles (IDPs) and Meteoric Smoke Particles (MSPs). Candidate materials were characterised and compared to the present understanding of the nature of IDPs and MSPs. Knowledge and understanding from meteoritics was used to inform open questions in atmospheric chemistry. The elemental composition, structural, surface and size distribution properties of the candidates was compared to micrometeorites and remote measurements of MSPs. Both relatively rare carbonaceous and the more common ordinary chondritic meteorites and terrestrial minerals were shown to be useful analogues for IDPs, whilst synthetic materials were identified as analogues for MSPs.

Uptake of HNO_3 and HO_2, based on laboratory experiments, was implemented in a global modelling study. The uptake processes were assessed to determine the region(s) and season(s) in which they would affect atmospheric chemistry. This heterogeneous chemistry augmented previous understanding of gas-phase chemistry, with a view to understanding all sources and sinks of atmospheric species. Whole Atmosphere Community Climate Model (WACCM) runs including uptake were compared to control runs with only gas-phase chemistry. Uptake of both HNO_3 and HO_2 was shown to alter chemistry in the polar vortex, including effects on many secondary species and feedbacks on each other.

Heterogeneous nucleation kinetics of nitric acid hydrates in Polar Stratospheric Clouds (PSCs) was investigated in the laboratory. SiO_2 particles were used as analogues for MSPs processed in acidic solution and the phase which formed was investigated. A newly developed drop freeze assay capable of quantifying heterogeneous nucleation kinetics was used. Nucleation events observed in µl droplets were parameterised using current theoretical models and the results compared to atmospheric observations. The measured heterogeneous nucleation kinetics of the Dihydrate, which then readily converts to the Trihydrate, on SiO_2 were shown to be capable of explaining the concentrations of crystals observed in the atmosphere.

Table of Contents

List of Tables

List of Figures

List of Abbreviations

Abbreviation	Term	Description
BET	Brunauer, Emmet & Teller theory	A method used to determine the specific surface area (m^2 g^{-1}) of a material
CAI	Calcium Aluminium Inclusions	Phases present in some meteorites, rich in Ca and Al
CARMA	Community Aerosol and Radiation Model for Atmospheres	A model of aerosol and radiative properties
CC	Carbonaceous Chondrites	Chondritic Meteorites containing significant carbon
CI	Carbonaceous Ivuna	meteorites with a composition similar to the Ivuna chondrite
CM	Carbonaceous Mighei	meteorites with a composition similar to the Mighei chondrite
CNT	Classical Nucleation Theory	A theoretical framework which describes kinetics of nucleation
CPC	Condensation Particle Counter	An instrument which measures the concentration of aerosols in a gas flow
(h-)DFT	(hybrid) Density Functional Theory	A method of calculating energetically optimal molecular structures
EDX	Energy Dispersive X-Ray spectroscopy	A method used to determine the elemental composition of a material
FAGE	Fluorescence Assay by Gas Expansion	A technique for measuring concentrations of OH or HO_2 radicals
FROST	Framework for Reconciling Observable Stochastic Time dependence	A theoretical method for modelling the time dependence of nucleation

GEOS	Goddard Earth Observing Systems model	A global model of atmospheric dynamics and meteorology
IDP	Interplanetary Dust Particle	Dust grains which exist in our solar system
INP	Ice Nucleating Particle	A particle which can increase the probability of ice nucleation
MIF	Meteor Input Function	A description of the size, velocity and total mass of material which enters the Earth's atmosphere from space
MLS	Mesospheric Limb Sounder	A radiometer aboard the AURA satellite
NAD	Nitric Acid Dihydrate	A crystalline material containing one molecular equivalent of HNO_3 and two of H_2O
NAM	Nitric Acid Monohydrate	A crystalline material containing one molecular equivalent of HNO_3 and one of H_2O
NAT	Nitric Acid Trihydrate	A crystalline material containing one molecular equivalent of HNO_3 and three of H_2O
NAX	Arbitrary Nitric Acid hydrate	A crystalline material containing one molecular equivalent of HNO_3 and arbitrary H_2O
NWA	The North West Africa-5515 meteorite	A CK4 body found in Algeria in 2007.
OC	Ordinary Chondrites	Chondritic Meteorites with low carbon content
PSC	Polar Stratospheric Cloud	Iridescent clouds which form in the polar stratosphere during winter
QMS	Quadropole Mass Spectrometer	An instrument used for separating and detecting chemical species

SEM	Scanning Electron Microscopy	A technique used to image features on the 100s nm to µm scale
SMPS	Scanning Mobility Particle Sizer	An instrument for measuring the concentration and (by separating by mass and charge) size distribution of aerosols
STS	Stratospheric Ternary Solution	Droplets of $HNO_3/H_2O/H_2SO_4$ which form in the stratosphere during winter
TEM	Transmission Electron Microscopy	A technique used to image features on the nm scale
TMI	Transition Metal Ions	transition metal ion complexes in aqueous solution
UoL	University of Leeds	Where much of the work contained in this thesis was carried out
(SD-) WACCM	(Specified Dynamics-) Whole Atmosphere Community Climate Model	A global model of atmospheric chemistry, dynamics can be constrained to improve reproducibility
XRD	X-Ray Diffraction	A technique for measuring the crystal structure of materials

Chapter 1

Introduction: Atmospheric Processes Involving Meteoric Material

This chapter sets out the current understanding of processes involving meteoric material as it travels through Earth's atmosphere to the surface (summarised in Figure 1.1) and poses related science questions which are discussed in the following chapters.

On atmospheric entry some Interplanetary Dust Particles (IDPs) ablate, both through sputtering and frictional heating, releasing constituents into the gas phase. Those IDPs which do not ablate completely sediment rapidly to the surface. Material which ablates is chemically transformed into Meteoric Smoke Particles (MSPs). These are aerosol particles small enough (<100 s nm radius) that they do not sediment gravitationally but are transported by the residual atmospheric circulation. This transport carries MSPs down the winter polar vortex, where they take up HNO_3, HO_2 (catalysing production of H_2O_2), and H_2SO_4. In the stratosphere, MSPs are entrained into (and at least partially dissolve in) acidic liquid droplets (Junge layer aerosol) either by taking up H_2SO_4 and H_2O or by colliding with existing droplets. At low temperatures these droplets take up more H_2O and HNO_3 and form crystalline solids, likely through heterogeneous nucleation on MSP surfaces. The crystals then grow by taking up more HNO_3 and H_2O and sediment to lower altitudes, causing denitrification of the stratosphere and transporting MSPs to the troposphere and ultimately to the Earth's surface.

This chapter introduces each of these processes and poses science questions which are addressed in the following chapters.

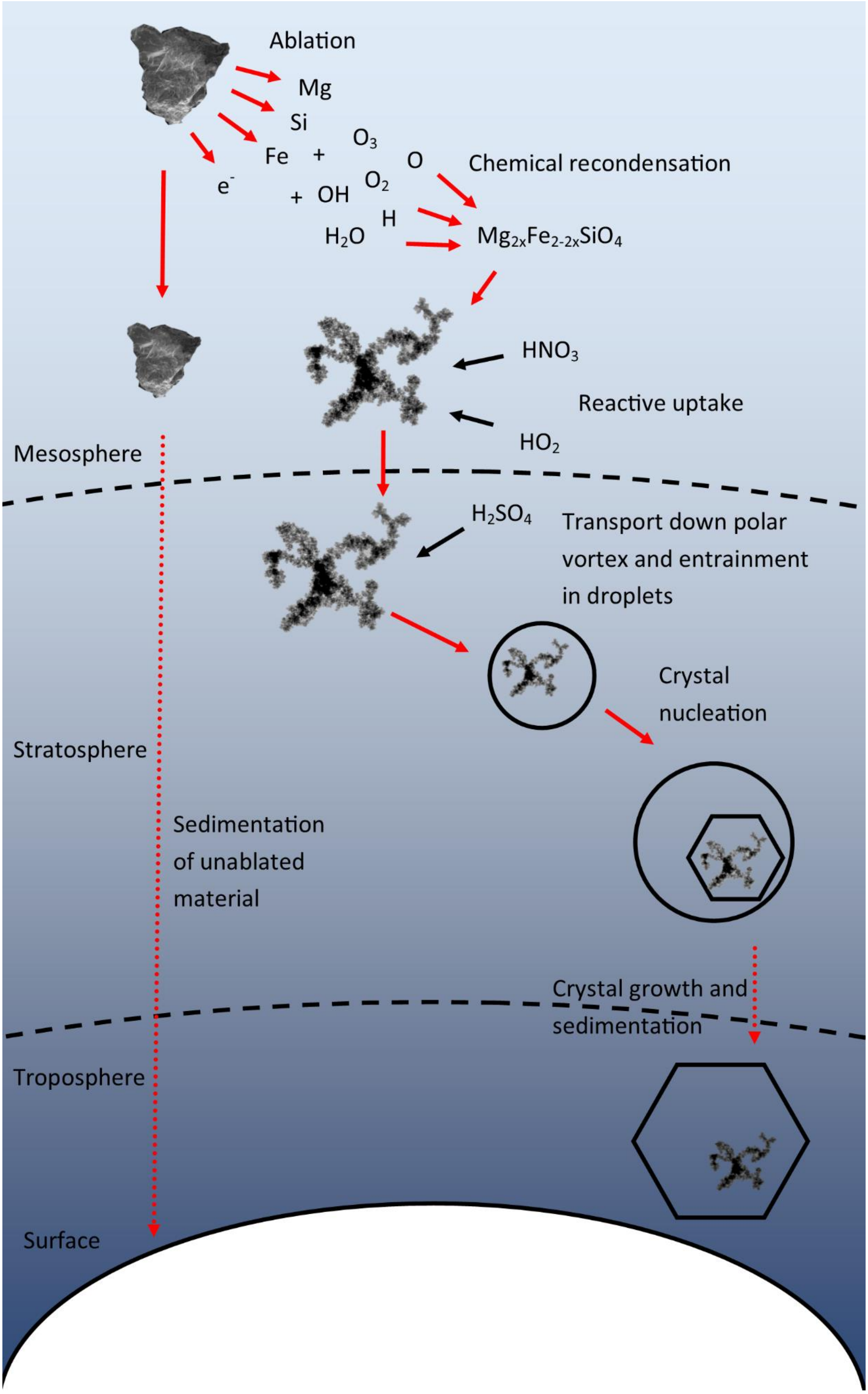

Figure 1.1: Summary of processes involving meteoric material as it travels to the Earth’s surface.

1.1 Interplanetary Dust; Content and Composition, Meteoric Ablation and Recondensation

The majority of Interplanetary Dust Particles (IDPs), which produce meteors (sometimes visible in the night sky) when they enter the Earth’s atmosphere, come from the Jupiter family comets (≥90 %) and the asteroid belt or Oort cloud comets (≤10 %) with a minor contribution from Halley-type comets [*Nesvorný et al.*, 2011; *Nesvorný et al.*, 2010]. IDPs from these sources are slowed (their orbits are circularised by Poynting-Robertson drag) and then gravitationally drawn toward the inner solar system. Those which reach Earth mostly have radii from 10-50 μm (0.01 to 1 μg mass assuming 3 g cm^{-3} density) [*Carrillo-Sánchez et al.*, 2015; *Nesvorný et al.*, 2011]. Cometary and asteroidal IDPs would differ mostly in that cometary dust would be expected to be have a greater degree of H_2O processed minerals such as phyllosilicates.

Most of the information available regarding the content and composition of IDPs comes from studies of material collected from melted polar snowpack [*Maurette et al.*, 1987; *Taylor et al.*, 1998], deserts [*Kohout et al.*, 2014], ocean sediments and stratospheric flights [*Blanchard et al.*, 1980; *Rietmeijer*, 2000; *Zolensky and Lindstrom*, 1992]. Particles collected at the surface are generally termed Micro-Meteorites (MMs) whilst those retrieved from the stratosphere are more commonly referred to as IDPs, however both are thought to originate from the same extra-terrestrial sources.

Particles collected from these locations show differing levels of thermal processing related to atmospheric entry and weathering by the terrestrial environment [*Taylor et al.*, 2012]. These range from unmelted particles, which contain mineral grains with nm to 10s μm diameters, to cosmic spherules which have melted to a significant extent but not completely evaporated. The surfaces of MMs can be processed, mainly by hydrolysis reactions at the high pressures experienced in polar ice caps. Nevertheless, the large sample sizes available allow statistically reasonable statements to be made regarding the nature and origins of IDPs in general [*Jessberger et al.*, 2001; *Kohout et al.*, 2014; *Taylor et al.*, 2012]. *Taylor et al.* [2012] examined more than 5000 MM particles recovered from the South Polar Water Well in the year 2000 and found that ~75 % of these were fine grained aggregates of Carbonaceous Ivuna (CI-) or Carbonaceous Mighei (CM-) chondritic elemental composition, 10 % were coarse grained (>10s μm scale) anhydrous minerals and <10 % were Ordinary Chondrites (OCs). Less than 1 % of these MMs had achondritic compositions, Calcium Aluminum Inclusions (CAIs) or recognisable chondrules. The porosity of IDPs is similar to Carbonaceous Chondrite meteorites (CCs) (bulk density ~2 g cm^{-3} [*Jessberger et al.*, 2001]), however those of OCs are rather higher (>3 g cm^{-3}), since these have undergone mild metamorphism which reduces porosity [*Consolmagno et al.*, 2008].

Complimentary information has been obtained from extra-terrestrial observations and capture and return missions. Such studies are limited in that they typically examine only a single parent body (asteroid or comet) and may therefore not represent the variability present in sources of IDPs. Exceptions include the Long Duration Exposure Facility (LDEF), which used impact features on Al plates which were exposed to space in near Earth orbit for over 5 years to determine a size distribution for incoming material based on an assumed velocity distribution [*Love and Brownlee*, 1993], and particles captured in aerogel aboard the MIR space station [*Hörz et al.*, 2000]. Studies of single parent bodies have yielded some interesting results; the comet 81P/Wild 2 has a near CI composition [*Rietmeijer*, 2015] whilst 67P/Churyumov-Gurasimenko has an Fe/Na ratio enriched with respect to CI by a factor of 1.5 to 15 [*Hilchenbach et al.*, 2016], 9P/Tempel 1 ejecta also shows good agreement with solar or CC composition [*Lisse et al.*, 2006]. These observations of single bodies by a variety of techniques (capture and return atomic spectroscopy, in-situ atomic spectroscopy and remote infra-red emission spectroscopy respectively) are in good general agreement with the terrestrial observations.

Those IDPs which reach the Earth's atmosphere are frictionally heated according to their mass, velocity and entry angle with respect to the zenith [*Vondrak et al.*, 2008]. IDPs then lose mass; partially by molecular sputtering but mainly because the melting point of constituent phases is reached and material is able to diffuse to the molten surface and evaporate. More volatile elements such as Na and K are lost first, a process known as differential ablation [*Janches et al.*, 2009]. Unablated particles are large enough that they rapidly sediment to the surface, whilst ablated material remains in the mesosphere to take part in atmospheric chemistry.

The mass flux of IDPs to the Earth's atmosphere is highly uncertain, with estimates ranging from several to several hundred metric tons per day (t d^{-1}) [*Plane*, 2012]. A number of atmospheric processes not previously studied could be used to constrain this flux, known as the Meteoric Input Function (MIF).

Atmospheric chemistry of meteoric metals involves Fe, Mg, Na, K, Ca and Si (and other metals) along with atmospheric constituents such as O_3, O_2, H_2O and CO_2 and has been recently reviewed by *Plane et al.* [2015]. Example chemical schemes are shown in Figure 1.2 for Fe and Na containing species.

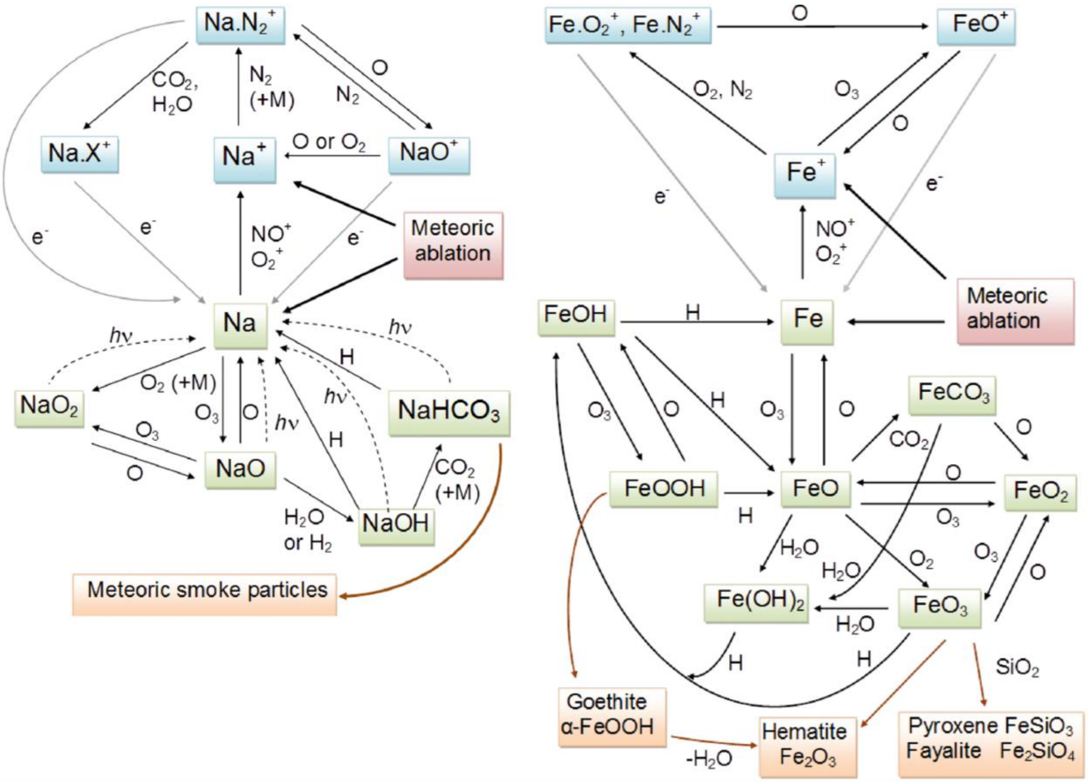

Figure 1.2: Chemical schemes showing interactions between metal species (Na and Fe) produced from meteoric ablation and how they come to produce meteoric smoke particles. Reproduced from *Plane et al.* [2015].

In general, the interplay of a wide variety of reactions leads to layers of neutral atomic metals, with ionic species prevailing above and stable molecular reservoirs below. One important process which produces links between these various schemes is the hydrolysis of SiO_2 to sililic acid ($Si(OH)_4$), as shown in Figure 1.3, which can then undergo dehydration reactions with metal hydroxides to produce metal silicates. For example the reaction of $Si(OH)_4$ with FeOH is exothermic by 21 kJ mol^{-1} [*Plane et al.*, 2016].

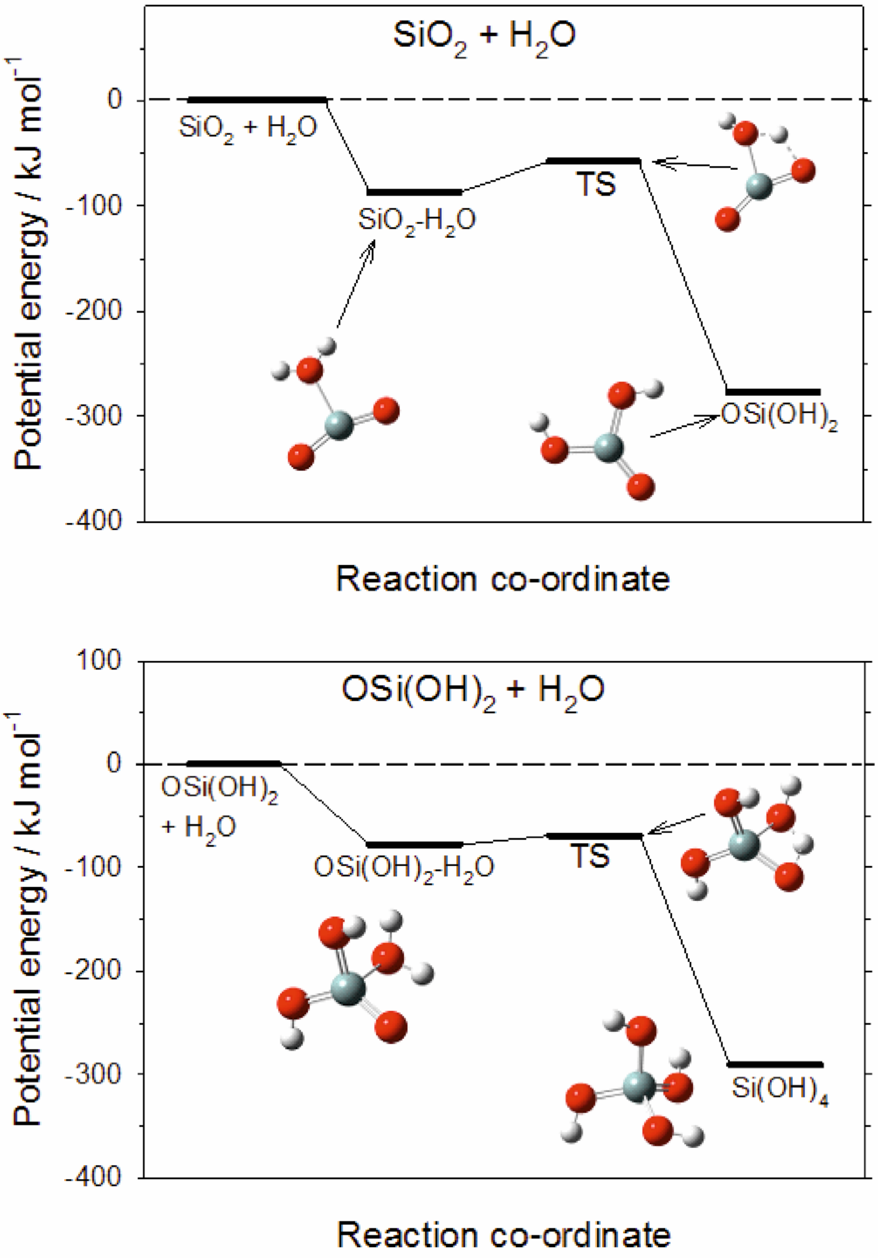

Figure 1.3: Potential energy surface for hydrolysis of SiO_2 to $Si(OH)_4$ calculated with the Gaussian 09 suite of programs [*Frisch et al.*, 2009]. Molecular geometries were optimised using hybrid Density Functional Theory (h-DFT). The B3LYP method with the 6-311+G(2d,p) triple zeta basis set was used. The resulting rotational constants and vibrational frequencies were then used in master equation calculations to calculate potential energy changes, which were further improved (to ±15 kJ mol^{-1}) using the complete basis set method [*Montgomery et al.*, 2000]. Both steps in the hydrolysis are found to be exothermic by nearly 300 kJ mol^{-1}. Reproduced from [*Plane et al.*, 2016].

These molecular species including silicates, oxides and carbonates can then polymerise to produce meteoric smoke particles (MSPs). These have yet to be collected and characterised fully [*Hedin et al.*, 2014], however they have been observed remotely and in *situ* [*Hervig et al.*, 2009; *Plane et al.*, 2014; *Rapp et al.*, 2012; *Robertson et al.*, 2014]. Whilst these studies can inform the composition of MSPs [*Hervig et al.*, 2012], only laboratory work has given any insight into the likely morphology of these particles, which is crucial for examining their surface properties [*Saunders and Plane*, 2006]. The current hypothesis, supported by these laboratory studies, is that molecules add to primary aerosols until at some radius these primary aerosols grow faster by agglomeration than by condensation. This leads to aerosol with a fractal, soot-like morphology which in the atmosphere is transported by the residual atmospheric circulation toward the winter polar vortex and down into the stratosphere [*Bardeen et al.*, 2008; *Dhomse et al.*, 2013].

In order to assess the impact of IDPs and MSPs on the atmosphere it is necessary to produce surfaces which are chemically analogous. In the literature, a variety of materials have been employed to investigate a wide range of processes. For example, samples of several well characterised CCs along with various terrestrial minerals have been used to examine the impact on IDPs of capture in low density silicon and of atmospheric entry [*Burchell et al.*, 2006; *Court and Sephton*, 2011; *Toppani et al.*, 2001].

Although ground CC samples are often used as analogues for IDPs, the fine grained nature of MMs (and IDPs) is significantly different to CCs, which are composed of µm scale grains of mineral aggregates, single minerals, chondrules etc. [*Jessberger et al.*, 2001]. This means that, even though the bulk composition of IDPs closely resembles CI or CM meteorites, individual particles of ground meteorite samples will frequently not represent the composition of IDPs. Chapter 2 of this thesis will examine materials which can be used as analogues for IDPs and MSPs in a variety of applications.

1.2 Meteoric Smoke; Perturbations to Gas-Phase Species

The growth, transport and deposition of MSPs has been investigated by a variety of modelling studies [*Bardeen et al.*, 2008; *Dhomse et al.*, 2013; *Saunders et al.*, 2007]. It is common to assume that the fractal morphology can be well represented by a distribution of spherical particles in bins of geometrically increasing radius, agglomerating collisionally. This has obvious implications for the available surface area of MSPs, but also affects their optical and dynamical (transport) properties. *Saunders et al.* [2007] demonstrated that including the fractal nature of particles in a 1D atmospheric simulation significantly changed their atmospheric abundance. As shown in Figure 1.4, fractal particles are effectively less dense than spherical particles of the same mass and therefore sediment more slowly. This results in increased concentrations of MSPs in the middle atmosphere.

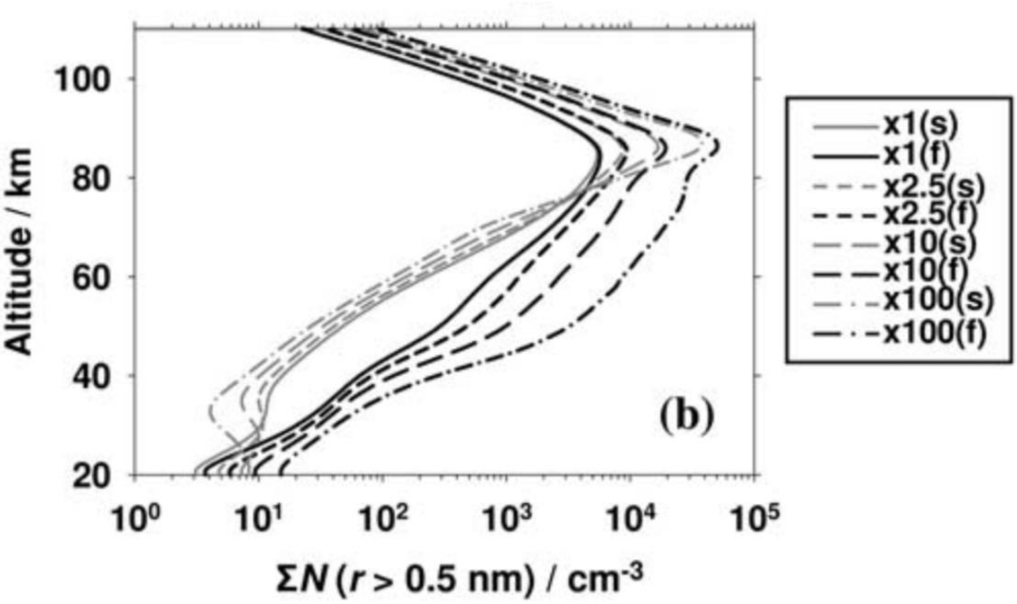

Figure 1.4: Difference in total number concentration of MSPs (>0.5 nm radius) considering fractal (f) or spherical (s) particles. Various scenarios are shown representing different total mass input of ablated meteoric material (factor shown × 44 t d^{-1}). Reproduced from *Saunders et al.* [2007].

The extinction due to fractal aerosol can be treated using refractive indices given by the volume average of the refractive indices of the aerosol primary spheres and the medium, which in this case is air [*Sorensen*, 2001]. The resulting changes to extinction are rather complex since a spherical particle will have a smaller diameter but higher effective (volume averaged) refractive index than a fractal particle of the same mass. Because MSPs have not yet been collected for analysis [*Hedin et al.*, 2014], there is no constraint available on the volume filling properties (fractal dimension, D_f) of MSPs and since introducing this degree of freedom would have a significant impact on computational efficiency, spherical approximations - with appropriate caveats - remain commonplace [*Bardeen et al.*, 2008; *Frankland et al.*, 2015; *Neely et al.*, 2011].

Models of MSP transport allow researchers to investigate their interactions with chemical constituents in an atmosphere. Uptake, the simplest of these interactions, of H_2SO_4 onto MSPs has been suggested as a route for the formation of Junge layer aerosol and as an explanation of anomalous extinction observed in the upper stratosphere [*Neely et al.*, 2011; *Saunders et al.*, 2012]. Molecules which are taken up onto particle surfaces can also go on to react, with the MSPs effectively catalysing slow reactions. For example, *Summers and Siskind* [1999] proposed that the MSP-catalysed reaction of O with H_2 could be a significant source of H_2O in the mesosphere. Open questions which will be addressed in this thesis include the interaction of HNO_3, which is produced by auroral precipitation [*Verronen et al.*, 2011], and HO_2 with MSPs.

Modelling studies have shown that gas-phase chemistry alone cannot reproduce observations of HNO_3, particularly when solar proton events occur [*Funke et al.*, 2011; *Jucks et al.*, 1999; *Kvissel et al.*, 2012]. To fully understand any species' concentration it is necessary to understand all pathways for production and loss of that species. Recent progress has been made on the auroral production pathway of HNO_3 [*Verronen et al.*, 2016]; however, this introduces significant HNO_3 into the mesosphere where, in the absence of sunlight, uptake to MSPs may be a significant loss pathway.

An uncertainty is also outstanding in the abundance of HO_x species (defined in Figure 1.6) in the mesosphere, known as the HO_x dilemma [*Millán et al.*, 2015]. This is shown in Figure 1.5, where measurements of atmospheric HO_2 from the Mesospheric Limb Sounder (MLS) radiometer are compared to simulations from the Whole Atmosphere Community Climate Model with Specified Dynamics (SD-WACCM). Several studies have attempted to explain this discrepancy with modifications to gas phase chemistry schemes. *Siskind et al.* [2013] showed that increasing the rate coefficient for the reaction of H with O_2, producing HO_2, by a factor of 1.5 (which is within the error bounds of measured rates) improved agreement between modelled and measured OH abundance but did not present a comparison for HO_2. *Pickett et al.* [2008] showed that for northern hemisphere summer, rate constants within the stated error of the JPL 2006 recommendation could explain the observed HO_2 but did not discuss seasonal trends. To the author's knowledge, no study has thus far assessed whether uptake to and/or reaction on MSPs could significantly impact the mesospheric HO_x budget.

Since Figure 1.5 shows that WACCM currently underestimates HO_2 abundance our intention is to determine whether uptake to MSPs is an important loss process rather than to suggest that including uptake alone will improve the agreement. In fact uptake of other species such as HNO_3 – and subsequent indirect chemical effects on HO_2 – could improve the agreement between model and observations.

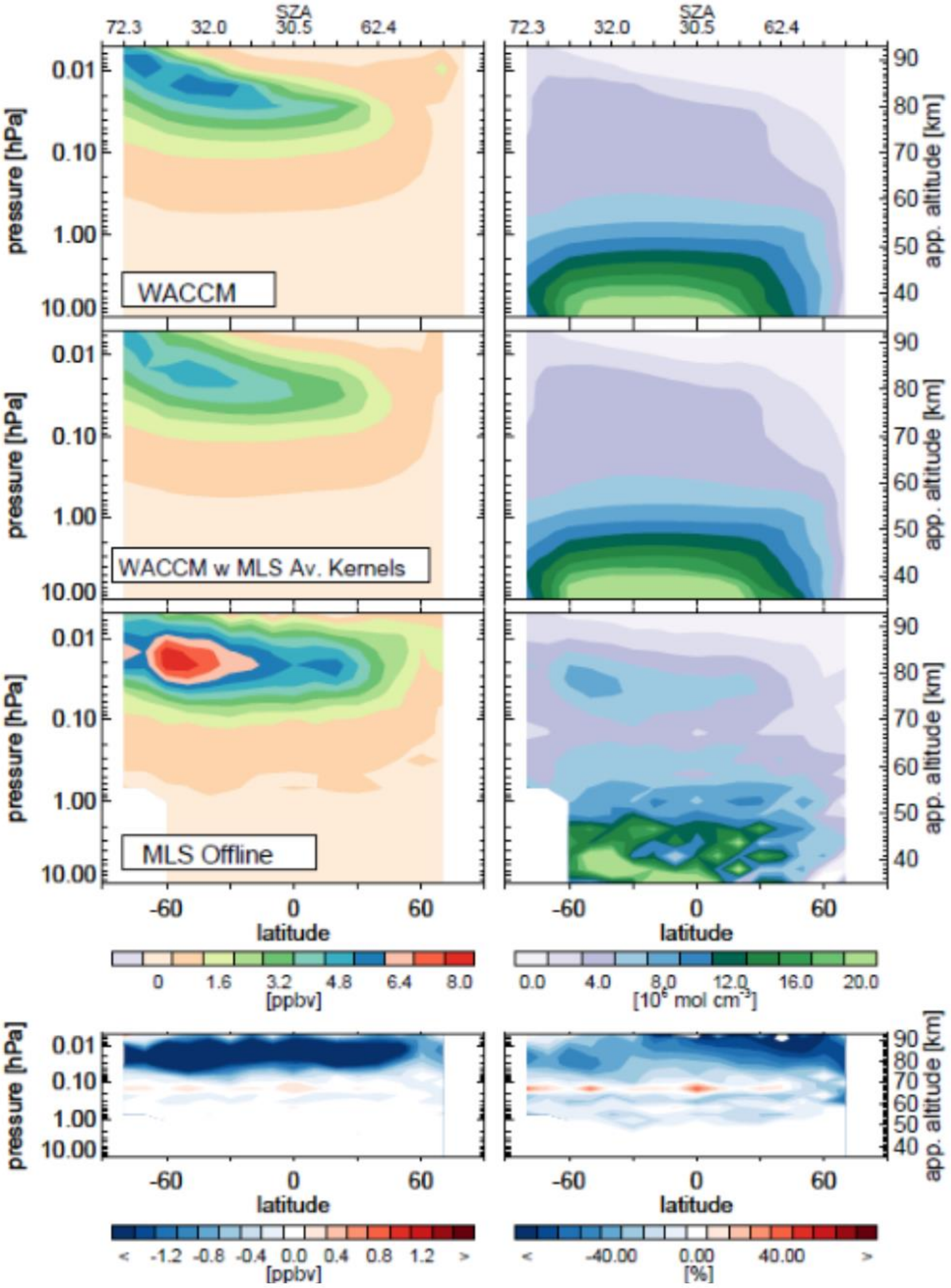

Figure 1.5: Zonal and monthly mean Atmospheric HO_2 for January 2005 as simulated in SD-WACCM (top two panels), as measured by MLS (third panels) and difference (bottom panels) in terms of mixing ratio (left panels) and concentration (right panels). There is clearly a significant flaw in our understanding of mesospheric HO_2. Reproduced from *Millán et al.* [2015].

Figure 1.6 summaries the chemistry of NO_x (oxidised nitrogen compounds, including HNO_3) and HO_x in the middle atmosphere, including the primary gas phase production and destruction pathways of HNO_3 and HO_2 (for definitions of rate constants and term symbols shown in Figure 1.6 see *Brasseur and Solomon* [1998]).

When the atmosphere is unperturbed by solar protons, HNO_3 is produced by reaction of NO_2 with OH:

$$NO_2 + OH \rightarrow HNO_3 \qquad (R1.1)$$

and removed by photolysis, reaction with OH and transport (either gas phase or by sedimentation of condensed phase particles, see Section 1.3):

$$HNO_3 + OH \rightarrow NO_3 + H_2O \qquad (R1.2)$$

$$HNO_3 + h\nu \rightarrow NO_2 + OH \qquad (R1.3)$$

where $h\nu$ represents a photon. Since OH is a photoproduct, this means that HNO_3 is both produced and destroyed in the presence of sunlight.

HO_2 is produced by reaction of H with O_2 (and collisional stabilisation by a third body; *m*), OH with O_3 (a reversible equilibrium) and OH with H_2O_2:

$$H + O_2 + m \rightarrow HO_2 \qquad (R1.4)$$

$$OH + O_3 \rightleftharpoons HO_2 + O_2 \qquad (R1.5)$$

$$OH + H_2O_2 \rightarrow HO_2 + H_2O \qquad (R1.6)$$

and removed by reaction with O and NO:

$$HO_2 + O \rightarrow OH + O_2 \qquad (R1.7)$$

$$HO_2 + NO \rightarrow OH + NO_2 \qquad (R1.8)$$

This implies that removal of HNO_3 and HO_2 by MSPs would have secondary impacts on all of the species involved in these reactions. Example HO_2 and HNO_3 profiles are shown in Chapter 3 (Figure 3.4).

Following solar proton events, HNO_3 can also be created by conversion of N_2O_5 on protonated water clusters $H^+.(H_2O)_n$ [*Kvissel et al.*, 2012]:

$$N_2O_5 + H^+.(H_2O)_n \rightarrow H^+.(H_2O)_{n-1} + 2\ HNO_3 \qquad (R1.9)$$

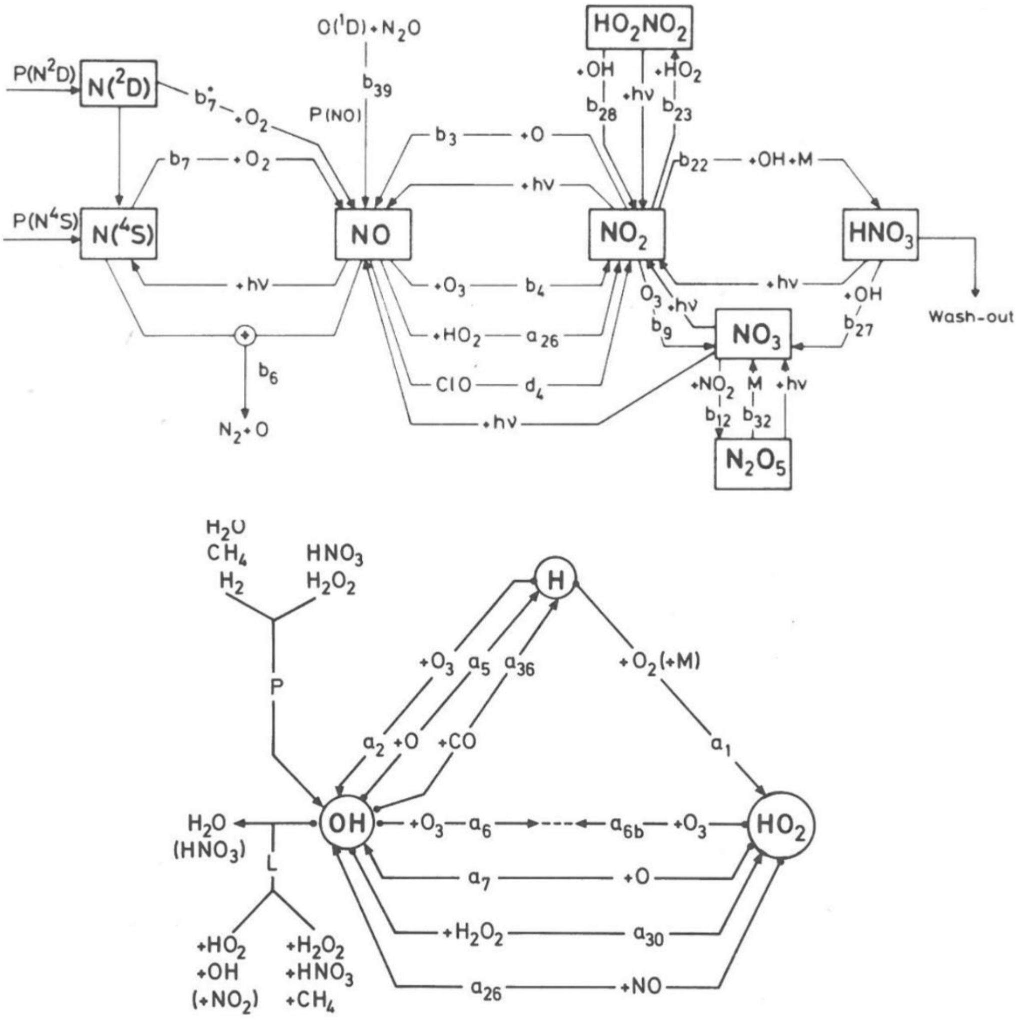

Figure 1.6: Chemistry of HO_x and NO_x in the middle atmosphere, showing production and destruction pathways for HO_2 and HNO_3. Interactions with MSPs at any stage in these can alter the balance of the atmosphere's chemical constituents, both by directly removing species *via* reactive uptake and by secondary impacts of the loss of the species taken up. Note also that there is an indirect relationship between these chemical schemes *via* the reactions of NO and NO_2 with HO_2. Reproduced from *Brasseur and Solomon* [1998], see that reference for definitions of terms and rate coefficients.

1.3 Interactions with Stratospheric Aerosol

1.3.1 MSPs in the Stratosphere

Saunders et al. [2012] showed that the interaction between MSPs and H_2SO_4 could potentially control the gas phase abundance of H_2SO_4 and cause at least partial dissolution of MSPs into liquid droplets. Recent studies using airborne particle counters with heated and unheated inlets have shown that a significant fraction (as much as 80 %) of stratospheric aerosol particles contain non-volatile (thermo-stable to over 200 °C) components [*Campbell and Deshler*, 2014; *Curtius et al.*, 2005; *Weigel et al.*, 2014]. There may be a contribution to this from precipitates left by evaporating solution droplets; however, electron microscopy shows that some MSPs and other materials are able to persist as solids [*Ebert et al.*, 2016]. Single particle mass spectrometry measurements of mid-latitude aerosol also suggest the presence of solid Si and Al containing particles [*Murphy et al.*, 2014]. Figure 1.7 shows the ratio of a variety of elemental isotopes to ^{56}Fe. The broad (in comparison to other metals) peaks shown for ^{28}Si and ^{27}Al suggest that these are produced from solid particles, since ionisation of solid particles is less uniform than liquid droplets, whereas other metals produce sharp peaks and are therefore likely present in liquid solutions.

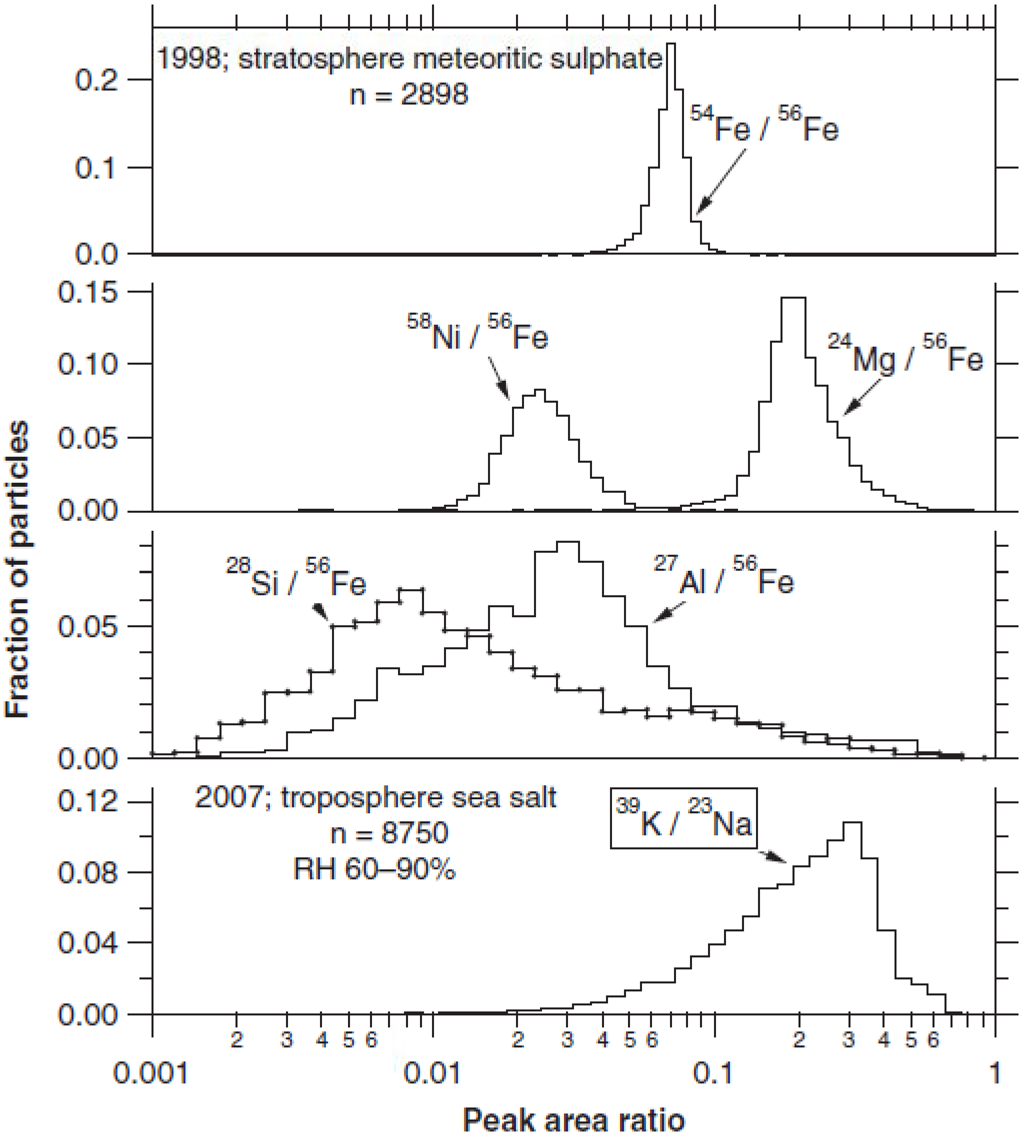

Figure 1.7: Single particle mass spectrometry of stratospheric (top three panels) and sea salt (bottom panel, for comparison) aerosol. The width of these signals is due to the accuracy of integrating mass spectral peak areas. The wider signals for ^{28}Si and ^{27}Al are indicative that these are less uniformly ionised, likely because they are present as solid particles whilst other components are dissolved in liquid droplets. Reproduced from *Murphy et al.* [2014].

The composition of non-volatile (stable under an electron beam) particles collected in the stratosphere in two size fractions (<400 and 400-3000 nm diameter) was investigated by *Ebert et al.* [2016] using electron microscopy. Polished boron substrates [*Choël et al.*, 2005], suitable for SEM and X-ray microanalysis since boron is unlikely to be present in the stratosphere, were exposed for 20 minutes to a 7.7 cm^3 s^{-1} flow of stratospheric aerosol. With the aircraft cruising at a fixed altitude at 750 km hour^{-1} [*Stefanutti et al.*, 1999], this corresponds to a cylindrical volume with circular cross section equal to the inlet size and total volume of 9240 cm^3. Particles with diameter of 1 µm will be sedimenting rapidly and have residence times in this volume on the order of tenths of a µs. This implies that the particles collected were in flux through the horizontal area of 3.7×10^{-4} cm^2 sampled in each flight. On examination under the electron microscope, several tens to hundreds of particles were found in the larger size fraction. It is difficult to explain how these particles, as sampled, could be of extraterrestrial origin; *Carrillo-Sánchez et al.* [2015] described a global flux of 1 µm radius unablated MMs of approximately 2×10^{-12} g cm^{-2} day^{-1}, equivalent to less than 9×10^{-6} particles passing through such a horizontal area in the time sampled. This, combined with the spherical nature of many of the constituent particles, would seem to exclude the possibility of the collected particles being directly formed of un-ablated IDPs, many of which do not undergo significant melting [*Taylor et al.*, 2012]. Since ablated material, after forming MSPs, is only likely to grow larger than 100 nm radius by agglomeration within liquid droplets [*Bardeen et al.*, 2008], the origin of the collected particles, most likely MSPs or artefactual observations, remains an open question.

Ebert et al. [2016] discuss contamination of the sample surface and conclude that this is not likely to be significant. In addition, the chemical composition of the particles captured is reasonable for the types of material expected in the stratosphere [*Kremser et al.*, 2016], suggesting that these particles could be agglomerates of MSPs.

Micron scale particles have previously been collected on electron microscope grids exposed on aircraft in the stratosphere but have tended to be morphologically fractal agglomerates of smaller particles [*Bigg*, 2012]. Figure 1.8 compares electron microscope images of particles collected by *Bigg* [2012] with those collected by *Ebert et al.* [2016]. The fractal particle would clearly have a longer residence time in the stratosphere than the relatively compact particle, despite both being made up of agglomerated smaller particles. One possibility is that the particles observed by *Ebert et al.*

[2016] are formed when multiple smaller particles impact the sample collector. These could be contained in a single droplet or there may be some movement of droplets and particles after the initial collection (residues were detected of volatile sulfate phases). Since the presence of volatile material in the smaller size fraction prevented a quantitative assessment, it is not possible to determine whether the mass of small particles can be reconciled with a reasonable abundance of MSPs.

Making the assumption that these particles are formed from MSPs, they may give useful insight into the types of solid material present in the stratosphere. This in turn can inform our understanding of the processing and transport of MSPs and particularly their interactions with other stratospheric aerosols.

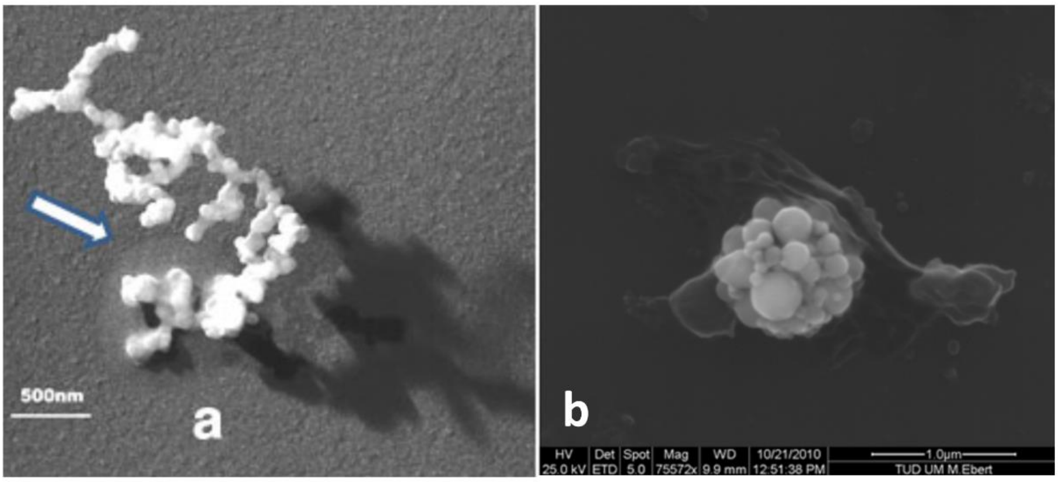

Figure 1.8: Comparison of particles collected on aircraft flights in the stratosphere by *Bigg* [2012] (a) with those collected by *Ebert et al.* [2016] (b). The arrow in panel (a) indicates a region of residual sulfate material. A fractal agglomerate such as that shown in panel (a) would reside in the stratosphere significantly longer than the relatively compact particle shown in panel (b).

The particles collected by Ebert and co-workers were found to have a wide variety of compositions including silicates, Fe rich, Ca rich, C/Si, mixed metal / oxides, Pb rich, soot and Al oxides. MSPs would likely fall into the Fe rich, Ca rich, mixed metal / oxide or silicate categories (classification was by the major peaks and many particles observed were agglomerates of different types). Metal containing silicates were ubiquitous and were classified as silicates, which dominated the total in many cases. Figure 1.9 shows the numbers of particles of each class collected in eleven flights.

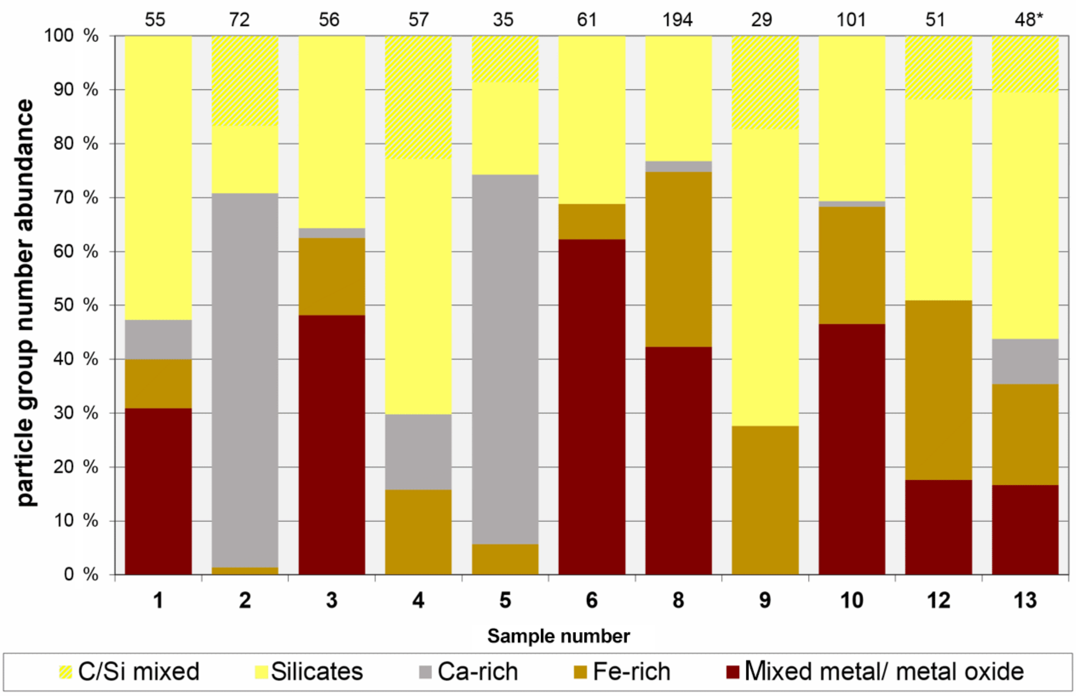

Figure 1.9: Particles (400 nm to 3 μm diameter) collected on boron impactors during 11 flights in the RECONCILE campaign (late Arctic winter). Samples were exposed for 20 minutes each through a 0.75 mm diameter pinhole with a 7.7 cm^{-3} s^{-1} flow of stratospheric air. Flights 1-5 sampled at least partially within Polar Stratospheric Clouds (PSCs). The total number of particles observed is shown above the bar for each flight. Reproduced from *Ebert et al.* [2016].

A significant reduction was observed (see Figure 1.9) in the number of Fe rich and mixed metal / metal oxide particles (a smaller fraction of the total observed non-volatile residuals) in Polar Stratospheric Clouds (PSCs) compared to elsewhere in the stratosphere. Comparing two flights (8 & 10) well removed from PSCs with the best PSC track (flight 2, all flights in PSC also include some sampling in nearby air masses): mixed metal / oxide particles fall from 44 % by number to 0 observations respectively; Fe-rich particles fall from 29 % to 1 % and silicates fall from 26 % to 13 %. The total number of observed particles also falls from 194 and 101 to just 72 in flights 8, 10 and 2, respectively [pers. comms., M. Ebert., U. Darmstadt, 2016]. This suggests that some particle types are removed by the clouds, most likely due to heterogeneous nucleation of crystalline phases on the surface of the solid particles, which are then removed when they grow and sediment out of the cloud.

1.3.2 Polar Stratospheric Clouds (PSC)

PSCs are clouds visible near the winter pole, formed when Junge layer aerosol (droplets of 70-80 wt % aqueous H_2SO_4 [*Junge et al.*, 1961]) are cooled in the winter vortex and take up HNO_3 and H_2O from the surrounding atmosphere. PSCs are known to be responsible for the depletion of O_3 in the polar spring for several reasons. Firstly, heterogeneous chemistry on the surface of PSC aerosol activates chlorine compounds which catalytically destroy O_3. Secondly growth and sedimentation of these aerosols removes HNO_3 from the stratosphere, slowing formation of $ClONO_2$, shifting the balance of Cl chemistry to more active catalysts of O_3 destruction. PSC have been observed for as long as explorers have visited the south pole and were notably described by *Scott and Jones* [2006]:

“The light was especially good today; the sun was directly reflected by a single twisted iridescent cloud in the North, a brilliant and most beautiful object”

Robert Falcon Scott, diary entry for August 1, 1911, after *Solomon* [1999]

The iridescent nature of these clouds, leading to their alternative description as ‘nacreous clouds’ is a result of the size distribution of the aerosol of which they are composed, with particle radius in the hundreds of nm, comparable to visible light.

Figure 1.10 (a) shows the equilibrium concentration of droplets as these clouds cool, calculated using the online Aerosol Inorganic Model (e-AIM, [*Clegg et al.*, 1998]) assuming atmospheric volume mixing ratios of 10 ppb HNO_3, 0.1 ppb H_2SO_4 and 4 ppm H_2O. H_2SO_4 droplets are diluted by uptake of H_2O from around 200 K, and contain significant concentrations of HNO_3 below 197 K. Below 190 K, continued uptake of H_2O again leads to dilution of the acidic droplets.

Observations have shown that at temperatures below 194 K these droplets often crystallise and grow large enough that they sediment out of the stratosphere [*Peter and Grooß*, 2012]. The crystalline phase which forms is thought to be composed of Nitric Acid Trihydrate (NAT) [*Höpfner et al.*, 2006b; *Voigt et al.*, 2000], and removal by sedimentation of this material leads to denitrication of the stratosphere, which has significant impacts on polar ozone depletion [*Solomon*, 1999]. No laboratory study to date, however, has observed nucleation of NAT at a rate large enough to describe the observed PSCs [*Knopf et al.*, 2002]. Instead Nitric Acid Dihydrate (NAD) is thought to nucleate first, but rapidly transform to NAT [*Grothe et al.*, 2008].

Where the atmosphere reaches temperatures below 188 K, H_2O ice can also form. Since H_2O ice can form a nucleus for NAT formation, this is one pathway by which NAT is formed in the atmosphere. Studies have shown that up to 80 % of NAT clouds can be explained by nucleation on H_2O ice formed in air-masses cooled by gravity wave activity [*Mann et al.*, 2005].

Figure 1.10 (b) shows the Saturation ratio (S_x, a measure of the thermodynamic stability of a phase, see Section 1.3.3) of NAT, NAD and H_2O ice, as a function of temperature. $S_x \geq 1$ implies that the phase is stable. The temperature at which each phase is stable (T_x) is marked on Figure 1.10 with vertical lines. There is clearly a significant temperature regime in a cooling air-mass where Nitric Acid Hydrate (NAX) phases are stable but H_2O ice is not. Kinetics of crystalline PSCs formed in the absence of H_2O ice have therefore been commonly parameterised by a constant number of nucleation events per volume per time, $J_{het,vol}$ / cm^{-3} s^{-1}, which is applied in any model grid box where NAT is thermodynamically stable [*Carslaw et al.*, 2002; *Larsen et al.*, 2004]. Recent studies have shown, however, that biasing all aerosol processes colder by 1.5 K improved agreement with observed cloud [*Brakebusch et al.*, 2013]. This could be indicative of an important kinetic limitation on the nucleation of NAX phases.

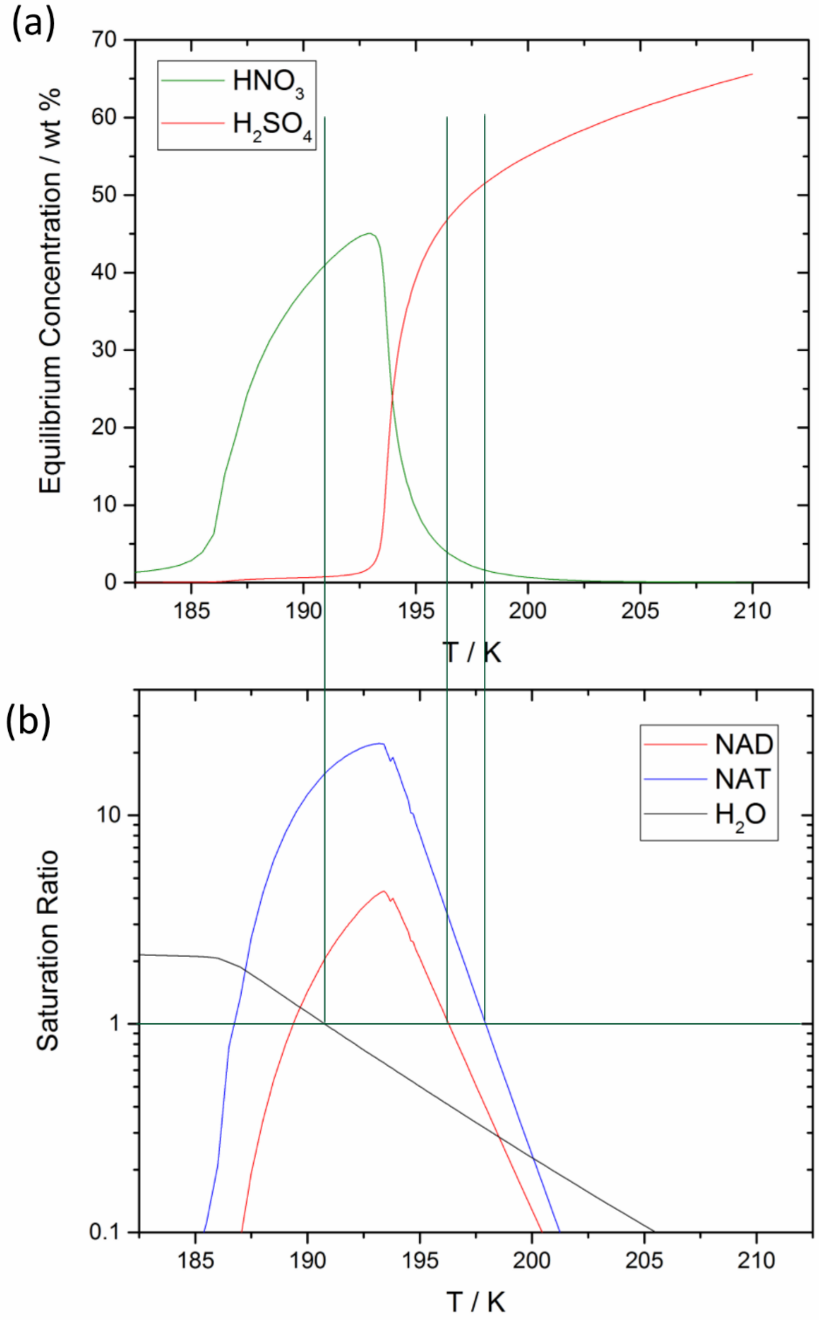

Figure 1.10: Concentration (a) and associated saturation ratio (b) of droplets in equilibrium with a gas phase containing 0.4 ppb HNO_3, 0.1 ppb H_2SO_4 and 4 ppm H_2O as a function of temperature. Horizontal and vertical green lines demonstrate the temperature and concentration at which the solution is saturated with respect to Nitric Acid Trihydrate (NAT), Nitric Acid Dihydrate (NAD) and H_2O ice. After *Carslaw et al.* [1997].

1.3.3 Nucleation Theory

To facilitate consideration of the problem of nucleation kinetics in PSC we must first examine current theoretical and technical methods for evaluating such kinetics. Note that in this thesis only nucleation by particles immersed in droplets (as opposed to particles impacting droplets or deposition of gas phase species onto particles) is considered since that is the likely mode of nucleation in PSCs [*Hoyle et al.*, 2013].

The key factors for nucleation kinetics are the temperature, T / K, and the saturation ratio for the NAX phase which nucleates, S_{NAX}. S_{NAX} is a measure of how thermodynamically stable or metastable the supercooled solution is when compared to the system with a solid phase present. It is given by the ratio of the free energy, ΔG / kJ mol^{-1}, of the supercooled liquid to the system in thermodynamic equilibrium. This ratio is equivalent to that of the activity, a_y / mol dm^{-3}, product of the components of the solid to the equilibrium constant for the dissociation of the solid, $K_{s,NAX}$:

$$S_{NAX} = \frac{\Delta G_{supercooled}}{\Delta G_{equilibrium}} = \frac{a_{NO_3^-} \times a_{H^+} \times x a_{H_2O}}{K_{s,NAX}} \qquad (1.1)$$

where $K_{s,NAX}$ is given by the product of activities of the components at equilibrium. $K_{s,NAX}$ is a function of temperature, independent of the concentration of the solution, since on nucleation of a solid the crystal will grow, consuming liquid phase components and moving the concentration to equilibrium. This is related to the concept of a phase diagram, a plot of the melting points (or equivalently of equilibrium concentrations) against temperature.

The phase diagram for the HNO_3 / H_2O system is shown in Figure 1.11. An example hypothetical path through the phase diagram is shown for a solution of constant 30 wt % HNO_3. The solution cools to 210 K, at which point H_2O ice nucleates (indicated by a star). The H_2O ice crystal grows, consuming H_2O and concentrating the solution, until equilibrium is reached. On further cooling the concentration of the solution will follow the H_2O ice melting curve, bringing it into a region where NAD becomes stable and can nucleate (shown here at around 195 K). Examining the phase diagram can provide an understanding of observations, in this example that could be the observation of a NAD phase which would not be stable in a 30 wt % aqueous HNO_3 solution in the absence of H_2O ice.

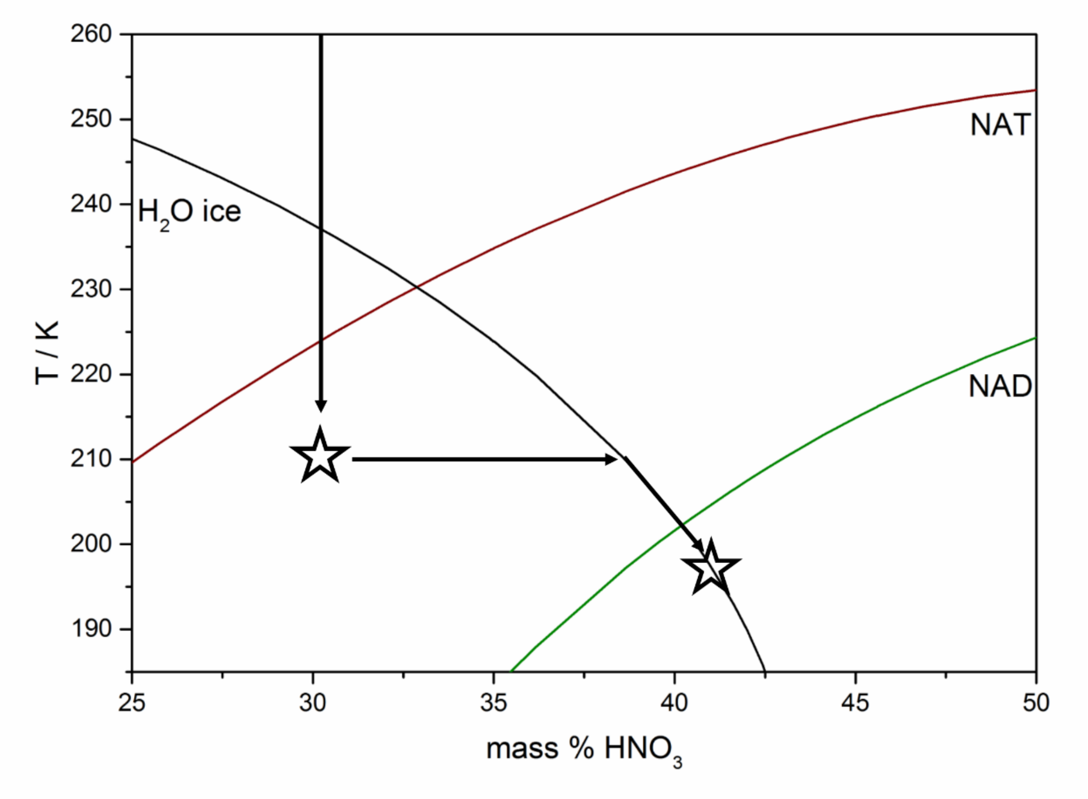

Figure 1.11 Phase diagram showing the melting points of H_2O ice, NAT and NAD in a region relevant to PSCs. A hypothetical pathway through the phase diagram is shown for a 30 wt % aqueous solution of HNO_3. The likely behaviour of the solution on nucleation (indicated by a star) of H_2O ice at 210 K is also shown.

Solid phases, even when thermodynamically stable, may not spontaneously form due to a kinetic barrier, allowing liquids to supercool. Nucleation of solid phases requires a number of molecules to come together in a physical structure similar to the crystalline phase. This is known as the critical cluster. The energy barrier for formation of this critical cluster, ΔG^* / kJ mol^{-1}, is related to the surface tension, Γ / n m^{-1}, the volume of one molecular equivalent of the solid, V_{mol} / cm^{-3}, T and S_{NAX} by [*Zobrist et al.*, 2007]:

$$\Delta G^* = \frac{16\pi}{3}\frac{V_{mol}^2\Gamma^3}{\left(k_BT\,ln(S_{NAX})\right)^2} \qquad (1.2)$$

where k_B (1.38×10^{-23} m^2 kg s^{-2} K^{-1}) is the Boltzmann constant.

The homogeneous rate constant for formation of critical clusters, J_{hom} / s^{-1}, and thereby nucleation, has been described by the Classical Nucleation Theory (CNT) and is given by [*Murray et al.*, 2012]:

$$J_{hom} = \frac{k_B}{h}e^{-\Delta F/k_BT}e^{-\Delta G^*/k_BT} \qquad (1.3)$$

where h (6.63×10^{-34} m^2 kg s^{-1}) is the Planck constant and ΔF (kJ mol^{-1}) is the activation energy for diffusion. From measurements of the diffusion coefficient of HNO_3 on H_2O ice it has been shown that ΔF can be approximated by a fixed value of 2000 k_B *[Luo et al., 2003]*.

CNT can be extended to consider the presence of a heterogeneous interface with the supercooled liquid which reduces the kinetic barrier to nucleation. Practically, this is achieved by multiplying ΔG^* by a parameter known as the effectiveness factor, f_{het}. f_{het} is a dimensionless quantity related to the contact angle, φ / °, between the heterogeneous nucleus and the supercooled liquid:

$$f_{het} = \frac{1}{4}\cos(2+\varphi)\cos(1-\varphi)^2 \qquad (1.4)$$

The heterogeneous nucleation rate, J_{het} / cm^{-2} s^{-1}, also differs from the homogeneous rate in that it is multiplied by the number of molecules, $n_{mol,int} \approx 3 \times 10^{14}$ cm^{-2} [*Zobrist et al.*, 2007], at the interface of the supercooled liquid with the heterogeneous nucleus:

$$J_{het} = \frac{n_{mol,int}k_B}{h} e^{-\Delta F/k_B T} e^{-\Delta G^* f_{het}/k_B T} \qquad (1.5)$$

The rate of nucleation events in a given gas volume, R / cm^{-3} s^{-1}, is then given by [*Murray et al.*, 2012]:

$$R = \frac{dN_{liq}}{dt} = J_{het}A_s N_{liq} \qquad (1.6)$$

where dN_{liq} is the number of liquid droplets, N_{liq}, containing surface area A_s in that volume, which nucleate in time dt. Solving this differential equation over a fixed time period, Δt, and recognising that the number of nucleation events, ΔN_{NAX}, is given by the difference between the number of droplets at the beginning, $N_{liq,i}$, and end of that time period gives the expression:

$$\Delta N_{NAX} = N_{liq,i}\left(1 - exp(-J_{het}A_s\Delta t)\right) \qquad (1.7)$$

This inherently assumes that all of the surface area in each droplet nucleates with the same efficiency. Real material, however, is likely to have many different sites on its surface, which will nucleate a crystalline phase with different efficiency.

The probability of a site activating nucleation is dependent on both temperature and time. Treating a heterogeneous surface as having a single, uniform nucleation efficiency will tend to over-represent the time dependence of nucleation (see Figure 1.12). Conversely, in some cases nucleation has been found to be time independent [*Murray et al.*, 2012], allowing the nucleation kinetics to be treated by a simple temperature dependent model whereby the fraction of droplets which have crystallised, f_{NAX}, is given by:

$$f_{NAX} = \frac{N_{NAX}}{N_{liq}} = 1 - \exp(-n_s A_s) \qquad (1.8)$$

where n_s / cm^{-2} is the cumulative density of sites which are active at temperatures greater than the current temperature.

Where time and temperature dependences are both important, it is possible to model the nucleation kinetics with a quantified time dependence [*Herbert et al.*, 2014]. Figure 1.12 compares experimental data of nucleation events observed over time and at T_{iso}; a constant temperature, to several theoretical models. Assuming that the surface facilitating nucleation is uniform predicts much more crystallisation of droplets than treating a range of activities and the stochastic nature of nucleation.

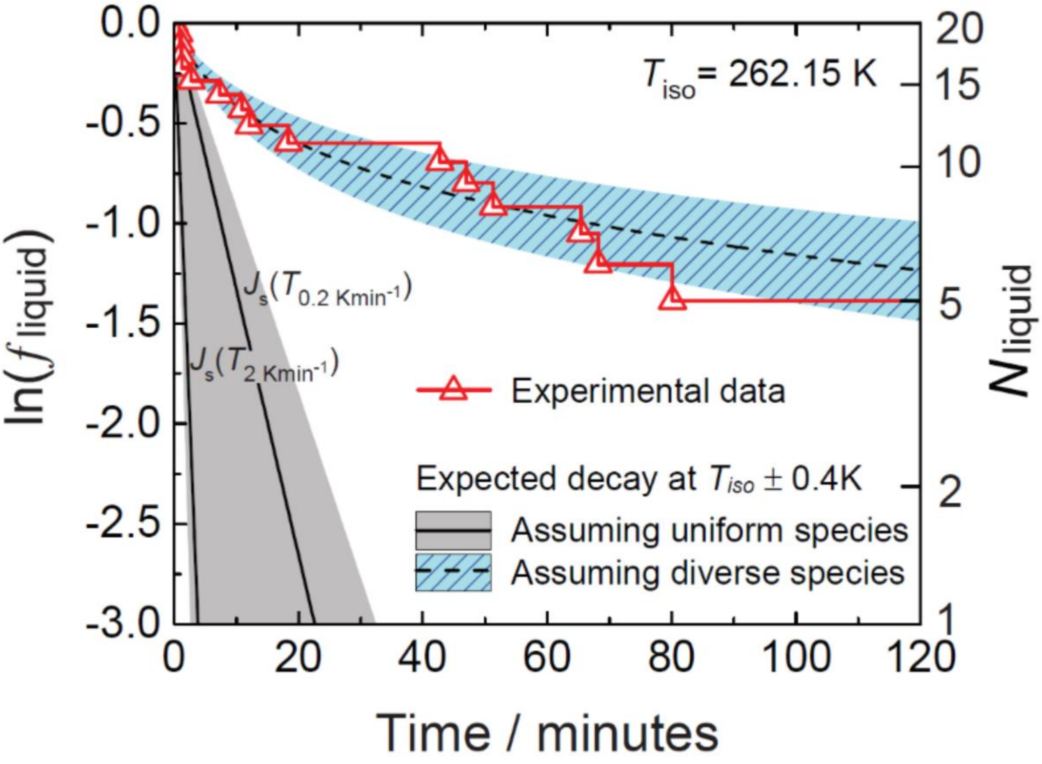

Figure 1.12 Comparison of observed H_2O ice nucleation in H_2O droplets containing heterogeneous nuclei in an isothermal experiment at 262.15 K. The solid black lines and grey shaded area represent the range of liquid fractions expected if the heterogeneous nucleus had a uniform ability to nucleate crystallisation. The dashed black line and blue shaded area represent the range of liquid droplets predicted by a model which treats a range of activity across the surface of the heterogeneous nucleus and the stochastic nature of nucleation by that surface. Reproduced from *Herbert et al.* [2014], see that publication for further details including definitions of symbols.

Recent modelling studies of the formation of PSCs have shown that heterogeneous nucleation, described by CNT with a distribution of differently active surface sites, can improve agreement with observations [*Engel et al.*, 2013; *Hoyle et al.*, 2013]. Figure 1.13 compares PSCs measured by the CALIOP satellite to those modelled over several days using either a heterogeneous parameterisation or a constant nucleation rate per volume ($cm^{-3}\ s^{-1}$). The heterogeneous parameterisation clearly better reproduces the observed cloud.

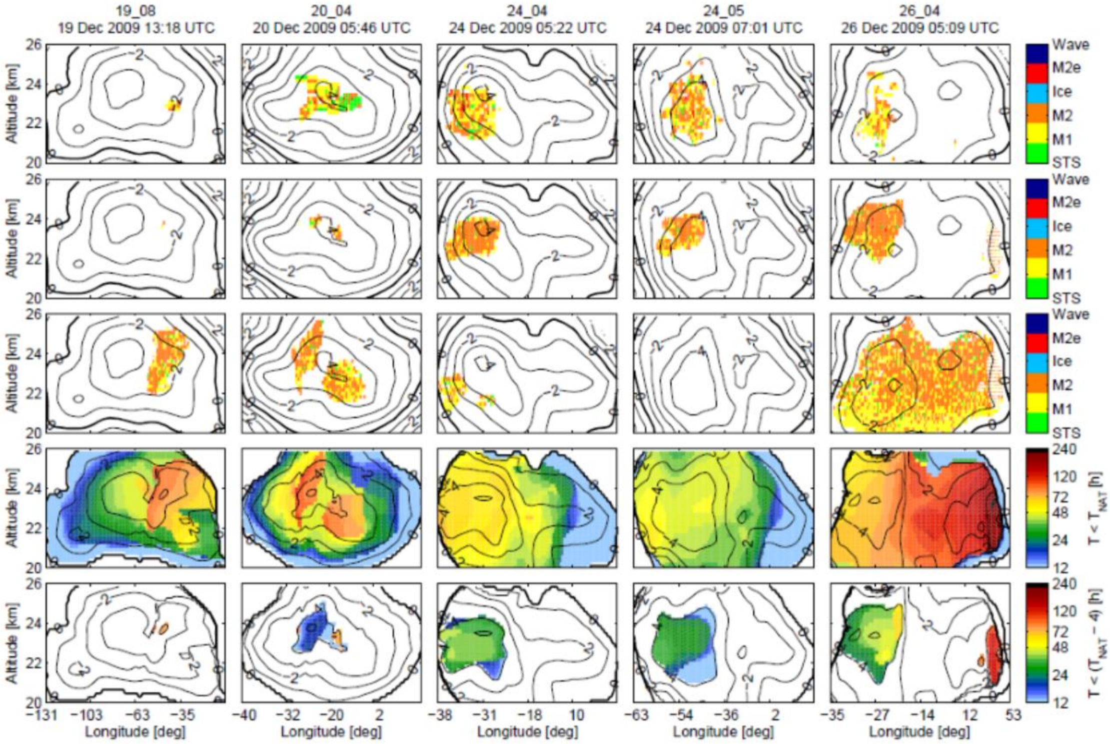

Figure 1.13:. Comparison of polar stratospheric cloud over a few days (horizontal panels) measured by the CALIOP satellite borne LIDAR (top row) and modelled using CLaMS (the Chemical Lagrangian Model of the Stratosphere) using a heterogeneous nucleation parameterisation (second row) and using a constant nucleation rate per volume (third row). The number of hours spent below the saturation point of NAT (T_{NAT}, fourth row) and 4 K lower is shown for information. Reproduced from *Hoyle et al.* [2013].

Whilst this shows compelling evidence that the heterogeneous nucleation pathway is important for the formation of PSCs, the generic nature of the heterogeneous aerosol modelled leaves an open question as to whether nucleation is dominantly triggered by MSPs or by tropospheric aerosol. The precise NAX phase which forms is also unclear. Both NAD and NAT are known to have α- and β- polymorphs, with differing stabilities [*Grothe et al.*, 2008]. Balloon-borne mass spectrometry has shown that the particles contain a molecular ratio of three H_2O molecules to one HNO_3 [*Voigt et al.*, 2000]. Satellite interferometry shows the presence of a spectral band at 820 cm^{-1} [*Höpfner et al.*, 2006b], which is likely due to the presence of NAT (both the α- and β- modifications show this feature [*Weiss et al.*, 2016]). *Höpfner et al.* [2006b] demonstrated that the equivalent feature for the α-NAD at 810 cm^{-1} was not present in the atmospheric spectrum, however the peak for β-NAD at 816 cm^{-1} is much harder to distinguish from the NAT peak. This is important since direct nucleation of NAT has not been observed in laboratory experiments at a sufficiently high rate to explain observed cloud [*Knopf et al.*, 2002]. *Grothe et al.* [2008] was able to produce NAT through thermal treatment of the thermodynamically less stable NAD phases. Such direct nucleation of a less stable (lower kinetic barrier) phase, known as Ostwald's step rule, is known to occur in the water ice system [*Malkin et al.*, 2012].

Formation of NAT PSCs likely proceeds either heterogeneously on a surface which has not yet been examined, or *via* formation of either NAD polymorph which then rapidly transforms to NAT. Transformation to NAT is unlikely to occur in the bulk solid, since significant molecular rearrangement would be required. Instead, nucleation of secondary crystalline phases in the residual solution, possibly encouraged by freeze concentration affecting the saturation or barrier to nucleation, could be followed by liquid-mediated transfer of mass from one crystal to the other. Similar processes have been suggested in the $(NH_4)_2SO_4$ / H_2O system to explain the crystalline phases observed [*Murray and Bertram*, 2008].

1.4 Aims and Contents of this Thesis

This thesis aims to address some of the issues described above.

In order to inform the general issue of how much meteoric material impacts the Earth on a daily basis, the following questions have been investigated:

1. What materials are suitable for use as analogues to meteoric material in atmospheric studies?
   This was investigated by preparation and characterisation of a range of materials and a consideration of their similarity (or not) to atmospheric materials.

2. Can uptake of reactive species to MSPs change the balance of chemistry in the mesosphere and stratosphere?

   This was investigated by measurement of the uptake coefficients for HNO_3 and HO_2 on MSP analogues and a global modelling study of how sensitive the atmospheric gas phase abundances of a range of species are to this process.

3. Can heterogeneous nucleation of crystalline phases on MSP surfaces explain the concentrations of crystals observed in the atmosphere?
   This was investigated by measurement of kinetics of nucleation by an MSP analogue and application of these kinetics in an atmospheric model.

Each of these processes has a sensitivity to the available amount of meteoric material, which could inform the total daily meteoric input to the Earth’s atmosphere.

To describe the results of these investigations, this thesis has been structured to broadly discuss processes from the top of the atmosphere moving down in altitude.

Chapter 2 describes investigations of analogues which can be used to simulate IDPs and MSPs in investigations of meteor ablation and surface science. Materials were prepared by chemical synthesis from precursors and mechanical grinding of terrestrial minerals and meteorites. The elemental composition, crystallographic, surface and size distribution properties of the products were analysed using a suite of techniques. The materials were then compared to current understanding of IDPs and MSPs in the upper mesosphere.

Chapter 3 discusses reactive uptake of HNO_3 and HO_2 from the gas phase to the surface of these particles in the lower mesosphere and upper stratosphere. Uptake coefficients measured in the laboratory were used to parameterise the impact of MSPs on HNO_3 and HO_2 in WACCM-CARMA. Comparison of model runs with and without reactive uptake was used to characterise changes in the availability of HNO_3 and HO_2.

Chapter 4 describes measurements of the nucleation kinetics of NAX phases on SiO_2 particles (analogues for MSPs) under conditions relevant to PSCs in the lower stratosphere. Droplets of HNO_3 in aqueous solutions and with suspended SiO_2 were cooled and nucleation events observed. The nucleation was then parameterised using two theoretical models and a box model of equilibrium droplet concentration used to compare the results to observations of crystal concentrations and a parameterisation commonly used in atmospheric models.

Chapter 2

Synthesis and Characterisation of Analogues for Interplanetary Dust and Meteor Smoke Particles

As described in Chapter 1, many atmospheric processes are controlled by extra-terrestrial material. Investigating and particularly quantifying the effects of these processes requires suitable samples which are chemically similar to the environmental material. This chapter describes development and characterisation of analogues for both Interplanetary Dust (IDPs) and Meteoric Smoke Particles (MSPs); aerosol which form chemically from material ablated from IDPs. These analogues include amorphous materials with elemental compositions similar to the olivine mineral solid solution series, a variety of iron oxides, undifferentiated meteorites (chondrites) and minerals which can be considered good terrestrial proxies to some phases present in meteorites. The products have been subjected to a suite of analytical techniques to demonstrate their suitability as analogues for the target materials.

2.1 Introduction and Methods

Analogues have been prepared both by processing mineral and meteorite samples, and by chemical synthesis from appropriate precursors. The genesis of the various samples is described in Table 1 along with their proposed application, specific surface area and mass density as appropriate. Note that throughout this thesis any crystalline materials will be referred to by their names, whilst chemical compositions will be used for materials without significant crystal structure.

Here MSPs, IDPs and meteorite samples are collectively referred to as meteoric material. Particles collected by aircraft in the stratosphere are often termed IDPs [*Bigg*, 2012], whilst those collected terrestrially are called MicroMeteorites (MMs) [*Taylor et al.*, 2012]. In order to determine the most appropriate analogue material, the key difference is between ablated and unablated material. In this chapter, IDPs should be taken to refer to unablated material, MSPs to ablated matter, and MMs specifically to material recovered terrestrially.

Table 2.1 Genesis, proposed analogue use, BET surface area and bulk density of samples described in this chapter.

Analogue	Genesis	Analogue for	BET surface area / $m^2 g^{-1}$	Mass density / $g cm^{-3}$
Mg_2SiO_4	$MgCl_2 + Na_4SiO_4$	MSPs	102 ± 5	
$MgFeSiO_4$	$Fe(SO_4)_2(NH_4)_2 + MgCl_2 + Na_4SiO_4$	MSPs	358 ± 16	2.647 ± 0.004
Enstatite / Hematite	From $MgFeSiO_4$ as above, sintered at 1273 K for 24 hours	MSPs	3.07 ± 0.03	
Fe_2SiO_4	$Fe(SO_4)_2(NH_4)_2 + Na_4SiO_4$	MSPs	244 ± 2	3.2638 ± 0.0007
Goethite	$Fe(SO_4)_2(NH_4)_2$ + NaOH + compressed air	MSPs	41.4 ± 0.4	3.964 ± 0.006
Hematite	From Goethite as above, dehydrated at 573 K for 24 hours	MSPs	34.4 ± 0.2	
Peridot Olivine*	Skarvebergbukren, Norway N/62	IDPs	n/a	
Albite*	Almeklovdalen, Norway N/37	IDPs	n/a	
Labradorite*	University of Leeds research collection	IDPs	n/a	
Anorthite*	Japan *via*. Gregory, Botley & co., Chelsea	IDPs	n/a	
Chergach Meteorite	Meteorites-for-sale.com	IDPs	n/a	3.5 [*Weisberg et al.*, 2009]
Allende Meteorite	Institute of Space Sciences (CSIC-IECC) research collection	IDPs	n/a	2.9 [*Clarke et al.*, 1971]
Murchison Meteorite	Institute of Space Sciences (CSIC-IECC) research collection	IDPs	n/a	2.9 [*Fuchs et al.*, 1973]
NWA 5515 Meteorite	Meteorites-for-sale.com	IDPs	n/a	2.7[*Opeil Sj et al.*, 2012]

* Terrestrial mineral samples were obtained from the University of Leeds, School of Earth and Environment research collections

2.1.1 Meteorite Samples

Samples of the Allende (CV3) [*Clarke et al.*, 1971], Murchison (CM2) [*Fuchs et al.*, 1973], North West Africa 5515 (NWA, CK4) [*Weisberg et al.*, 2009] and Chergach (H5) [*Weisberg et al.*, 2008] meteorites were ground by hand using a pestle and mortar and then sieved (Endecottes test sieves, pore sizes of 38, 106, 150, 250 and 355 µm) to obtain size fractions relevant for use as IDP analogues (tens to hundreds of µm radius [*Bardeen et al.*, 2008; *Bigg*, 2012; *Carrillo-Sánchez et al.*, 2015]). These meteorites represent several carbonaceous groups and one ordinary chondrite. Allende and Murchison have notably been used in a number of previous studies investigating IDP behaviour whilst NWA and Chergach have been included to represent outlier groups in the likely IDP flux (see Section 2.3) [*Burchell et al.*, 2006; *Court and Sephton*, 2011; *Toppani et al.*, 2001].

2.1.2 Terrestrial Minerals

Terrestrial minerals were also used here as analogues for fine and coarse-grained anhydrous IDP material. These were obtained by grinding peridot olivine, labradorite, anorthite and albite followed by size separation. These minerals were chosen as example members of solution series. Other members of such series or other minerals could also be used, either alone or in mixtures, to obtain a wider range of compositions. Similar terrestrial minerals have been used in the past to investigate IDP processing. These include simulated changes in pyrrhotites during aerobraking eg. [*Greshake et al.*, 1998] and olivine and pyroxene as a “thermometer” for the temperatures reached by meteors [*Sandford and Bradley*, 1989].

2.1.3 Synthetic Samples

Sol-gel synthetic routes to produce both crystalline mineral samples and amorphous materials of suitable composition were also used. Sol-gel synthesis uses a viscous solution to kinetically hinder reactions and facilitate formation of highly ordered inorganic materials [*Mann et al.*, 1997].

Directly synthesised compounds include amorphous materials with compositions covering the olivine solid solution series ($Mg_xFe_{2-x}SiO_4$ where $0 \leq x \leq 2$) and goethite. These can be annealed to produce secondary products including hematite and mixtures of crystalline phases such as enstatite and hematite.

$Mg_xFe_{2-x}SiO_4$ compounds were synthesised by stirring at room temperature for 7 days a mixture of stoichiometric amounts (relative to 0.1 mol l^{-1} product) of $MgCl_2$ (Aldrich), $Fe(SO_4)_2(NH_4)_2$ (Sigma-Aldrich) and Na_4SiO_4 (Alfa Aesar) [*Frankland et al.*, 2015]. Solutions immediately turn blue when Fe is present but otherwise are colourless. All solutions are viscous but do not pass the inversion test. After purification, annealing of this amorphous product at 1273 K for 24 hours was also used to generate a mixture of crystalline enstatite and hematite.

To investigate the formation of a ferrihydrate impurity in $Mg_xFe_{2-x}SiO_4$ a synthesis was also performed where HCl (Fisher Scientific, 37% analytical reagent grade) was added dropwise to bring the pH to 7 (the Na_4SiO_4 is made from a mixture of NaOH and Na_3SiO_3, giving an alkaline solution).

Here we report a novel method to produce pure goethite and, by processing this, hematite. Goethite was obtained by stirring a solution of 0.1 mol l^{-1} each of $Fe(SO_4)_2(NH_4)_2$ and NaOH (Fisher Scientific, analytical reagent grade) for 3 days with a flow of compressed air bubbling through the reacting solution. The purified goethite product of this reaction was dehydrated by annealing at 573 K for 24 hours to produce hematite.

A direct synthesis of monodisperse, regular cubes of hematite has also been performed [*Hiranuma et al.*, 2014; *Ozaki et al.*, 1984; *Sugimoto et al.*, 1993]. A solution of 2 M $FeCl_3$ (Fison’s Scientific Equipment) was added slowly with stirring to 5.4 N NaOH, the resulting viscous solution was stirred for a further 10 minutes then transferred to a Teflon reaction bomb. This was aged at 100 °C for 8 days.

All reaction products were collected and dried in petri dishes. Residual byproducts were removed using repeated dialysis (at least 15 hours total) in a Soxhlet apparatus with the particles held in water permeable tubing (Snakeskin 7000 MWCO).

Purified products, along with samples of meteoritic and terrestrial materials, were then subjected to a suite of characterisation techniques in order to assess their appropriateness as analogues for IDPs and MSPs. Mass yields after purification are >90 %, although the possibility that H_2O is adsorbed to the large surface area of the synthetic particles adds an upward bias to such measurements. In any case, approximately 20 g of $Mg_xFe_{2-x}SiO_4$ and 3-5 g goethite can be produced in a typical 2 l batch synthesis, providing sufficient material for characterisation and further studies.

2.2 Characterisation of Analogues

A thorough characterisation of each of the products described above is required to inform their use as analogues for IDPs and/or MSPs. The properties which are required for a given analogue depend on the application to which it is put. This is compounded by the differing size scales of IDPs (up to several tens to hundred µm radius) and MSPs (single molecules which polymerise and agglomerate to several hundred nm radius), which restricts somewhat the techniques available for the characterisation of each analogue.

Where ablation is examined, it is important to understand the elemental composition and crystal structure, particularly as this has implications for melting and evaporation. In studies of catalysis, however, the surface properties of a sample are of paramount importance. Such properties have been investigated for samples of the products discussed in Section 2.1.

2.2.1 Elemental composition

The elemental composition of a material has clear relevance to studies of virtually all properties of meteoric material and is arguably the most widely applicable characterisation of both environmental and analogous samples.

Taylor et al. [2012]_ENREF_59 examined around 5000 MMs from the South Polar Water Well and showed that IDPs have likely compositions similar to CI or CM meteorites. Whilst there is considerable uncertainty in the mineral composition of MSPs e.g. [*Hervig et al.*, 2012], the elemental ratios of the metals (primarily Fe, Mg) and SiO_2 available for their formation are relatively well known [*Plane et al.*, 2015].

Elemental compositions were measured by Energy Dispersive X-Ray Spectroscopy in combination with Scanning Electron Microscopy (SEM-EDX, Joel JSM 6610LV coupled to an Oxford Instruments INCA X max80 EDS). The carbon signal is omitted due to interference from carbon tape used as an SEM substrate, while the oxygen signal is affected by surface adsorbed water. This technique is limited by statistical uncertainty, since values are measured for individual particles or agglomerates rather than large, representative samples, and by reduced sensitivity to lighter elements. There is also a potential effect of particle size; since a flat surface is required for quantitative measurements, single particles are used and measurements of the smaller size fractions therefore survey less material. This could lead to an underrepresentation of rare component phases and elements. Average values with a 95% standard error (typically from 4-8 measurements) are given in this chapter. Inductively Coupled Plasma – Atomic Emission Spectroscopy

(ICP-AES, ICAP 6500 ThermoElectron) has been used for two meteoritic samples. Solutions were prepared from approximately 0.025 g of each sample fluxed with 0.05 g of Li-metaborate and dissolved in 30 ml HNO_3 1 molal and 1 drop of HF. Four standard reference materials provided by the US Geological Survey were used for external calibration; internal calibration of the equipment was carried out before the measurements and rodhium was used as internal standard. Three determinations of the elemental composition were carried out and averaged for each meteorite, showing standard errors lower than 5% for most elements.

2.2.1.1 Meteorite Samples

_ENREF_60Several size fractions (particles of <19 µm and >177.5 µm radii) of the Chergach and NWA (particles of 19-53 µm and 125-177.5 µm radii) meteorites were analysed by SEM-EDX. The composition of the Allende and Murchison meteorite samples were measured by ICP-AES. Elemental compositions of all four meteorites are compared to CI, CM composition and to their respective groups [*Hutchison*, 2004] in Figure 2.1. Note that the differences between standard compositions are generally smaller than the standard errors in the compositions. This is due to the coarse grained nature of meteorites in general. After grinding, grains of individual minerals distort the measured composition away from the mean of a larger sample.

In the Chergach sample shown in Figure 2.1 a) Si, Cr, Mn, Mg, Ca, K and P all agree within error with the standard compositions. Na and Al are enhanced (although Al is in agreement with the CM compositions) suggesting that the sample contained albite. Fe, Ni and S are depleted, suggesting that minor phases such as Fe-Ni metallic alloys and metal sulfides or sulfates are underrepresented in the sample. The Chergach meteorite has a rather Mg rich olivine content, with much of the Fe being contained in a metallic or alloy form, consistent with an enhancement of major phases over minor in these measurements [*Weisberg et al.*, 2008]. Differences in the two size fractions are generally smaller than the uncertainty. However, major constituent elements are enhanced in the smaller size fractions, whilst minor elements are depleted. This suggest that some softer phases are enhanced in the smaller size fractions, whilst phases which grind less easily are enhanced in larger size fractions. In compositional terms Chergach (and potentially other OCs) appears a reasonable approximation for IDPs, containing many of the same phases. This is significant since OCs are generally more available than CCs.

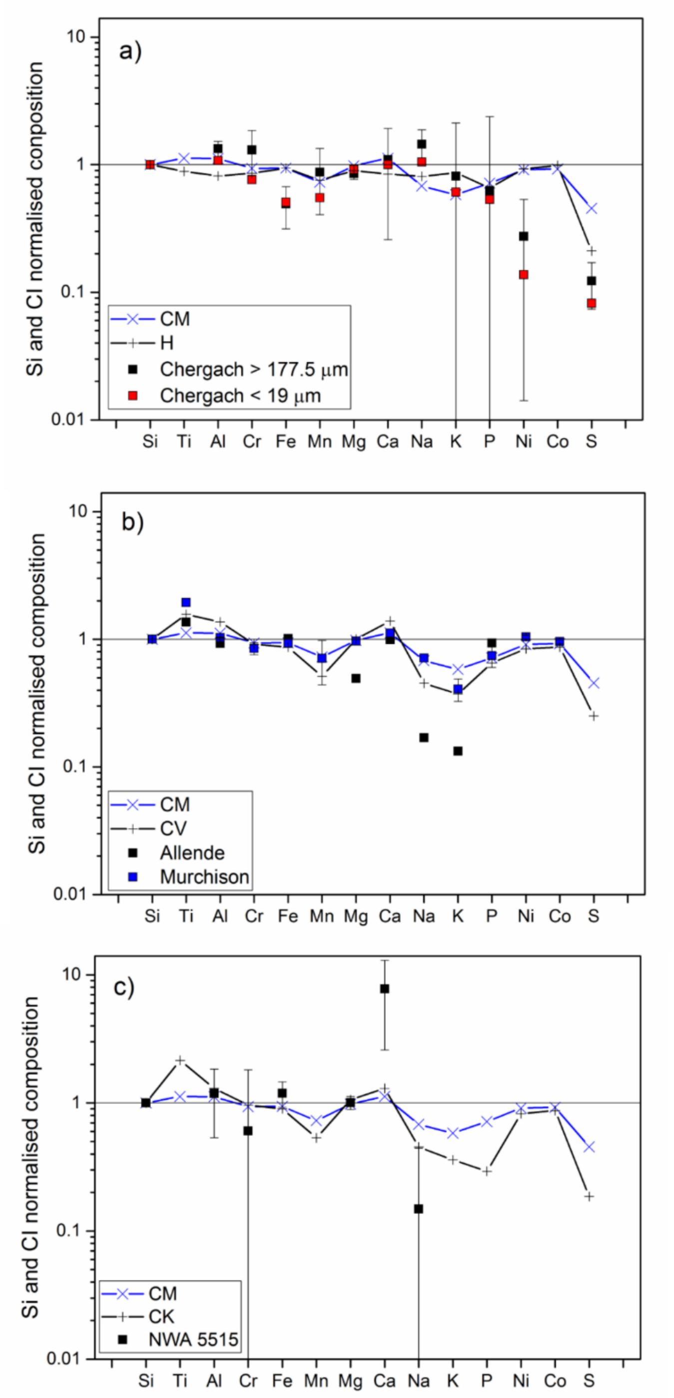

Figure 2.1: Elemental compositions, normalised to Si, comparing each of the meteorites used in this study to the composition of CI, CM and its own group [*Hutchison*, 2004]. a) Two size fractions (<19 µm and >177.5 µm) of the Chergach (H5) meteorite. b) The Allende (CV3) and Merchison (CM2) meteorites. c) The North West Africa 5515 (CK4) meteorite, 125-177.5 µm size fraction. Error bars show the 95 % confidence interval of 4-8 measurements. Measurement techniques vary, see text for details.

The Murchison and Allende meteorites, shown in Figure 2.1 b), have been included here as examples of carbonaceous chondrites which are commonly used as analogues for IDPs [*Burchell et al.*, 2006; *Court and Sephton*, 2011; *Toppani et al.*, 2001]. Allende has suffered some degree of thermal metamorphism so has compositions within the CI-CM range for all elements except Mg, Na and K. The Allende meteorite is known to have an Fe rich olivine matrix, accounting for the Mg depletion. The low abundance of relatively volatile elements such as Na and K is typical of CV meteorites but is known to be extreme in the case of Allende [*Clarke et al.*, 1971]. However, these elemental constituents and their relatively volatile phases (melting points <1500 K) are present in all samples observed. The Murchison sample agrees well with the CM (or CI) elemental composition, a fact which, combined with its relatively large available mass (>100 kg) has led to its wide use as an IDP analogue [*Burchell et al.*, 2006].

The 125-177.5 µm radius size fraction of the NWA meteorite sample, shown in Figure 2.1 c), is significantly enriched in Ca and depleted in Na. In addition minor elements including Ti, Mn, K, P, Co and S are below the limit of detection. In the 19-53 µm radius size fraction, SEM-EDX analysis shows a highly heterogeneous composition, with each particle appearing to represent a single phase (elemental ratios consistent with Andesine, Olivine and Augite were observed). This suggests a large content of refractory (melting point >2000 K) and coarse grained components, inconsistent with the bulk of the IDP flux. This highlights the fact that not all CC meteorites are inherently suitable as IDP analogues in all applications. Such materials can be useful, however for examining extreme events, *e.g*. differential ablation of particles with large entry velocities.

Ground meteorites are therefore variably suitable analogues for IDPs in terms of elemental composition, however they do contain many relevant phases (see Section 2.2.3) and since the ablation process is dominantly controlled by the melting point of the phase [*Vondrak et al.*, 2008], should act as satisfactory analogues in particular cases.

2.2.1.2 Terrestrial Minerals

Peridot olivine, labradorite, anorthite and albite samples have also been subjected to SEM-EDX analysis. The olivine was found to be Fo_{90} forsterite (ratios of Mg:Fe = 10 ± 4 and (Fe+Mg):Si = 1.9 ± 0.6) with some content of Ni, Ca and Al, consistent with the volcanic basalt casing around the peridot in which the olivine formed. The labradorite was measured as having An_{55} composition (ratios of Na:Ca = 0.8 ± 0.2 and (Na+Ca):(Si+Al) = 0.244 ± 0.014). The anorthite sample was found to have An_{97} composition (ratios of Na:Ca = 0.04 ± 0.02 and (Na+Ca):(Si+Al) = 0.27 ± 0.04). The albite sample was found to have a composition consistent with such an $An_{0\text{-}10}$ sodium feldspar (ratios of Al:Si = 0.344 ± 0.013 and Na:Si = 0.33 ± 0.04). The reproducibility (standard errors typically <20 %) of these measurements and their agreement with expected ratios for each mineral support the use of the SEM-EDX characterisation technique so long as numerous spectra are measured for each sample.

2.2.1.3 Synthetic Samples

SEM-EDX has been used extensively here to assess the composition of the synthetic products, particularly with regards to the removal of NaCl and Na_2SO_4 salt byproducts. In general it was found that around 10 hours of processing in the Soxhlet apparatus was sufficient to remove these byproducts. This validates the synthesis described above.

Compositions were confirmed for goethite (Fe:O = 0.6 ± 0.4), hematite (Fe:O = 0.7 ± 0.3), Mg_2SiO_4 (Mg:Si = 2.0 ± 0.5) and Fe_2SiO_4 (Fe:Si = 2.4 ± 0.8). When a ratio of precursors designed to produce $MgFeSiO_4$ was used, a ratio of Mg:Fe = 0.43 ± 0.12 and (Fe+Mg):Si = 1.8 ± 0.3 was measured. The overabundance of Fe can partially be explained by the presence of a ferrihydrite or goethite impurity (see Section 2.2.3); however, since the ratio of Fe+Mg to Si is not less than 2 it is possible that Mg accommodation into the synthetic $Mg_xFe_{2-x}SiO_4$ is less effective than that of Fe. This measured composition did not significantly vary on annealing to enstatite / hematite.

Note that oxygen ratios are reported for the crystalline iron oxides, but not for amorphous silicates. Indeed, the measured variability of the Fe:O ratio is larger than that other elemental ratios. This is due to contamination by surface adsorbed H_2O despite storing the samples in a vacuum dessicator for several weeks prior to composition measurements. This is thought to be a greater issue for the amorphous silicates due to their relatively large surface area with respect to the iron oxides (hundreds as opposed to several m^2 g^{-1} respectively, see Table 2.1 and Section 2.2.4). For applications where surface reactivity is important, this surface water could be removed by heating in a vacuum, though potential phase changes in the dust by such annealing should be considered where this is carried out (see Section 2.2.3). In generally, target compositions could be successfully synthesised and assayed using the techniques described here. Of the elements described here, Fe is the most abundant in Earth's atmosphere. Mg and Si have a slightly lower abundance with Na, K etc. present in smaller amounts [*Plane et al.*, 2015]. The synthetic materials presented here therefore represent suitable analogues for MSPs in terms of their elemental composition.

2.2.2 Textural Analysis and Compositional Mapping

The homogeneity of analogues is one of the key differences between ground bulk samples and IDPs. This can be evident in the elemental or mineralogical composition of the analogue material. Particle topography and homogeneity, both within each particle and across whole samples, was assessed using SEM-EDX mapping (FEG-SEM – FEI Nova 450) with EDX (AMTEK) at 18 kV) for the Chergach and Allende meteorites. Particles forming the Allende CV3 carbonaceous chondrite are heterogeneous even to the naked eye, with some white and some rounded glassy particles evident. These correspond respectively with Ca- and Al-rich inclusions and chondrules. Chergach particles, on the other hand, appear more homogeneous within each size fraction because of the recrystallization shown in this petrologic type (H5) of ordinary chondrites. These trends hold through to the microscopic scale, as demonstrated by the following analysis.

Figure 2.2 shows a micrograph and co-located compositional maps for a particle of Chergach. The Mg rich olivine matrix is clearly demonstrated, with smaller grains of a variety of phases evident. These potentially include metallic Fe (top left, bottom centre) and albite / feldspar (regions with Na and Ca).

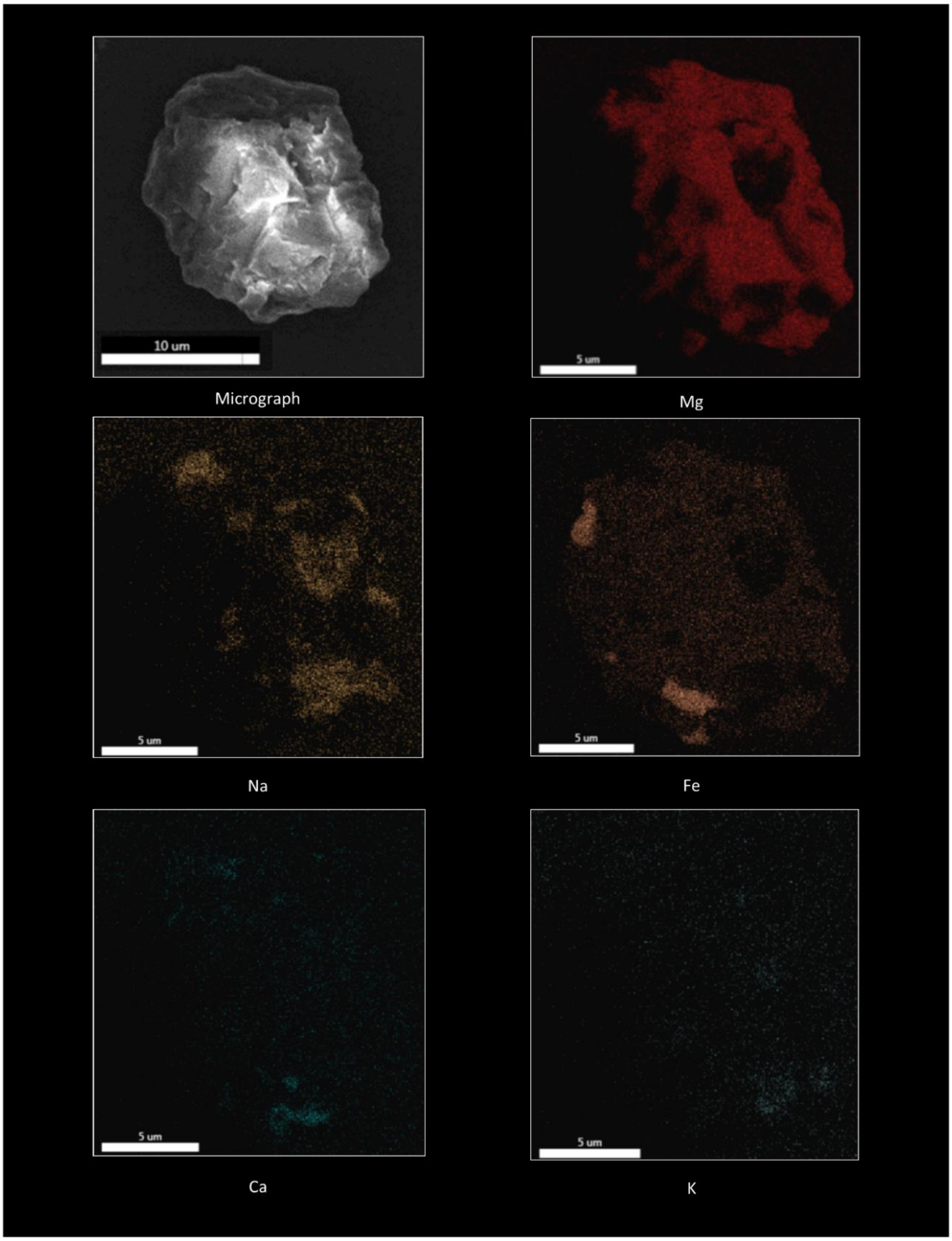

Figure 2.2: SEM-EDX mapping for a particle of the Chergach meteorite. Si is omitted due to interference from the substrate. The bulk Fo_{82} olivine is clearly shown in the Mg panel. Grains are visible containing Fe & Ca (lower centre), Na & K (lower right and centre right), and each of those elements individually.

Figure 2.3 shows a wide angle micrograph of a section of the Allende meteorite before grinding. Large features (100s of µm) are visible including a barred olivine chondrule (A), a porphyritic olivine chondrule (B), the fine grained carbonaceous matrix (C) and a metal sulfide inclusion (D). The scale of this image makes it clear that, while the mean of a large sample of particles may be a CI or CM (or in this case CV) composition as are IDPs, a ground sample of the meteorite will contain an overabundance of coarse and simple mineral grains, which would be representative of only a small fraction of IDPs.

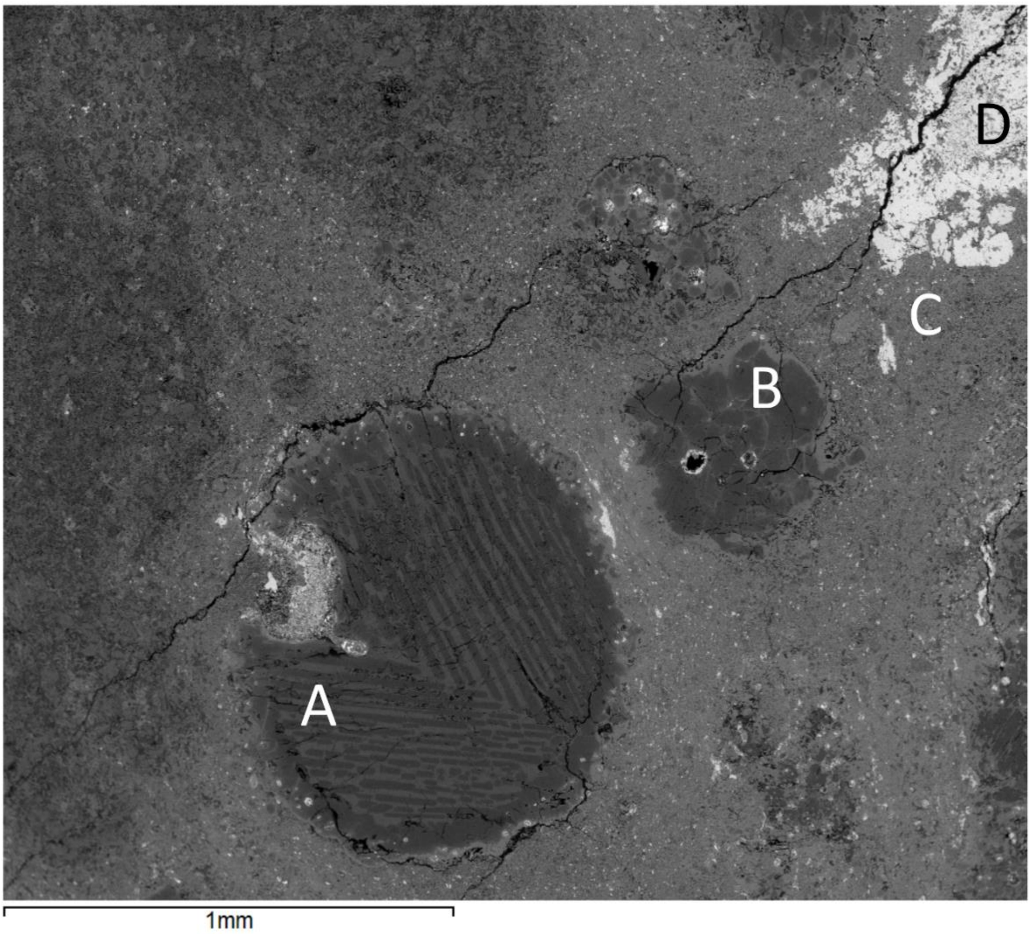

Figure 2.3: Backscatter electron image of a thin section of the Allende meteorite before grinding demonstrating the scale of individual features such as a barred olivine chondrules (A), a porphoritic olivine chondrule (B), the fine grained carbonaceous matrix (C) and a metal sulphide inclusion (D).

Figure 2.4 shows an aggregate particle of Allende, where a region of scoreacious material is in contact with a fine grained region (boundary marked by a dashed white line). EDX mapping, performed on the region shown by the white box on the micrograph, shows that the scoreacious region is depleted in volatile elements such as S, likely indicating loss of volatile phases such as troilite or more likely metal sulfate [*Burgess et al.*, 1991]. The fine grained region also shows a more heterogeneous content, with some Ca containing domains evident. This suggests that the scoreacious (right-hand) region has undergone significantly more heating, sufficient for volatile phases to evapourate and leave only the anhydrous metal silicate content. The left-hand region, however, has undergone less thermal alteration and resembles more closely a fine grained IDP.

Figure 2.5 shows two grains of Allende, one single mineral grain (left) and one fine aggregate (right). The single mineral particle appears to be a sodalite or nepheline (sodium silicate, albite is not present in significant quantities in the Allende meteorite [*Clarke et al.*, 1971]). The fine grained aggregate demonstrates the Fe rich olivine matrix of the Allende meteorite, with a heterogeneous content of Na, Al, Ca and some detectable Ni.

These examples have been selected to provide a flavour of the variability in the chondrites examined here. Such heterogeneous compositions are common in IDPs, however the fine grained nature of the majority of IDPs means that large grains such as those observed here are rare. Other authors have reported on the particle to particle variability inherent in ground meteorites [*Jessberger et al.*, 2001], however the direct comparison presented here allows some clear conclusions to be drawn. The variability displayed here for the Allende meteorite demonstrates the need to characterise samples well. In analysis of the surface or bulk properties this heterogeneity could have significant consequences. For example the rates of catalytic processes or early or late release of an ablating material could be dominantly controlled by a statistically uncommon particle or active site. One further observation is that the elemental heterogeneity in Chergach is not significantly different to that in Allende. While the texture of the grains is significantly different, grains of similar elements are present with a similar heterogeneity. This suggests that Chergach and other OC meteorites may be similar to the comparatively rare CC meteorites as IDP analogues.

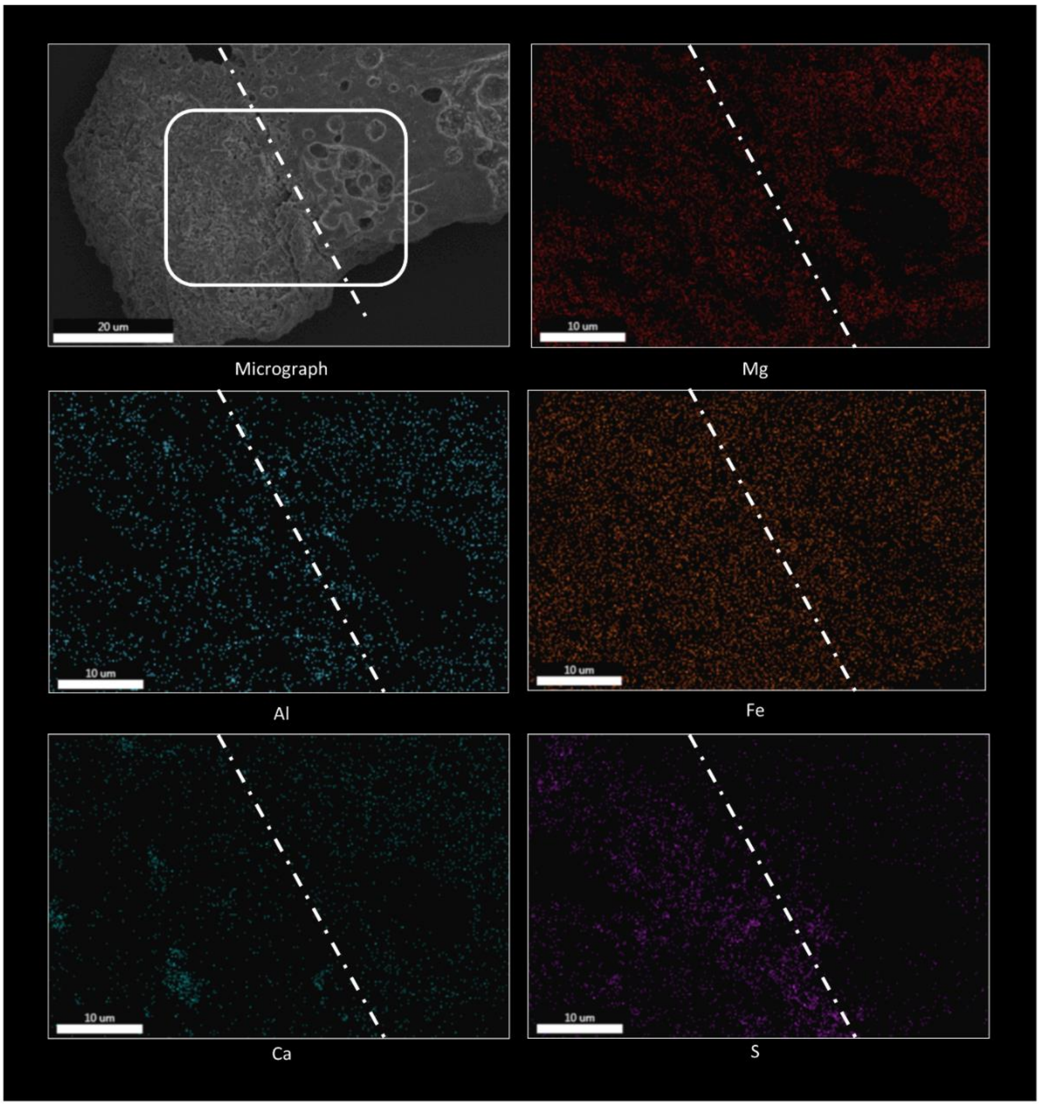

Figure 2.4: SEM-EDX mapping for a particle of the Allende meteorite, showing both fine aggregate and scoreacious regions. The fine aggregate material has a higher S content and is more heterogeneous than the scoreacious region.

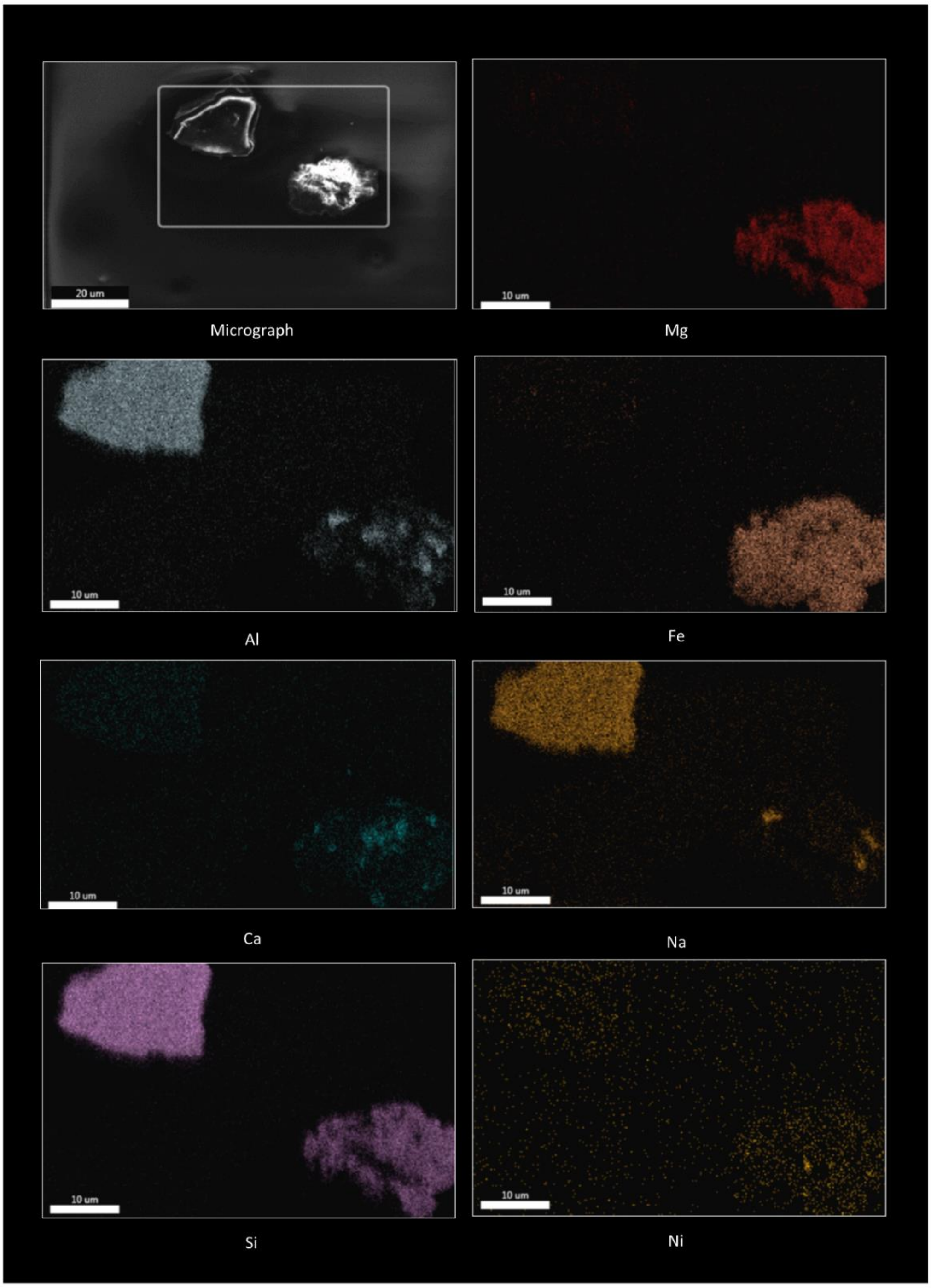

Figure 2.5: SEM-EDX mapping two particles of the Allende meteorite, showing one single mineral particle and one fine aggregate grain. Si can be included here since a Cu substrate was used. The single mineral (left) particle shows a homogeneous composition consistent with nepheline or sodelite, whilst the fine aggregate appears to have an olivine matrix containing grains of diverse composition.

SEM images of the cubic hematite synthesised in a pressure bomb are shown in Figure 2.6. Particles were deposited to the surface of the Si substrates used by evaporation of an aqueous suspension.

Figure 2.6 (a) shows that the size distribution of the particles produced is narrow. Indeed, *Ozaki et al.* [1984] described the product as “monodisperse”. The clumping of particles in some areas suggests that particles were agglomerated in suspension (see Section 2.2.5). Agglomeration of particles in suspension would affect their behaviour in *e.g*. surface science experiments because of changes in available surface area and in optical experiments because of changes to the effective size distribution.

Figure 2.6 (b) shows the size, shape and surface morphology a group of six particles. The reproducible rounded cuboid shape of the particles allows them to pack densely together, whilst the textured surface facilitates contact between particles. The surface morphology shown here would lead to an available surface area similar to that calculated assuming that the particles are spherical. Insufficient (<1 g) material was recovered in this synthesis to perform a BET analysis. The limited availability of pressure bombs, relatively long synthesis time (8 days) and low yield of this process limit its application as a method for producing MSP analogues. For applications where relatively small amounts of material are required, however, this could be a useful method for producing uniform, easily characterised material.

One caveat to the use of this material is that a small fraction of the cubic particles shatter, as shown in Figure 2.6 (c). This breaking of the cubic shape reveals a polycrystalline interior structure with a variety of types of exposed surface. *Hiranuma et al.* [2014] showed that grinding a sample of particles produced using this synthesis to expose more of this interior surface increased their activity as Ice Nucleating Particles (INP), demonstrating the importance of rare sites and heterogeneity in some surface science experiments. This is one example of why thorough characterisation of analogues can be extremely important.

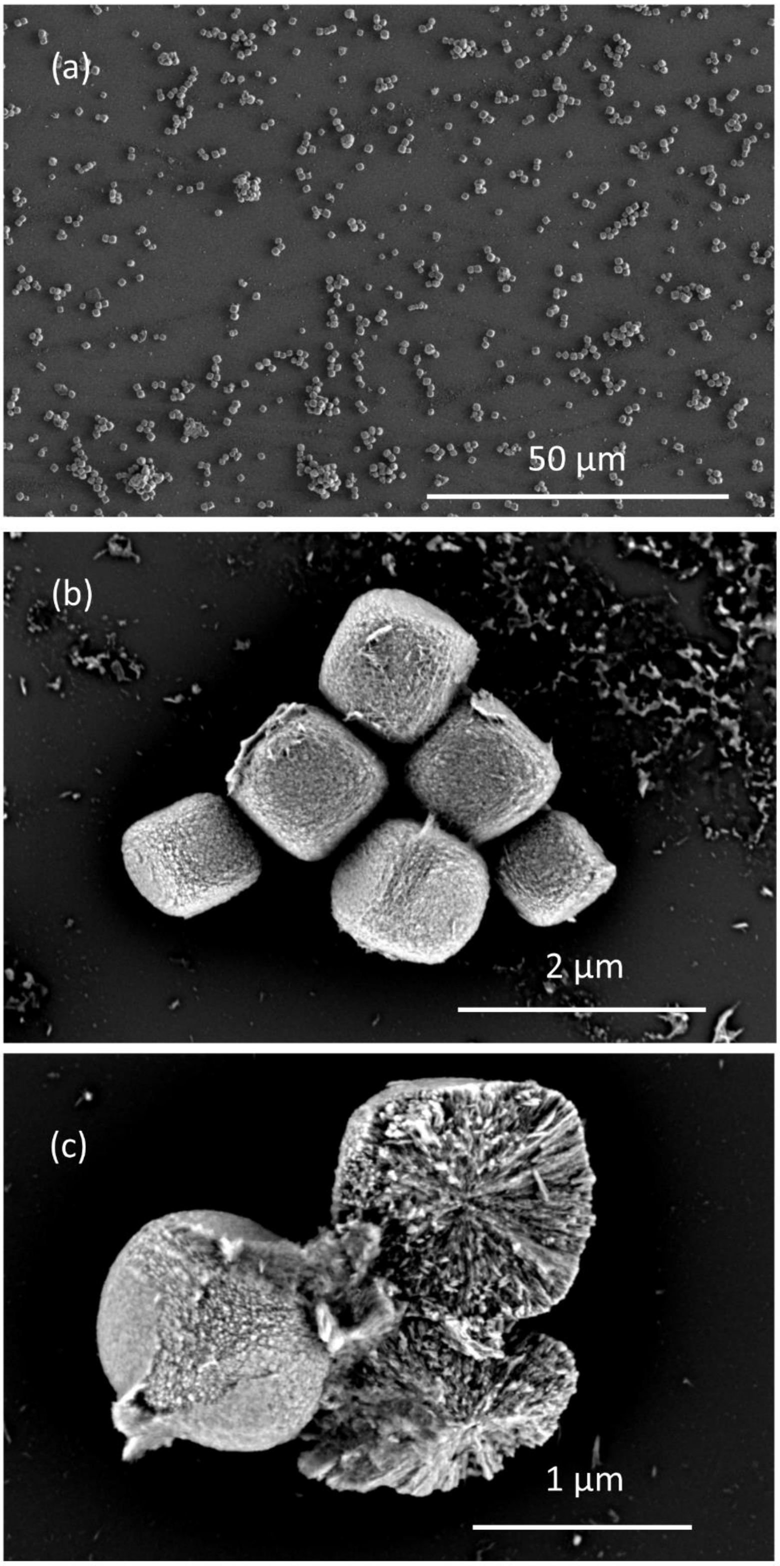

Figure 2.6: SEM images of hematite particles synthesised in a pressure bomb [*Sugimoto et al.*, 1993]. (a) a wide angle view showing a relatively monodisperse size distribution. (b) a collection of particles showing shape, size and surface morphology. (c) image of some cracked particles, showing high stress interior fractures.

2.2.3 Crystal Structure

The crystal structure of the analogue used can be important for many applications. It is crucial, for example, in studying the differential ablation of IDPs since each constituent element will be released dependent upon its vapour pressure over the phase it is contained in.

The crystal structure of the analogues was investigated by powder X-Ray Diffraction (XRD, Bruker D8 equipped with a germanium monochromator, using Cu K-α radiation). Measured patterns were compared to literature structures *via* a Rietveld refinement. This involves reproducing a pattern by comparison to one or more crystal structures. Inputs such as the crystallographic space group, lattice parameters and atomic positions allow the prediction of patterns which can be compared to the experimental observations. Factors such as nanocrystallinity and sample displacement can also be simulated to investigate peak shifts and broadening effects. Here this was carried out using the TOPAS software [*McCusker et al.*, 1999].

2.2.3.1 Meteorite Samples and Terrestrial Minerals

XRD analysis was only performed for the Chergach H5 OC due to the limited availability of other samples. Observed patterns for the albite and peridot olivine samples are compared to that of Chergach in Figure 2.7. Measured patterns (in black) can be reproduced by Rietveld refinements (in red). For peridot olivine a forsterite structure produces good agreement, for albite a structure of that mineral agrees well, and for Chergach structures of forsterite, albite and ferrosilite combine to give a good representation of the data. Whilst ferrosilite is not likely present in significant quantities, the enstatite end member of the same solid solution series has a similar structure. This suggests that in structural terms Chergach chondrite can be represented simply by a mixture of terrestrial minerals. Comparison to the SEM-EDX mapping, particularly the similarity of the heterogeneous phases present suggests that this can also be extended to other meteorites and IDPs. It is worth noting that the sample likely contains many other minor phases which are below the limits of detection here.

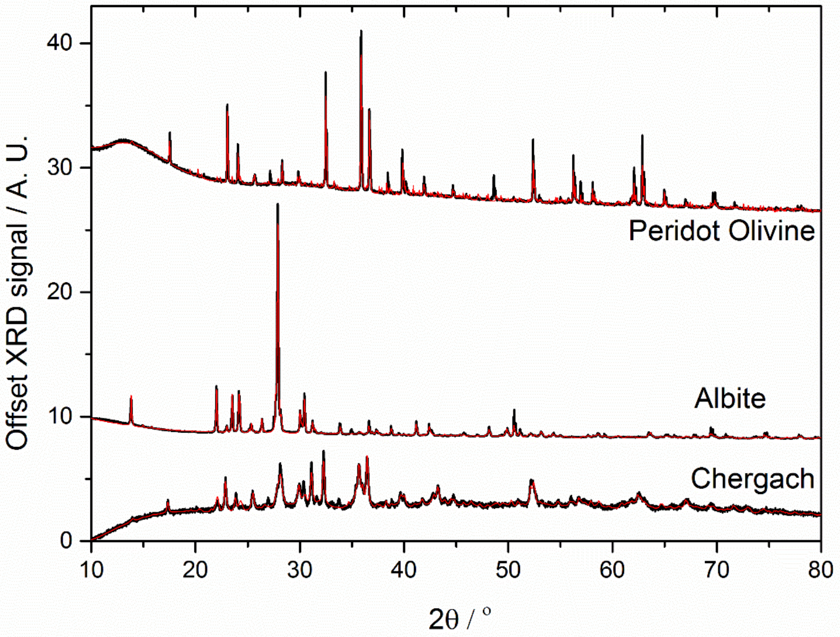

Figure 2.7: Observed powder X-Ray Diffraction (XRD) patterns for peridot olivine, albite and the Chergach meteorite. The black lines show measured data and the red lines show Rietveld refinements. Peridot olivine is compared to a forsterite structure, albite to a structure of that material and the Chergach meteorite to a combination of both with ferrosilite. Data have been scaled and offset to show an appropriate scale in each case.

In ablation experiments, individual minerals are useful to characterise phase changes as a function of heating [*Sandford and Bradley*, 1989]. Mixtures of minerals may be valuable to compare to meteoritic aggregates or even to IDPs if available, and hence evaluate the effect of grain aggregation and porosity on the release of the elemental constituents. Consideration should be given, however, to the variation of melting points across solid solution series *e.g.* [*Bowen*, 1913]. In the specific case of the Chergach meteorite (olivine composition $Fo_{81.6}$ [*Weisberg et al.*, 2008]), the melting point of major phases may be similar to the olivine used here, however for a more general study such considerations should be taken into account and terrestrial mineral analogues chosen with care. Terrestrial minerals can also be of great value in calibrating instruments, providing simple systems with known elemental ratios which are easy to characterise and available in greater supply than meteorite samples.

2.2.3.2 Synthetic Samples

XRD patterns for the synthetic samples discussed in this study are shown in Figure 2.8. Reitveld refinement (see Section 2.2.3) has a variable, though generally good, ability to reproduce the observed patterns and in some cases providing useful information regarding the synthetic product.

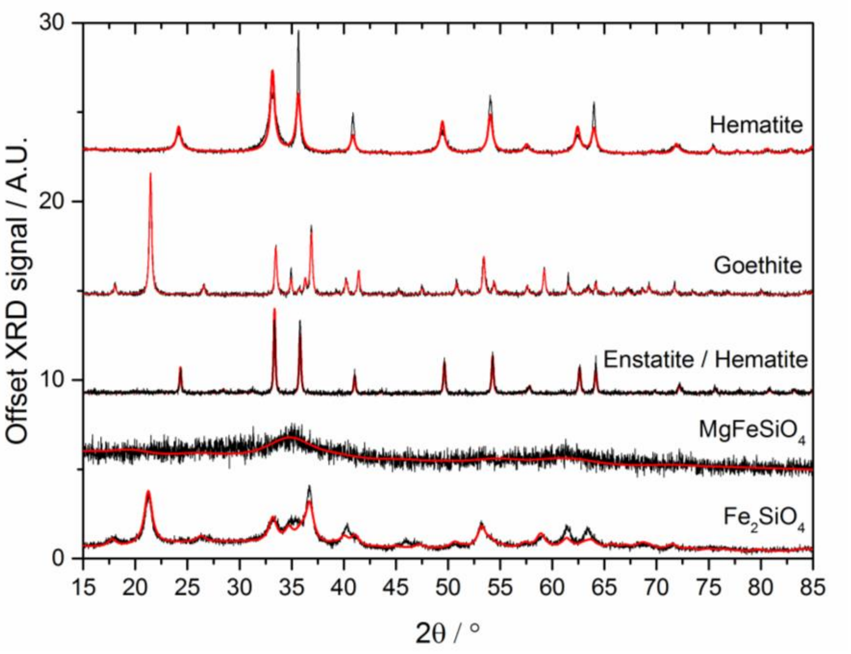

Figure 2.8: XRD patterns for synthetic samples produced in this study. Measured data are in black and fits from Rietveld refinement in red. Data have been scaled and offset to show an appropriate scale in each case.

$Mg_xFe_{2-x}SiO_4$ materials are mainly amorphous by XRD. In the case of Fe_2SiO_4 the broad crystalline peaks observed can be fitted with a goethite phase. For $MgFeSiO_4$ the similarly broad peaks are compared to a 6 line ferrihydrite phase. Ferrihydrite is a hydrated iron oxide similar to goethite. The broadness of these peaks, particularly that around 35°, is an indication of an amorphous phase or of crystals on the nm scale. For $MgFeSiO_4$ the pattern has been fitted assuming crystallites of 2.5 nm radius and for Fe_2SiO_4 the crystallites were assumed to have radii of 5.2 nm. This nanocrystallinity is discussed further in the context of the particle morphologies in Section 2.2.4. Implications of this crystallinity in terms of using these materials as analogues for MSPs are discussed in Section 2.3.

Performing the synthesis of $MgFeSiO_4$ at pH 7 did not reduce the presence of the ferrihydrite impurity shown in Figure 2.8. This suggests that the impurity may form very rapidly at the beginning of the synthesis, perhaps forming a nucleus for $MgFeSiO_4$ to subsequently deposit onto. Hydrated Fe oxides are also a likely component of MSPs [*Hervig et al.*, 2012], so the presence of this impurity phase does not significantly reduce the application as an MSP analogue. In fact, the overabundance of Fe with respect to Mg and Si in the mesosphere suggests that some Fe oxides or oxy-hydroxides are likely present alongside silicates in MSPs.

For an annealed sample of $MgFeSiO_4$ strong crystalline peaks are observed, which can be fitted with a hematite phase. Repeated SEM-EDX analysis shows that the composition does not change, suggesting that Mg and Si are present as an amorphous or nanocrystalline $MgSiO_3$ phase.

The XRD pattern of synthetic goethite is well fitted by assuming a structure of that mineral. Upon annealing a sample of this material at 573 K for 24 hours the XRD pattern could be modelled reasonably well by a hematite structure, consistent with the dehydration of the goethite [*Gualtieri and Venturelli*, 1999]. The fit in this case is imperfect, notably some peaks show significant broadening and the relative peak intensities are not well represented. Since peak broadening due to crystalline size is angle dependent this is likely an indication of relatively small crystallites (perhaps 50-100 nm in radius) but a crystallites size which gave a good fit was not found. Peak intensity variations are likely due to some preferred orientation. Implications of this crystallinity in terms of using these materials as analogues for MSPs are also discussed in Section 2.3.

2.2.4 Surface Area and Morphology

Surface properties are of paramount importance for the heterogeneous reactivity of an atmospheric solid and therefore an analogue intended to investigate such phenomena. The upper limit to the available reactive surface area was measured for the materials discussed here by the Brunauer, Emmet and Teller (BET, Micrometrics ASAP 2020) method. The results are shown in Table 2.1. The anomalously high specific surface area for the $Mg_xFe_{2-x}SiO_4$ materials is due to their unusual surface morphology.

This was investigated by Transmission Electron Microscopy (TEM, FEI Tecnai F20 200kV FEGTEM fitted with a Gatan Orius SC600 CCD camera), with a representative micrograph shown in Figure 2.9. The thin, folded sheet like nature of the material leads to a large surface potentially being available for uptake and reaction of gases.

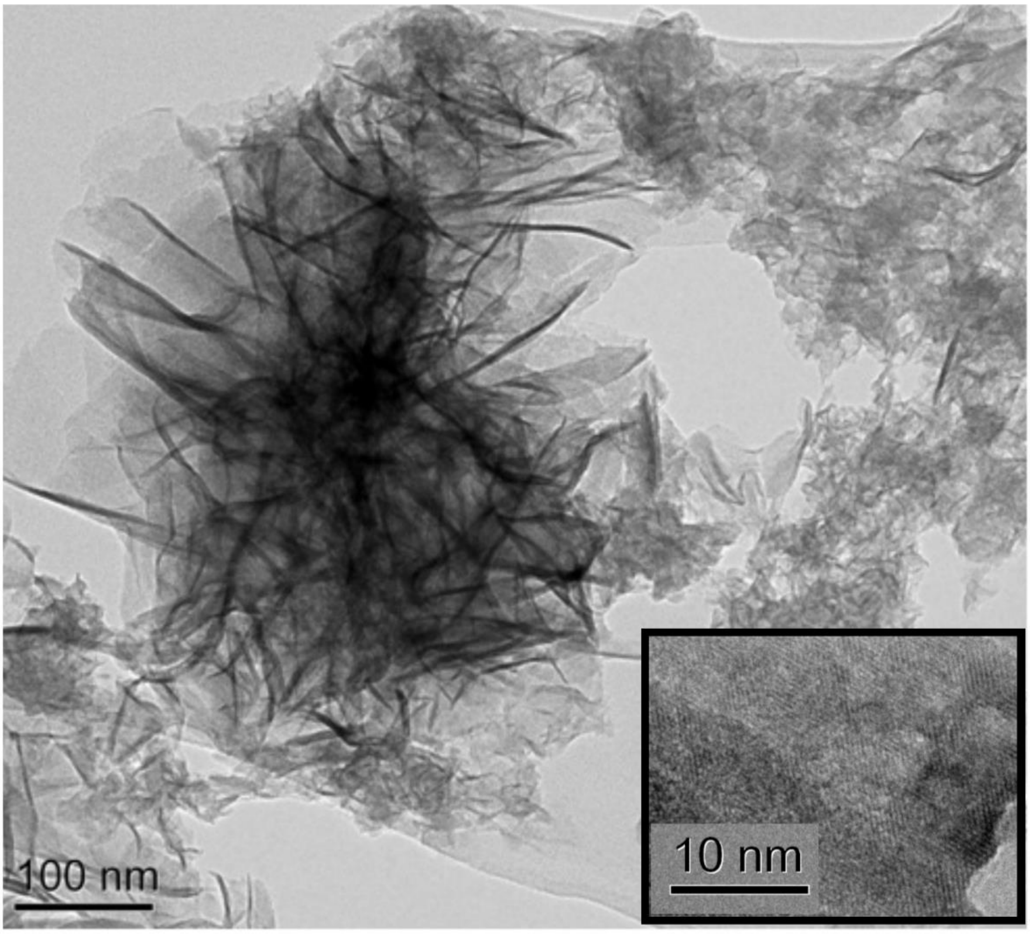

Figure 2.9: Typical transmission electron microscope image of the $MgFeSiO_4$ described in this study showing ‘folded sheet like’ morphology. Insert shows an example of nanocrystalline domains on the sheet surface.

The inset to Figure 2.9 shows that at atomic resolution nanocrystalline domains can be seen on the surface of the $MgFeSiO_4$. The scale of these domains is close to the 2.5 nm radius required to resolve the ferrihydrate peaks in the XRD analysis discussed above. This is compelling evidence that these crystalline domains produce the peaks seen in the XRD patterns and can therefore be considered an upper limit to their size. The implications of this nanocrystallinity in terms of using these materials as analogues for MSPs are discussed in Section 2.3.

The surface area which is actually involved in reaction will depend on the reactivity in a given system, however this large upper limit allows measurement of processes which are relatively slow [*Frankland et al.*, 2015]. The question of available surface area is also pertinent in the environment, since fractal or dendritic particles are often represented as spheres for reasons of computation efficiency [*Saunders et al.*, 2007]. Atmospheric processing by H_2O and acidic gases may also change the available surface area over time. Any use of such materials for surface science should include a careful study of the available surface area. In contrast, crystalline materials such as the goethite and hematite analogues presented here generally have BET surface areas close to that calculated by assuming spherical particles of reasonable size distribution (see Section 2.2.5). In that case the available surface area in a given experiment can often be well approximated by considering the experimental geometry (e.g. a coated flow tube), or assuming that layered samples of particles are close packed spheres with associated pore spaces [*Keyser et al.*, 1991].

2.2.5 Size Distribution and Density

The size distribution of an analogue can be important for many reasons. For example a layered sample of uniform sized particles might be expected to close pack with open pores, whilst a more heterogeneous distribution might have these pores between larger particles filled by smaller particles. Evaporation of particles may be kinetically controlled by the surface for smaller particles or diffusion through the molten bulk of larger particles. Density is also important in thermal studies since it impacts the conductivity of the material and in surface studies since the density of active sites is likely related to the density of a particular surface feature (*eg*. a particular ion or structural defect).

For dense, approximately spheroidal particles such as the hematite, goethite, enstatite / hematite and ground meteorites and minerals described here measuring the particle size distribution, which results from grinding, is important for designing experiments and interpreting results. For particles on the µm scale, optical microscopy can be used to probe such properties. Here we have used a backlit optical microscope equipped with an objective with a magnification of 10× to image arrays of particles. Typically around 3 dozen images containing 300-600 individual particles were produced and used to determine the size distribution of the sample using the following algorithm. First, particles were differentiated from the image background by the pixel brightness; second, to account for particles lying on top of each other in the images, the identified particles were artificially eroded until they separate and then rebuilt until they touch; particles in contact with the image edge were discarded; a minimum particle size was set to remove a background of smaller particles from each image; the area of each particle was then calculated (pixels were converted to µm^2 by reference to a standard 1 µm image). Control of the minimum size and pixel brightness threshold allow the analysis to function even for moderately transparent or reflective particles. Each particle area was converted to an equivalent circular radius, and the resulting particle size distribution was then fitted to a log-normal distribution and normalised to a probability density function for comparison.

The erosion and reconstruction process introduces several uncertainties into the analysis. First, the volume of a particle which lies on top of another is not counted, giving a downward bias in the estimated size, while imperfect separation of particles where the distance of contact is similar to the particle dimensions leads to an upward bias. Treating particle radius based on area is a major assumption of this method. For example, if the particle contacts a substrate or gas medium in profile then this may be valid, provided that the particles lay similarly *in situ* to their position on the microscope slide. However if volume properties (such as optical extinction) of the material is to be investigated then this method would likely overestimate the volume distribution, since gravitational settling on the surface of the microscope slide will tend to favour the particles laying horizontally. This would result in the shortest available vertical dimension (which is neglected here).

Example images for two of the meteorites and two of the terrestrial minerals discussed here are shown along with the measured size distributions for the Chergach meteorite in Figure 2.10. Figure 2.10 (b) shows the result of analysing Figure 2.10 (a), some overlapping particles have been separated and all which were touching the image edge have been discarded. The sizes of the remaining particles are used in determining the size distributions. These observed distributions have mean sizes within the stated pore size of the sieves used for separation.

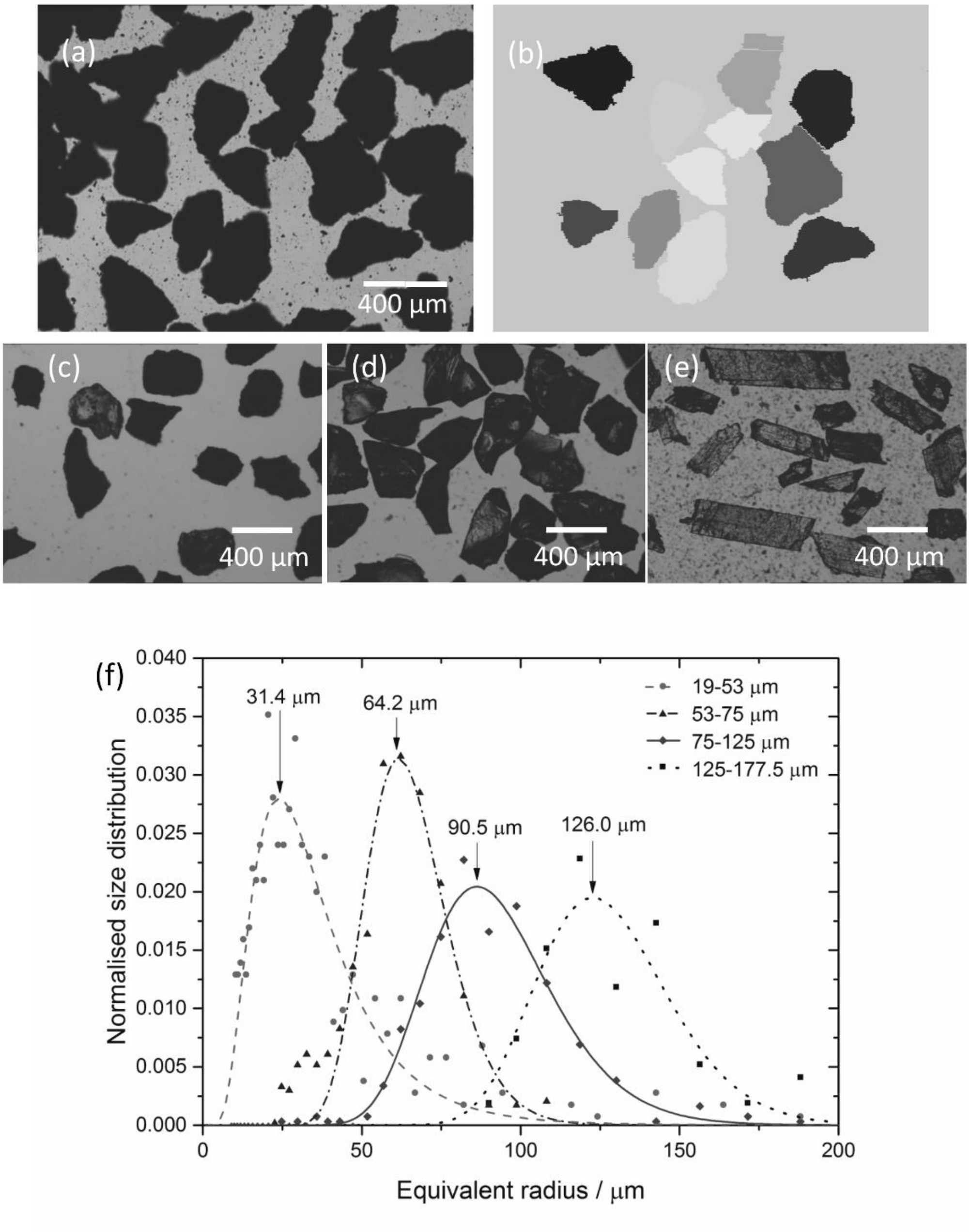

Figure 2.10: Example microscope images of the 75-125 μm radius fraction for (a) the Chergach meteorite, (c) the Allende meteorite, (d) the peridot olivine and (e) the albite samples. (b) shows the particles found by the image analysis software (described in Section 2.2.5) in (a) (scale as (a)). (f) shows a comparison of the measured probability density functions for each of the Chergach size bins investigated in this study. Mean radii are marked and limits set by sieves used for separation are given in the legend.

In general, materials which form needle-like particles (*e.g*. albite, see Figure 2.10 e) give slightly larger sizes in this analysis since they are better able to penetrate the pores in the sieves. Where each particle has been treated as an elypsoid with semi-major (longest) and semi-minor (shortest) axes of symmetry, this is shown for two size bins of the Chergach sample in Figure 2.11 by plotting the ratio of axes against the semi-major axis. There is a clear trend within both size bins for the larger particles to be less spherical.

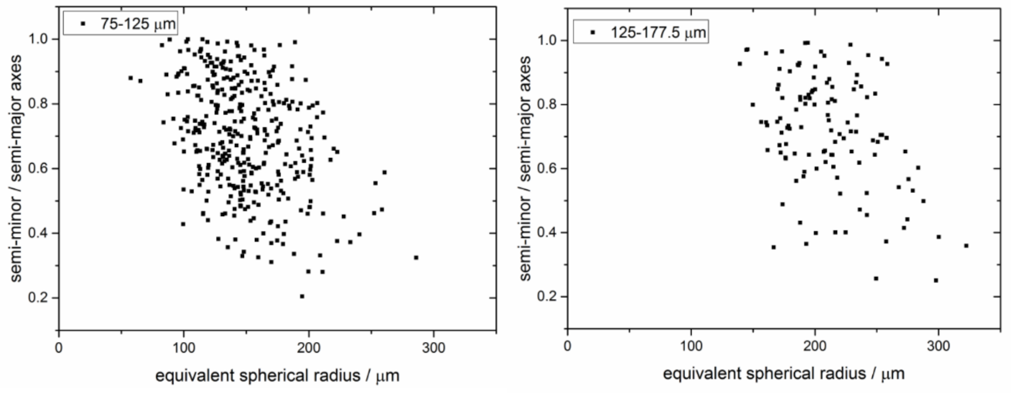

Figure 2.11: The ratio of the semi-major to semi-minor axes against the equivalent spherical radius of two size distributions of Chergach particles. The trend of larger particles having smaller ratios shows that larger particles are less spherical.

Size analysis techniques for smaller particles generally involve suspending particles in either a gaseous (*e.g*. Scanning Mobility Particle Size (SMPS) analysis [*Liu and Deshler*, 2003]) or liquid (*e.g*. Dynamic Light Scattering (DLS) [*Chu*, 2008]) medium. Aggregation can influence the results of these experiments such that in some cases only the limits of particle sizes are measurable. Measurements by both SMPS and DLS have shown that the $Mg_xFe_{2-x}SiO_4$ analogues discussed here have primary particle radii on the order of 200-500 nm. This is demonstrated by example SMPS (TSI-3080) spectra shown in Figure 2.12. Here particles were levitated into an N_2 flow using a loudspeaker, passed through an impactor (TSI 1034900, nozzle diameter 0.71 mm, D_{50} = 1286 nm) and the size distribution measured downstream. TEM imaging shows the presence of some particles on smaller scales (down to 10s of nm).

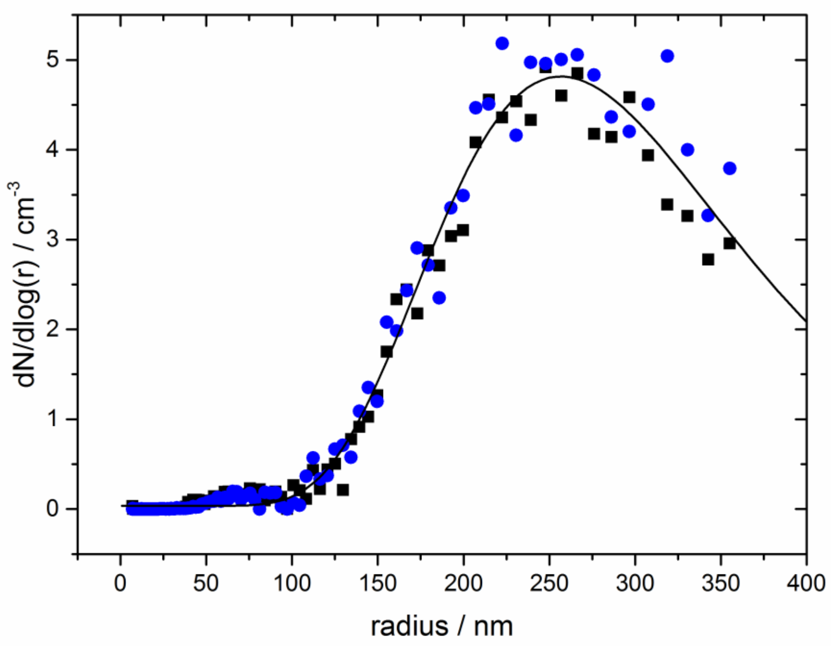

Figure 2.12: Example SMPS size distributions for the MgFeSiO$_4$ analogue entrained in a gas flow using an acoustic dust levitator. A log normal distribution with mean radius of 288 nm and width 0.341 respectively is shown for comparison (Pers. Comms. D. Moon, University of Leeds, 2015).

Proper measurement and interpretation of particle sizes is extremely specific to the application in question, however one general point to note is that while generating analogues to IDPs on the appropriate scale is relatively easy, the relatively small size of MSPs (molecular dimensions up to 100 nm radii [*Bardeen et al.*, 2008]) means that manufacturing analogues for these particles in sufficient quantity for many experiments is extremely challenging. Instead (as here) analogues likely to behave similarly are generated and the measured properties (*e.g.* rates or extinctions) extrapolated to atmospherically relevant particle sizes.

Another volume dependent quantity which can be important for experimental applications is the mass density of the analogue. Mass densities for some of the analogues discussed here are given in Table 1. The synthetic samples have densities significantly lower than for their equivalent bulk minerals, including those materials which are crystalline. This suggests a significant porosity, in agreement with the morphology described above for the Mg$_x$Fe$_{2-x}$SiO$_4$ materials. *Jessberger et al.* [2001] also noted a significant porosity in collected micrometeorites and IDPs.

2.3 Discussion

2.3.1 General

The meteorite samples discussed here represent a range of types (CC and OC, differing metamorphic groups). Whilst CC materials such as CI and CM appear to dominate the IDP flux, design of experiments using meteorites as IDP analogues is generally restricted to those types for which large masses of sample are readily available. The elemental composition, heterogeneity and crystal structure data presented indicate, however, that in many cases OC meteorites or even single minerals represent suitable analogues to IDPs (even beyond the 10 % of IDPs which are OC material). Murchison is a good example of an aqueously altered chondrite (group 2) and contains significant hydrated minerals such as philosylicates, as found in fine grained IDPs [*Taylor et al.*, 2012]. These phases will dehydrate and recrystallise when heated and so will most likely ablate similarly to the feldspathic minerals present in OCs. In addition, analysis of the NWA meteorite shows that there are large deviations within CC meteorites, and that many of these may be useful only for examining extreme or rare cases of IDPs. For example, studies are underway at the University of Leeds into differential ablation using a new Meteor Ablation Simulator (MASI) instrument [*Gómez Martín et al.*, 2016 - Unpublished results]. *Kearsley et al.* [2009] produced cometary analogues for impact studies in aerogel and Al foil by aggregating mineral fragments using an acrylic adhesive. These analogues provide excellent insights into the collection of IDPs and cometary dust in aerogel. However, from the point of view of chemical ablation studies, which take place on a relatively long time scale compared to impact and where the adhesive may cause undesired interferences, further characterisation experiments are required. The adhesive coating would also be likely to interfere with surface science experiments, where the mineral surface should be exposed to be observed directly.

Saunders and Plane [2011] have described a method of producing MSP analogues by photolysis of chemical precursors which then recondense in the gas phase. Amorphous $Mg_xFe_{2-x}SiO_4$ materials and Fe oxides are produced with a primary particle radius of 5-10 nm. These small primary particles agglomerate to produce fractal-like particles, likely a good representation of environmental MSPs. These particles have been probed for their optical properties and ice nucleating ability [*Saunders et al.*, 2010; *Saunders and Plane*, 2006]. We note that the amorphous nature found for those particles is similar to that described here. Where the primary particle radius is 5-10 nm, this sets the upper limit of the crystallite size similar to $Mg_xFe_{2-x}SiO_4$ sheets with maximum thicknesses / domain radii of several nm (Figure 2.9).

One significant difference is that the photochemical methods are able to produce Fe oxides which are amorphous, whereas we only observe crystalline products. This may simply be due to the size of the crystallites formed. Whereas in the photochemistry experiments many particles nucleate, take up the available precursor and at some point grow faster by agglomeration than deposition to existing particles, our solution phase synthesis allows relatively fewer particles to grow to larger sizes at which their crystallinity is measurable. Since MSP remain at small sizes, the photochemical method is likely more representative, so that care should be taken when using the materials synthesised by sol-gel processes as analogues for MSP.

Biermann et al. [1996] used micrometeorites as analogues for MSP nucleating crystallisation in polar stratospheric clouds and found that nucleation rates were not high enough to explain observed cloud. As the authors in that study observed, micrometeorites are generally compact, dense particles coated with magnetite crystals, which form due to serpentenisation of olivine after the IDPs reach the surface. MSPs which are present in stratospheric droplets, on the other hand, will have been processed and largely dissolved by the acidic content of those droplets [*Saunders et al.*, 2012]. *Murphy et al.* [2014] used single particle mass spectrometer measurements to show that silicon and aluminium in such droplets are generally solid while most other metals are in solution. A silica or alumina substrate would therefore seem more appropriate for investigating nucleation in polar stratospheric clouds.

Nachbar et al. [2016]_ENREF_15 used photolysis of chemical precursors to produce very small (several nm radii) particles, which were held in an ion trap at supersaturated conditions and used to measure nucleation kinetics and particle growth of CO_2 phases. These particles are alike both in size and composition to MSPs and therefore are highly appropriate as MSP analogues. As with the photochemical technique of *Saunders and Plane* [2011], the difficulty in using this material to investigate a wider range of applications lies in producing bulk amounts (*e.g*. typically several grams are required for uptake experiments).

2.3.2 Recommended Analogues for Specific Applications

With this discussion in mind, conclusions can now be drawn about which materials are most suitable for use as analogues to meteoric material in certain circumstances. The following are specific examples and each case should be taken individually.

Studies of the ablation of IDPs

CI or CM chondrites, where available, remain the best known analogue for unablated IDPs. Where sample availability is an issue these can be substituted with OCs. The major caveat to this is that chondrules will be overrepresented as a volume or mass fraction of the total material. Such studies should therefore be supplemented by studies of individual materials so that signals due to different components of the MM sample can be understood.

Surface reactivity of unablated MM

Since surface reactivity of a mixed material can be disproportionately controlled by individual components of the mixture the true surface area of the active material in that case would be difficult to estimate. CI/CMs are therefore not suitable for use as analogues for the surface reactivity of IDPs since it is known that this would over represent some surfaces. Instead, reactivity of a range of individual minerals should be measured and atmospheric surface areas of each estimated.

Surface reactivity of MSPs

Further to the above discussion of reactivity of unablated MM, the fractal agglomerate nature of MSPs should be considered whenever their reactivity is investigated. These amorphous or nano-crystalline materials may have significantly different reactivity to bulk crystalline minerals. Amorphous materials of reasonable composition are therefore the most appropriate candidates. Careful consideration of the composition of the atmosphere should also be made in these studies. It is thought (see Chapter 1) that MSPs in Earth’s atmosphere are composed of metal silicates or oxides, however in reducing atmospheres (e.g. Titan) the composition may be quite different. The photochemical method described by *Saunders and Plane* [2006] notably produces such amorphous materials with a fractal morphology similar to that expected of MSPs, however this technique is limited in its ability to produce large sample masses for surface science studies. Sol-gel techniques should therefore be used where more sample is required.

Crystal nucleation in polar stratospheric cloud by MSPs

This has been included here as a special case of MSP reactivity since meteoric material is often speculated to be the nucleating material in polar stratospheric clouds. As MSPs are transported into the stratosphere they will take up sulfuric acid and partially dissolve in the resulting acidic liquid (see Chapters 1 and 4). [*Bogdan et al.*, 2003] suggested that the high temperature preparation of fumed silica may result in a material which is morphologically similar to MSPs. Indeed electron micrographs from that study compare most favourably to those taken by *Saunders and Plane* [2006] of photochemically produced MSP analogues, as shown in Figure 2.13. Fumed silica therefore ought to be a good analogue for MSPs which cause nucleation in the stratosphere.

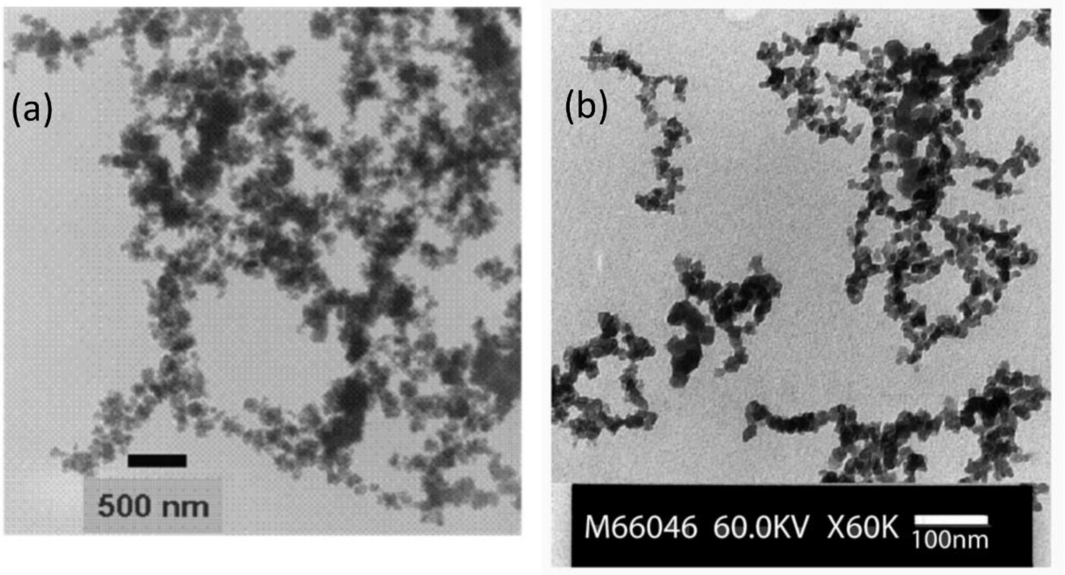

Figure 2.13: (a) TEM image of photochemically produced Fe_2SiO_4 MSP analogues with a fractal morphology likely representative of the atmospheric material (reproduced from *Saunders and Plane* [2006]). (b) TEM image of fumed silica showing a remarkably similar morphology (reproduced from *Bogdan et al.* [2003]).

2.4 Conclusions

This chapter has demonstrated the preparation of a variety of analogues for IDPs and MSPs. The methods involved can be employed by other researchers since they are simple and use materials which are widely available to the scientific community. No general comments are made here as to the best analogue to use for a given application. Instead some common issues are raised in order to help researchers choose materials for a wide range of applications.

It has been shown that reasonable analogues for IDPs can be produced by grinding and size segregating meteoritic material. The elemental composition of such analogues will vary slightly from the target material but phases which are present in IDPs will be well represented in ground meteorites. OCs are scarce in micrometeorite collections but samples of OC meteorites are much easier to source than CCs. Although ground OCs produce denser, more compact analogues, elemental compositions and mineralogy are reasonably close to those of average IDPs. Terrestrial materials such as peridot olivine, labradorite, anorthite and albite, when similarly ground, are good analogues for individual phases within IDPs, particularly for applications such as instrument calibration where paucity of sample can be an issue. In the cases of both meteorites and terrestrial minerals it was shown that mechanical sieving can reliably produce target particle size fractions which are representative of IDPs.

Chemical syntheses were presented for compounds with elemental compositions similar to the olivine solid solution series. These are thought to be nanocrystalline folded sheets. The large surface area presented by this morphology allows measurement of relatively unreactive processes which occur at the interface, whilst the elemental composition is similar to that expected for MSPs.

A chemical synthesis was also presented for crystalline goethite, which could be dehydrated to produce hematite. These are potential components of MSPs. The crystalline nature of these materials may not be representative of MSPs; nevertheless for some applications they may still be considered suitable analogues.

Finally, it is clearly of great importance that in laboratory experiments where analogues are used for IDP or MSP materials, careful attention is paid to characterising the analogue and ensuring that the limitations of its applicability are understood.

Chapter 3
Reactive Uptake of HNO_3 and HO_2 in the Middle Atmosphere

Heterogeneous uptake of reactive species to the surface of Meteoric Smoke Particles (MSPs) can perturb the atmospheric composition in the upper stratosphere and mesosphere, as discussed in Chapter 1. This chapter describes global modelling studies of the uptake of two species, HNO_3 and HO_2. Parameterisations of uptake based on laboratory experiments have been included alongside MSPs in the Whole Atmosphere Community Climate Model (WACCM) coupled to the Community Aerosol and Radiation Model for Atmospheres (CARMA). Comparison of model runs with and without uptake shows significant impacts of MSPs on atmospheric concentrations of HNO_3, and HO_2.

Whilst the effect on HO_2 is confined to the polar vortex in the upper stratosphere, HNO_3 is removed throughout the winter hemisphere. The effect of uptake to MSPs on HNO_3 is overestimated at altitudes below 35 km since interactions with H_2SO_4, which will deactivate the surfaces of the particles, have not been included in these model simulations. For HNO_3, the uptake coefficient was varied to investigate the potential impact of temperature dependent uptake on the results.

3.1 Methods

In order to assess the impacts of MSPs on the atmospheric concentrations of reactive species (unablated IDPs will be tens to hundreds of µm in radius and thus sediment too quickly to perturb concentrations) models which treat both MSPs and heterogeneous uptake are required.

A clarifying note on terminology; here altitudes are presented in terms of pressures. These can be approximately converted to altitudes *via* the scale height [*Yung and DeMore*, 1999], however as pressure is the more physically relevant unit it is used throughout this chapter. Reference to altitudes "above" a certain pressure should be taken to mean "at higher altitude" rather than "at higher pressure (*i.e*. lower altitude)".

Agglomeration and transport of MSPs and heterogeneous uptake to their surfaces was modelled (see acknowledgements for details of collaborations) in the 3-dimentional (global) model WACCM-CARMA [*Bardeen et al.*, 2008]. WACCM is a numerical model extending from the surface to 140 km. Here we have used version 4 (with NCAR Community Earth System Model 1.0.3 as common numerical framework), which has 88 hybrid σ-pressure vertical coordinate levels (each having pressure of $1000 - n \times 5.96 \times 10^{-6}$ hPa) with latitudinal, longitudinal and time resolution of 1.9 ° and 2.5 ° and 30 minutes, respectively [*Feng et al.*, 2013]. The model has a very detailed description of atmospheric processes, including nonlocal thermodynamic equilibrium, radiative transfer, auroral processes, ion drag, and molecular diffusion of major and minor species and an interactive chemistry module, thereby resolving most known neutral chemistry and major ion chemistry in the middle and upper atmosphere. Each field is calculated at 30 minute time steps.

To facilitate comparison between model runs, allowing investigation of single additional processes, WACCM-CARMA was run with Dynamics Specified (SD-WACCM) from the Goddard Earth Observing Systems model (GEOS-5). GEOS-5 data for the years 2005 to 2010 was combined with ("nudged") 1 % of the WACCM meteorological fields (temperature, winds, surface pressure, specific humidity, surface wind stress, latent and sensible heat flux etc…) at every model dynamics time step. This nudging factor then reduces linearly from 1 to 0 % between 50 and 60 km, above which the model is free-running.

3.1.1 Modelling Atmospheric Meteoric Smoke Particles

Particles of molecular radius (r = 0.2 nm) were injected into WACCM-CARMA from 75-100 km, with the peak injection at 83 km - the altitude where MSPs are known to form [*Hervig et al.*, 2009; *Plane et al.*, 2014; *Rapp et al.*, 2012; *Robertson et al.*, 2014]- and allowed to agglomerate collisionally. The total injection rate is scaled to give a global flux of ablated particles of 44 t d^{-1} (see Section 1.1). This is clearly a simplification of the full nucleation / condensation / agglomeration growth processes which lead to MSPs in the atmosphere, however similar modelling which treated 0.2 nm particles forming from reaction of precursors and also allowed condensational growth of smaller particles lead to similar size distributions; with the largest particles reaching 100 nm diameters (pers. comms. J. M. C. Plane, Leeds University, 2013).

As discussed in Chapter 1, MSPs are assumed to be compact spheres with associated surface area. At the sizes reached sedimentation is negligible, so MSPs are transported by the atmospheric circulation. Since they form relatively evenly across the mesosphere, this means that they are carried to and concentrated in the polar vortex, which transports them from the mesosphere to stratosphere. This much of the process has been modelled using WACCM [*Bardeen et al.*, 2008].

Further transport processes have been examined using other global models. The results show that a minor population of MSPs then spread out and are transported to low latitudes, where tropospheric folding allows them to cross the tropopause [*Dhomse et al.*, 2013]. Most are incorporated into Polar Stratospheric Cloud (PSC) aerosol, which grow large enough to sediment and cross the polar tropopause (modelled deposition rates are at least 10 times higher at midlatitudes compared to equatorial regions). Once in the troposphere MSPs will reach the ground by a variety of wet and dry deposition mechanisms. Modelling of transport and deposition of radioactive ^{238}Pu oxide nano-particles formed on ablation of a satellite power unit has shown that this transport from ablation to deposition takes around 4 years [*Dhomse et al.*, 2013].

3.1.2 Modelling Heterogeneous Uptake in the Atmosphere

Robust modelling of atmospheric species clearly requires a treatment of all effective sources and sinks of that species. This chapter aims to demonstrate whether uptake to MSPs can impact the atmospheric concentrations of HNO_3 and HO_2.

Uptake of a gas-phase species, x, to a solid surface is a first order process where the rate constant is given by the product of the rate of collisions, k^* / s^{-1}, with the surface and the probability that a collision results in loss from the gas phase; the uptake coefficient, γ. This gives the rate equation:

$$\frac{d[x]}{dt} = -\gamma k^*[x] \qquad (3.1)$$

where t is time. k^* is related to the molecular mean speed, $\bar{c}$ / cm s^{-1}, and available surface area, a_S / cm^2, by:

$$k^* = \frac{1}{4}\frac{a_s}{V}\bar{c}$$

where V / cm^3 is the gas volume under consideration. $\bar{c}$ is given by:

$$\bar{c} = \sqrt{\frac{8k_BT}{\pi m_x}}$$

where k_B is the Boltzmann constant, T the ambient temperature and m_x / kg is the molecular mass of the species of interest. This inherently neglects diffusion of the gas phase species into the bulk of larger particles, however the speculative mechanisms of uptake in the cases of both HO_2 and HNO_3 suggest that diffusion will be minor.

This kinetic expression was applied in SD-WACCM, along with the available surface area of MSPs and the atmospheric concentration of either HNO_3 or HO_2. This involves an inherent assumption that uptake to the surface is irreversible. In reality there may be a reduction in the available surface area of MSPs; otherwise evaporation, possibly following a reaction, may make these sites available again (see Section 3.2.6).

Values of γ based on laboratory measurements (see Section 3.1.3 and acknowledgements) have been used as the basis for SD-WACCM simulations of atmospheric uptake. A variety of model runs investigating the uptake of HNO_3 and HO_2 onto MSPs were carried out and are summarised in Table 3.1. A control run was performed to evaluate WACCM as a tool by comparison to observations. This also establishes a baseline for atmospheric concentrations of species of interest. Individual processes were then introduced to the model and any differences assessed to evaluate the sensitivity of the atmosphere to those processes in relation to others which are already included. γ_{HNO3} of 0.002, 0.02 and 1 were applied to represent; the value measured at room temperature, a factor of 10 increase to account for the effects of low temperature and the maximum possible uptake, respectively. This is intended as a study of the sensitivity of uptake to γ, which could inform future studies aiming to properly quantify the impacts of heterogeneous uptake. A further run was performed with γ_{HO2} of 0.2, chosen as the measured room temperature value with a factor ~3 increase to account for temperature dependence.

Table 3.1 WACCM-CARMA (version 4, CESM 1.0.3) runs carried out. All use the MSP scheme of *Bardeen et al.* [2008] with a total ablated mass flux of 44 t d^{-1}. This is injected as 0.2 nm radius particles between 75 and 100 km, with the peak injection rate at 83 km to simulate the formation of MSP from the mesospheric metal layers.

Run	Species taken up	Uptake Coefficient
Control	None	-
HNO_3 measured	HNO_3	0.002
HNO_3 T	HNO_3	0.02
HNO_3 max	HNO_3	1
HO_2	HO_2	0.2

During transport, MSPs interact with a number of species other than the HNO_3 and HO_2 discussed here. Notable interactions which have not been treated here include H_2O and H_2SO_4. Previous modelling has shown that below ~40 km (2 hPa) MSPs start to take up H_2SO_4 [*Neely et al.*, 2011; *Saunders et al.*, 2012]. This will block access to active sites on the surface of the MSPs and eventually leads to their incorporation into stratospheric sulfate aerosol. Modelling this process is beyond the aims of this study, since it would require tracking of several arrays of particles, interacting with each other and gas-phase species, which would be computationally expensive for the multiple runs required here (see Table 3.1). Impacts observed at low altitudes will therefore be overestimated since this reduction of activity has not been included. Possible interactions of H_2O with the uptake process are discussed in Section 3.1.3.

3.1.3 Measurement of Uptake Coefficients

Laboratory measurements of uptake coefficients can be carried out in many ways. In most cases, a flow of gas containing the target species is allowed to interact with the target aerosol and the loss of species compared to an experiment in the absence of aerosol is used to evaluate the uptake coefficient *via* the solution to equation (3.1):

$$\gamma = \frac{4V}{a_s \bar{c}} \ln\left(\frac{[x]_0}{[x]_t}\right) \tag{3.2}$$

In some methods work is carried out in the Knudsen regime, where the gas-phase pressure is low enough such that gas-surface interactions dominate over gas-gas [*Hanisch and Crowley*, 2001]. In others corrections are applied for diffusion of the target species through a gaseous medium to the heterogeneous surface [*Matthews et al.*, 2014].

Here γ values measured on the $Mg_{2x}Fe_{2-2x}SiO_4$ analogues described in Chapter 2 in two experimental studies have been adapted for atmospheric applications. See the acknowledgements in the front matter of this thesis for full details of collaborations in these studies.

γ_{HNO3} values were measured in a Knudsen cell, where a sample of particles was held behind a movable flap and HNO_3 / He gas mixtures were passed through the cell and measured with a mass spectrometer (QMS, Hiden HPR-60 EPIC). Particles were isolated or allowed to interact with the gas flow and any observed drop in signal was used to calculate γ_{HNO3} values. See *Frankland et al.* [2015] for further details. Experiments were carried out with and without H_2O coating the particle surface. An example is given in Figure 3.1, where uptake of both H_2O and HNO_3 is evident. The H_2O signal gradually returned to the background level over the one hour exposure, suggesting that the surface became saturated with H_2O. The HNO_3 signal, however, did not recover indicating that the surface was not saturated on this timescale.

γ_{HO2} values were measured by entraining particles in a flow of N_2 (using agitation from a loud speaker) and passing them down a flow tube with a flow of HO_2 / N_2. Particle size distributions were measured by a Scanning Mobility Particle Sizer (SMPS, TSI, 3080, see Figure 2.12), total number concentration was measured by a Condensation Particle Counter (CPC, TSI 3775) and the HO_2 signal is measured by the Florescence Assay by Gas Expansion (FAGE) technique. Upstream of the flow tube, particles were conditioned in a drift tube at variable relative humidity. HO_2 / N_2 gas mixtures were introduced into the flow tube using a sliding injector so that the contact time with the particles could be varied. See *James et al.* [2016] for further details. Figure 3.2 shows an example of the effect of different number concentrations of MSPs on the HO_2 signal. There is a clear loss of signal when particles are introduced (a), which gives a straight line when plotted as a natural logarithm (b). By equation (3.2), the gradient of this line is then $(\gamma_{HO2}\, \bar{c}\, a_s\, t)$ / 4. Figure 3.3 then shows a plot of $(\gamma_{HO2}\, \bar{c}\, a_s\, t)$ / 4 against contact time, from which a linear fit allows γ_{HO2} to be calculated. The uptake coefficients measured in each study are summarised in Table 3.2.

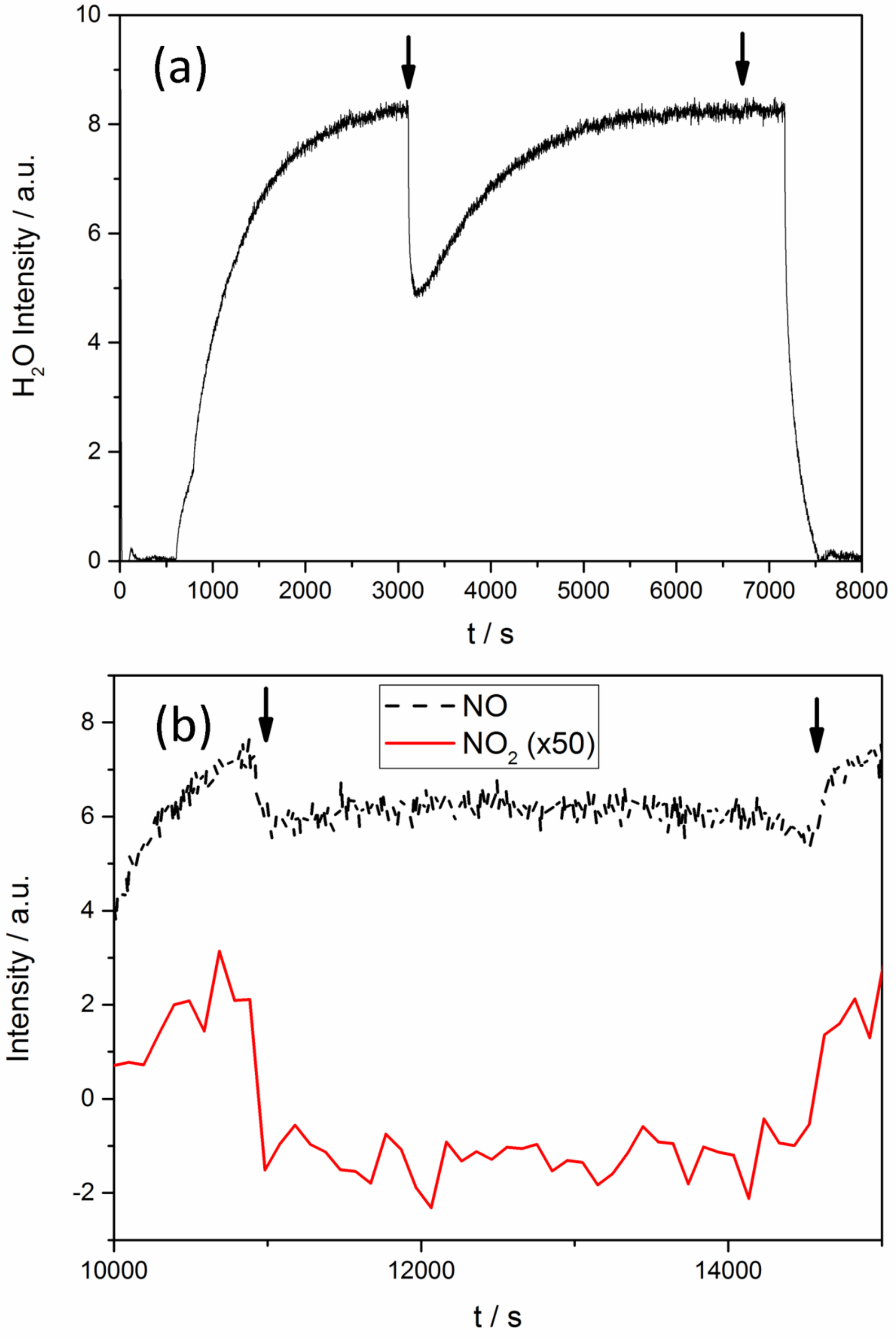

Figure 3.1 Mass Spectrometer signals for (a) H_2O and (b) daughter species of HNO_3. The black arrows indicate times at which the gas flows were allowed to contact the surface of MSP analogues by opening and closing a movable flap. Exposure to the particles creates a clear signal drop, indicating that gas-phase species have been taken up on the solid surfaces. See *Frankland et al.* [2015] for further details.

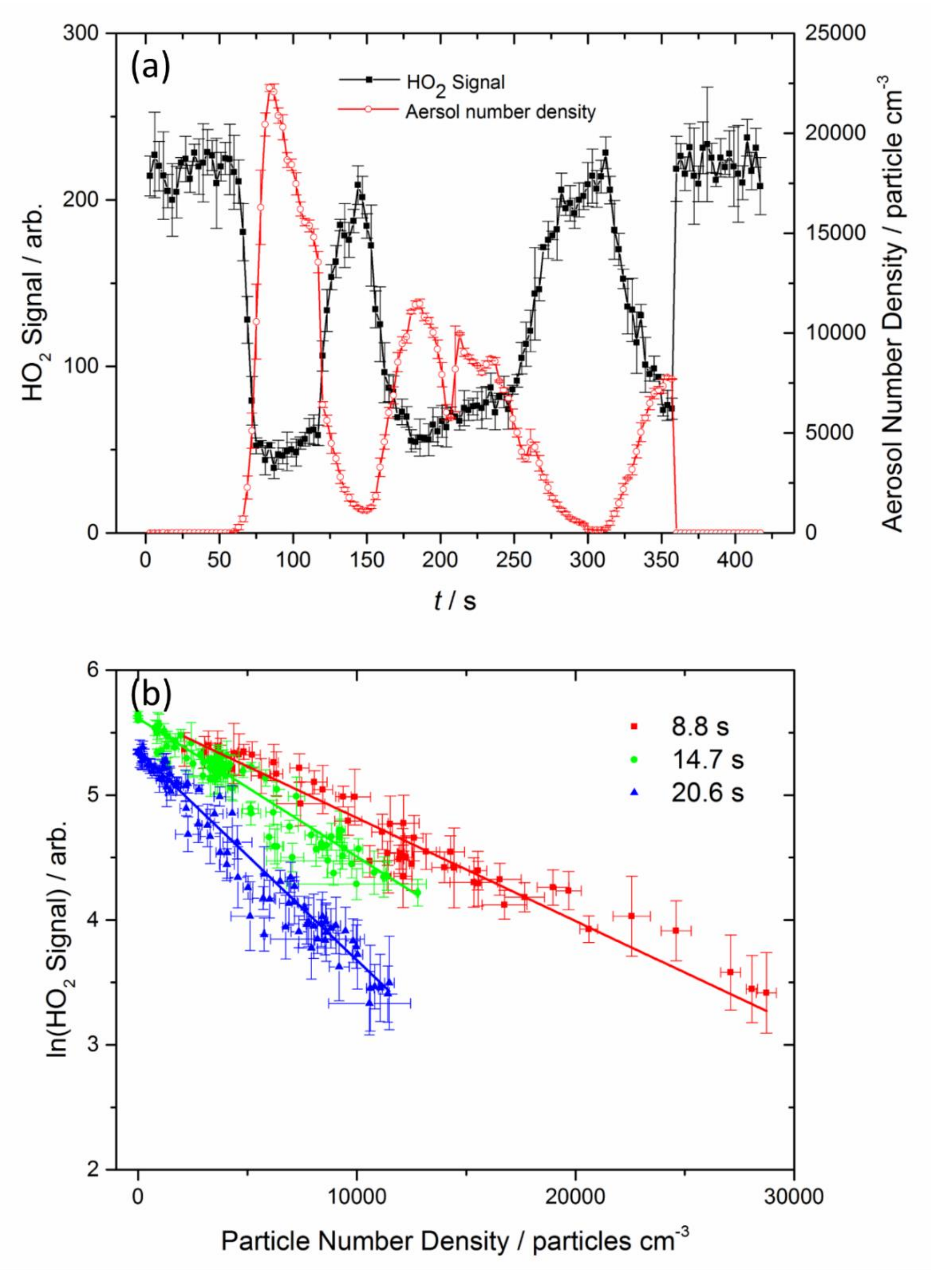

Figure 3.2 (a) The anti-correlation of HO_2 signal to number concentration of Fe_2SiO_4 MSP analogue particles (at 9.9 % RH with an injector to detector distance of 70 cm). (b) Example plot showing the HO_2 signal variation with Fe_2SiO_4 aerosol number concentration, also at 9.9 % RH for three fixed contact times as shown in the legend. Means and standard deviations of three condensation particle counter and FAGE measurements are shown (as points and error bars, respectively).

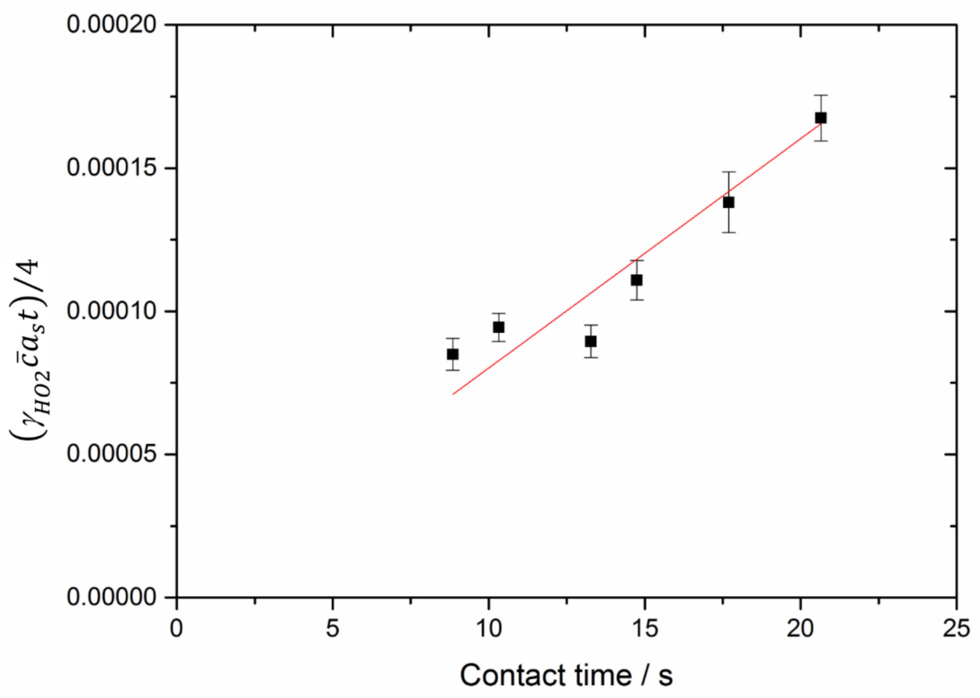

Figure 3.3 Plot of the dimensionless quantity $(\gamma_{HO2}\,\bar{c}\,a_s\,t)\,/\,4$ as a function of reaction time for uptake of HO_2 onto fayalite at a RH = 9.9%. The linear least-squares fit to these point yields $(\gamma_{HO2}\,\bar{c}\,a_s)\,/\,4$ as the gradient; $(6.3 \pm 1.4) \times 10^{-6}$ in this case; from which $\gamma_{HO2} = (7.3 \pm 0.4) \times 10^{-2}$ was obtained. The error bars represent 2 standard deviations in the individual exponential fits, examples of which are given in Figure 3.2 (b).

Table 3.2 Uptake coefficients measured in the laboratory.

MSP analogue (see Chapter 2)	Gas-Phase species	H_2O conditions	Uptake Coefficient
$MgFeSiO_4$	HNO_3	Dry	0.0018 ± 0.0003
$MgFeSiO_4$	HNO_3	Pre-saturated	0.0019 ± 0.0005
$MgFeSiO_4$	HO_2	10 % RH	0.069 ± 0.012
$MgFeSiO_4$	HO_2	20 % RH	0.186 ± 0.017
Fe_2SiO_4	HO_2	9.9 % RH	0.073 ± 0.004
Mg_2SiO_4	HO_2	11.6 % RH	0.0043 ± 0.0004

Although H_2O readily coated the surface of the MSP analogues (see Figure 3.1 (a)), pre-saturating the surface with H_2O was found to have a negligible effect on the measured γ_{HNO3}. This suggests that the two species occupy different active sites on the surface. In the atmosphere, then, uptake of H_2O may not significantly affect the uptake of HNO_3.

γ_{HO2} was found to strongly depend on the conditioning RH (increasing by a factor of ~2.5 between 10 and 20 % RH). Recent measurements have shown that HO_2 uptake tends to be more rapid for higher RH (See Figure 3 in *Lakey et al.* [2015] and Figure 6 in *Matthews et al.* [2014]. This is either due to dissolution of Transition Metal Ions (TMI, although note that as droplet size increases the concentration of TMI decreases so that the uptake would begin to reduce again in large droplets) or a $HO_2.H_2O$ complex may form on the surface and react more rapidly than HO_2 radicals in a similar mechanism [*Stone and Rowley*, 2005]. As the ambient conditions move toward the low RH present in the middle atmosphere (see Figure 3.5 (e)) a kinetic steady state will be reached where a mechanism not involving H_2O will dominate. This will cause the uptake coefficient to stabilise, as seen for example in measurements on humic acid (Figure 3 in *Lakey et al.* [2015]). Measurements of γ_{HO2} at lower RH could not be carried out since H_2O is required to produce HO_2 in the experiment. The uptake coefficient of ~0.07 measured on $MgFeSiO_4$ and Fe_2SiO_4 likely holds for lower RH at room temperature.

At colder atmospheric temperatures the uptake coefficient is likely to increase. If the rate determining step in the uptake process is accommodation on the surface then γ will be identical to the accommodation coefficient, which is known to increase at lower temperatures [*Hayward et al.*, 1967]. If there is a significant thermodynamic barrier to uptake, for example if a chemical reaction is required, then the reverse temperature dependence may be true. In Section 3.2.6 it is argued that there are not likely to be significant energy barriers on the reaction surface of the HO_2 uptake process, so the former temperature dependence is the more likely. Uptake coefficients as shown in Table 3.1 were therefore chosen to determine whether uptake of HNO_3 or HO_2 can significantly perturb the atmosphere.

3.2 Results

3.2.1 Evaluation of SD-WACCM

To assess the validity of SD-WACCM as a tool for atmospheric modelling, January 2005 monthly and zonally averaged data from the control run is compared to measurements from the Mesospheric Limb Sounder (MLS) radiometer aboard the AURA satellite in Figure 3.4. The model data have been sampled using the averaging kernels from the satellite data to facilitate a like with like comparison. There is broad agreement in the magnitude and in the latitude and altitude trends of both species.

Since evaluating WACCM's ability to accurately model the atmosphere is not an aim of this thesis, detailed comparisons of these data will not be made here, though they are present in the literature [*Livesey et al.*, 2011; *Millán et al.*, 2015]. Here we will simply say that WACCM is considered a suitable tool for assessing whether introduction of a new process significantly perturbs the model, and therefore whether that process is likely to be important in the atmosphere.

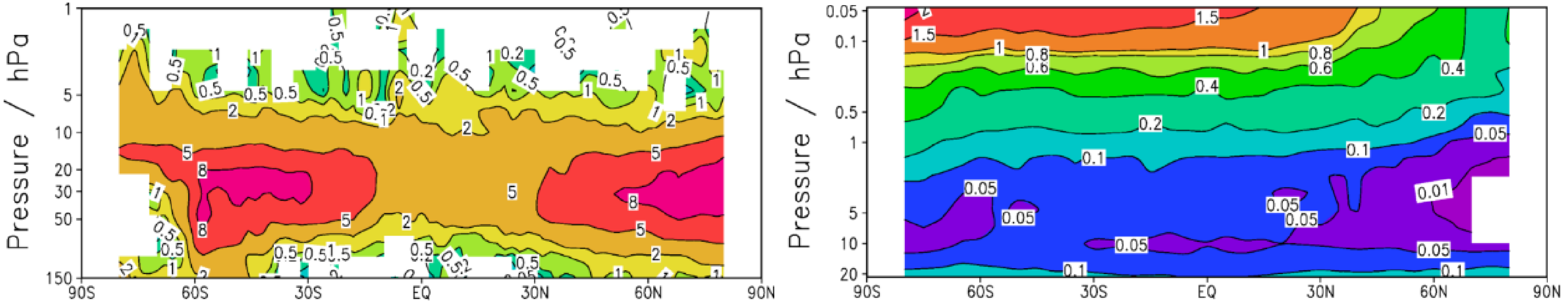

(a) MLS HNO_3

(c) MLS HO_2

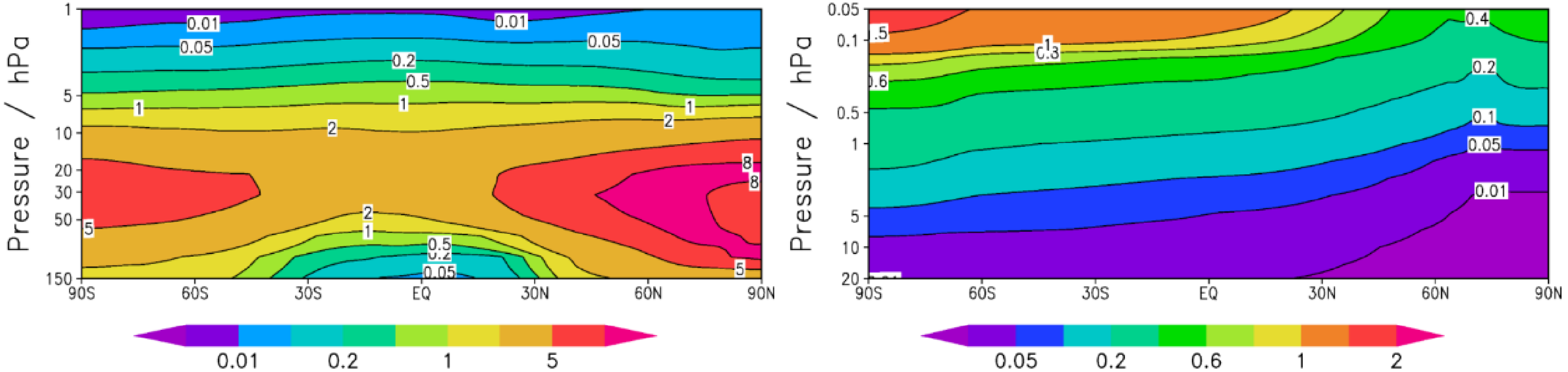

(b) WACCM HNO_3

(d) WACCM HO_2

Figure 3.4 Comparison of abundance (ppb) of HNO_3 and HO_2 from a WACCM-CARMA control run (without any heterogeneous uptake, bottom panels) to observations from the MLS radiometer aboard the AURA satellite. HNO_3 is shown in the left panels and HO_2 on the right. WACCM data has been sampled at the same averaging kernels as the observations. Colour bars shown apply to both panels vertically and should be interpreted with care since non-linear colouring has been used to accentuate some features.

3.2.2 First Order Effects of Uptake

The effect of introducing heterogeneous uptake is shown in Figure 3.5. Percentage differences in mixing ratio from the control run, zonally averaged at 80° S are shown for the (a) HNO_3 measured, (b) HNO_3 T, (c) HNO_3 max and (d) HO_2 runs. Percentage Relative Humidity (RH, panel (e)) and available surface area of MSPs / μm^2 cm^3 (f) are also shown for information. Losses of both HNO_3 and HO_2 clearly correlate to the presence of MSPs, with both occurring in the winter months as mesospheric air masses travel down the polar vortex. The effect of the uptake coefficient is demonstrated in comparison of panels (a), (b) and (c). At γ_{HNO3} = 0.002, some periodic loss of HNO_3 was observed at and below the 5 hPa, at γ_{HNO3} = 0.02 this increases to almost complete (>80 %) loss with the effect also visible at all altitudes in some years and at $\gamma_{HNO3} = 1$ this almost complete loss is evident at all altitudes. A periodic loss of up to 60 % of HO_2 was also observed between 1 and 0.1 hPa (panel (d)). Similar trends are seen in the Northern polar winter (data not shown), but are complicated by the variability of the boreal polar vortex.

There is a notable difference in the altitude behaviour of HNO_3 and HO_2. Whilst reactive uptake removes HNO_3 over the full altitude range investigated, HO_2 only changes significantly above 1 hPa. This implies that a different loss mechanism is dominant for HO_2 at lower altitudes; however for HNO_3 no other mechanism considered is faster than heterogeneous uptake. Regional trends in the results are discussed below in light of their latitude dependence (Figure 3.7).

Since both experimental studies showed the importance of the presence of H_2O, the percentage RH from the control run is shown in panel (e). This shows that this region of the upper stratosphere and mesosphere is remarkably dry, with significant RH occurring only in the summer mesosphere and winter stratosphere. HNO_3 uptake was shown to be independent of pre-saturating the MSP analogue surface with H_2O (see Section 3.1.3), implying that the significant H_2O concentrations concurrent with the MSP presence likely do not impact on the HNO_3 loss. Since HO_2 loss is confined to higher altitudes and winter months, the uptake process will likely proceed *via* a mechanism which does not involve H_2O. The presence of H_2O and other species is also discussed further below in light of the latitude dependence and mechanisms of uptake (Figure 3.7 and Section 3.2.6, respectively).

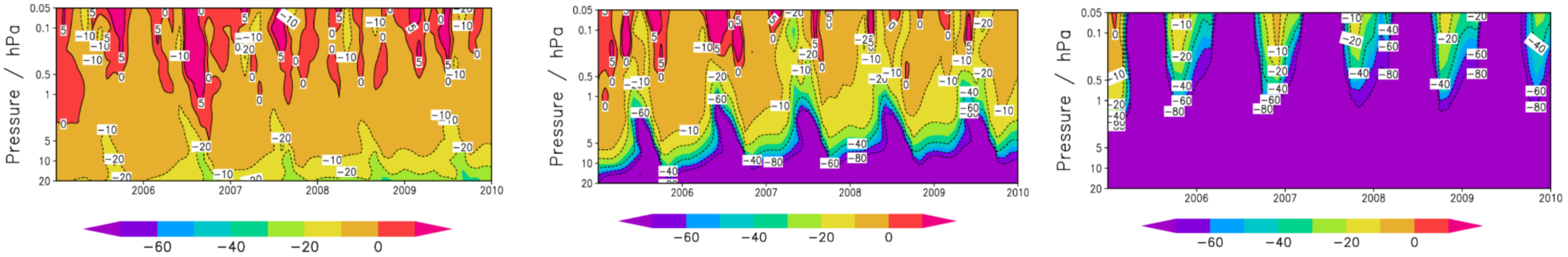

(a) % change in HNO$_3$, γ_{HNO3} = 0.002 (b) % change in HNO$_3$, γ_{HNO3} = 0.02 (c) % change in HNO$_3$, γ_{HNO3} = 1

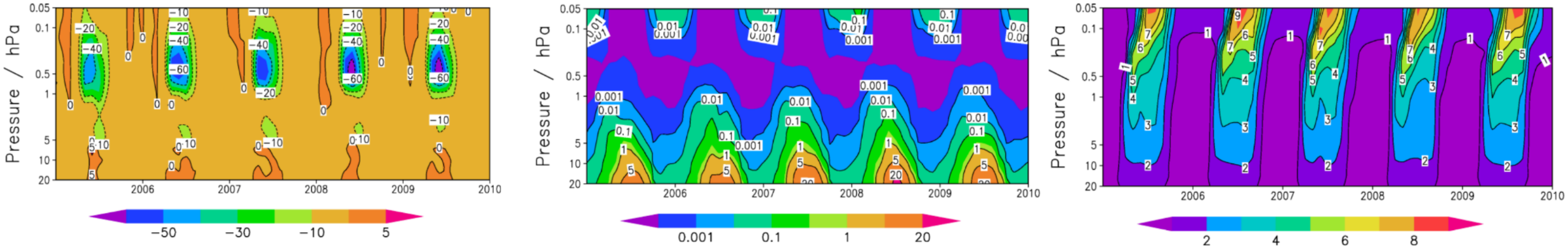

(d) % change in HO$_2$, γ_{HO2} = 0.2 (e) % RH, control run (f) available surface of MSPs / μm^2 cm^{-3}, control run

Figure 3.5 % difference in mixing ratio between control run and runs with (a) HNO$_3$ uptake using the measured uptake coefficient (HNO$_3$ measured), (b) HNO$_3$ uptake with a 10 fold increase on the measured uptake coefficient to account for temperature dependence (HNO$_3$ T), (c) HNO$_3$ with the maximum uptake which is physically possible (HNO$_3$ max) and (d) HO$_2$ with an uptake coefficient ~3 times larger than that measured, to account for temperature dependence. % relative humidity (e) and the available surface area of MSPs / μm^2 cm^{-3} (f) from the control run are shown for information. All data are shown zonally averaged at 80° S. Colour bars should be interpreted with care since non-linear colouring has been used to accentuate some features.

3.2.3 Trends in the Effects of Uptake

Figure 3.6 shows the percentage change in HNO_3 at the 10 hPa level, zonally averaged at 80° S with means of August 2007-2009 shown as data points and standard deviations as error bars. The dashed line is a guide to the eye, showing that at low γ_{HNO3}, the loss of HNO_3 is more sensitive to γ_{HNO3} than at higher γ_{HNO3}, where availability of HNO_3 becomes rate limiting. Such sensitivity is advantageous in atmospheric modelling of the uptake process, given that the temperature dependence of γ_{HNO3} is difficult to quantify experimentally (see Section 3.1.3). Where suitable atmospheric observations are available, this could be used to quantify the most appropriate γ values for atmospheric modelling (see Chapter 6).

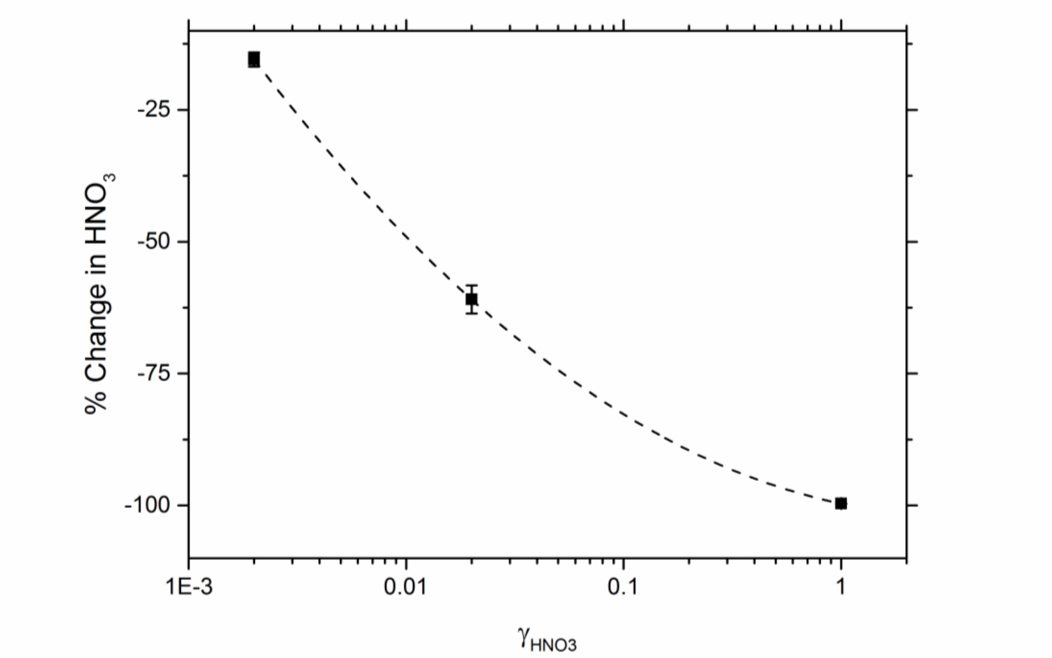

Figure 3.6 % change in HNO_3, zonally averaged at 80° S and 10 hPa. Points are the mean of August 2007, 2008 and 2009 with standard deviations shown as error bars. The dashed line is simply a guide to the eye, showing that at higher γ_{HNO3} the impact on atmospheric HNO_3 is less sensitive to changes in γ_{HNO3}.

Figure 3.7 shows the latitude dependence of the percentage difference in HNO_3 (panels (a),(b) and (c)) and HO_2 (d), zonally averaged for June 2009. The difference evident between HNO_3 and HO_2 in the altitude dependence over time is also seen here. This is reasonable since the major loss pathways (aside from heterogeneous uptake, see Section 1.2 and Figure 1.6 [*Brasseur and Solomon*, 1998]) for HNO_3 are photolysis and reaction with OH which do not occur in the dark polar vortex (photolysis lifetime of HNO_3 is 10^4 s above 1 hPa in the summer but photolysis is negligible in the winter and typical OH concentrations at 1 hPa near the poles in the control run are on the order of $1 \times 10^3\ \mathrm{cm^{-3}}$ in winter, which given the rate coefficient $b_{27} = 7.2 \times 10^{-15} \exp(785/T)$ molecules^{-1} cm^3 s^{-1} implies a lifetime for HNO_3 destruction by OH which is longer than the winter months). For HO_2 though, the major loss pathway is chemical reaction with O_3, which is competitive in the polar vortex (typical winter O_3 concentrations at 1 hPa near the poles on the order of $1 \times 10^{10}\ \mathrm{cm^{-3}}$ and rate coefficient of $1.4 \times 10^{-14} \exp(-580/T)$ molecules^{-1} cm^3 s^{-1} giving e-folding lifetimes of approximately 1 day).

This is significant since removal of HNO_3, as demonstrated here but not included in the HO_2 run, will have impacts on other species, particularly NO_x and O_3 (see Section 3.2.4), and therefore by slowing chemical loss could alter the importance of heterogeneous uptake relative to gas-phase loss of HO_2.

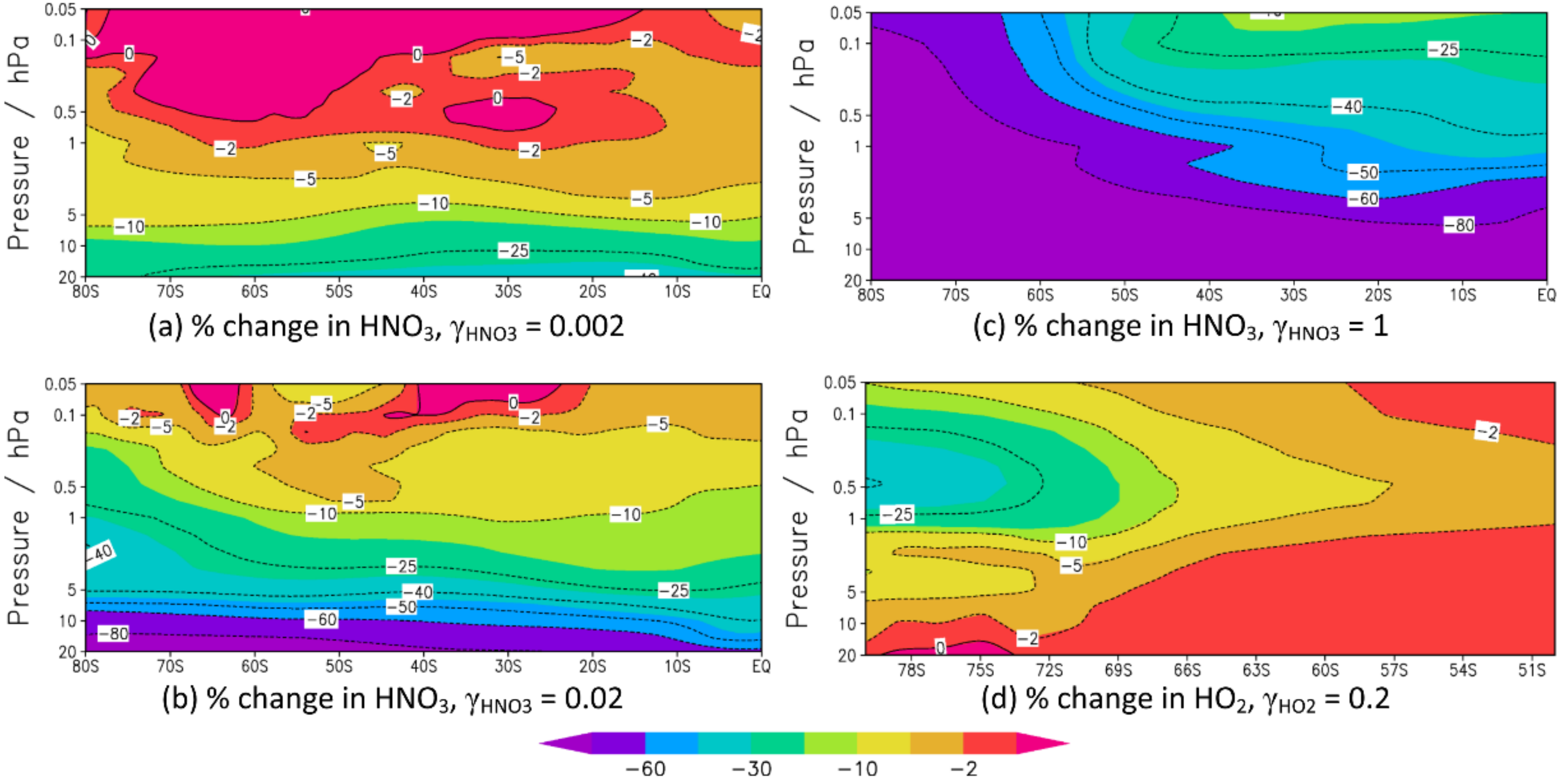

(a) % change in HNO_3, $\gamma_{HNO3} = 0.002$

(c) % change in HNO_3, $\gamma_{HNO3} = 1$

(b) % change in HNO_3, $\gamma_{HNO3} = 0.02$

(d) % change in HO_2, $\gamma_{HO2} = 0.2$

Figure 3.7 Latitude dependence of % difference in mixing ratio for June 2009 between the control run and runs (a) HNO_3 measured, (b) HNO_3 T, (c) HNO_3 max and (d) HO_2. For HNO_3 the entire southern hemisphere is affected, whereas for HO_2 the loss due to heterogeneous uptake is negligible at latitudes lower than ~50° S. The colour bar shown applies to all panels and should be interpreted with care since non-linear colouring has been used to accentuate some features.

One important implication of the fact that HNO_3 uptake affects all latitudes is that the impact could be cumulative over multiple years as air masses depleted in HNO_3 and associated species are able to spread throughout the atmosphere. Such a cumulative effect is not observed in the WACCM runs, suggesting that the various sources of these species throughout the year are able to compensate for the loss of HNO_3 in the winter polar vortex. The lack of treatment of interactions of MSP with H_2SO_4 and H_2O are also important here, since coating of surfaces and, eventually, incorporation into stratospheric sulfate aerosol will make the active surfaces of MSP inaccessible to HNO_3. The uptake of H_2SO_4 in the atmosphere has been investigated previously and found to occur below 40 km (~2 hPa) [*Neely et al.*, 2011; *Saunders et al.*, 2012]. This means that much of the uptake observed at lower altitudes and after transport to lower latitudes is likely spurious. Nevertheless, in the HNO_3 T and HNO_3 max runs there is a clear change above this altitude. Considering these two uptake processes in isolation and without treatment of the interaction between MSP and H_2SO_4 will not be sufficient to quantify these impacts, particularly in relation to the temperature dependence of γ. As a result, no comparison is made in this study between the results of SD-WACCM runs and atmospheric observations, with a view to quantifying the loss of HNO_3 to MSPs and ultimately the MIF. Re-evaluating HNO_3 uptake to MSPs in a model which treats the MSP/H_2SO_4 interaction is clearly a topic for future work (see Chapter 6).

3.2.4 Indirect Effects of Uptake on Other Species

Such extreme removal of a chemical species has clear implications for related chemistry, as discussed in Chapter 1 (See Figure 1.6). To understand the importance of these uptake processes in the atmosphere it is necessary to consider them in relation to other production and loss processes of those species. It is also likely that removal of one species will have indirect implications for other species. Figure 3.8 shows percentage difference in NO_2 (for all 3 HNO_3 runs, panels (a-c)) and total NO_x (for the HNO_3 T and HNO_3 max runs, panels (e) and (f)) along with NO_2 as a percentage of the total NO_x (primarily NO and NO_2 but also including NO_3 and N_2O_5) mixing ratio in the control run (d).

Significant losses are seen in both NO_2 and NO_x. Interestingly, the loss of these species occurs in the summer months. This is because the conversion from HNO_3 to other NO_x species is *via* photolysis to NO_2 and OH, which cannot occur in the dark winter vortex (see Section 3.2.3). The seasonal nature of this loss means that air from lower altitudes has more opportunity to mix to the altitudes at which significant loss was observed, implying that the interaction of MSPs with H_2SO_4 is likely more important here and that this therefore represents an upper limit to the effect.

NO_2 and NO_x show remarkably similar behaviour, despite the dominant species varying over seasons and altitudes. This suggests that in the summer months at least there is relatively rapid exchange between the various NO_x species. Reduction from $NO_2 \rightarrow NO$ is facilitated by photolysis (lifetime at 1 hPa on the order of 100 s in summer), whilst NO is oxidised to NO_2 by O_3 with a minor contribution from ClO (lifetimes at 1 hPa near the winter poles of several hours and several days, respectively). Hence a removal of HNO_3 by MSPs can be considered a more general removal of oxidised reactive nitrogen species along with the O_3 required to produce NO_2 from NO (and some formation of Cl from ClO), and the OH which reacts with NO_2 to produce HNO_3. *Frankland et al.* [2015] also observed a direct uptake of NO_2 to MSP analogues, which has not been tested for atmospheric significance to date.

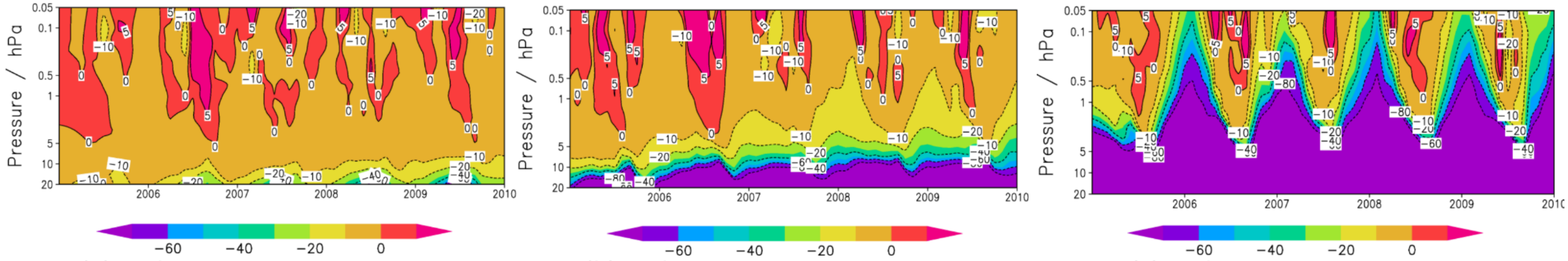

(a) % change in NO_2, γ_{HNO3} = 0.002

(b) % change in NO_2, γ_{HNO3} = 0.02

(c) % change in NO_2, γ_{HNO3} = 1

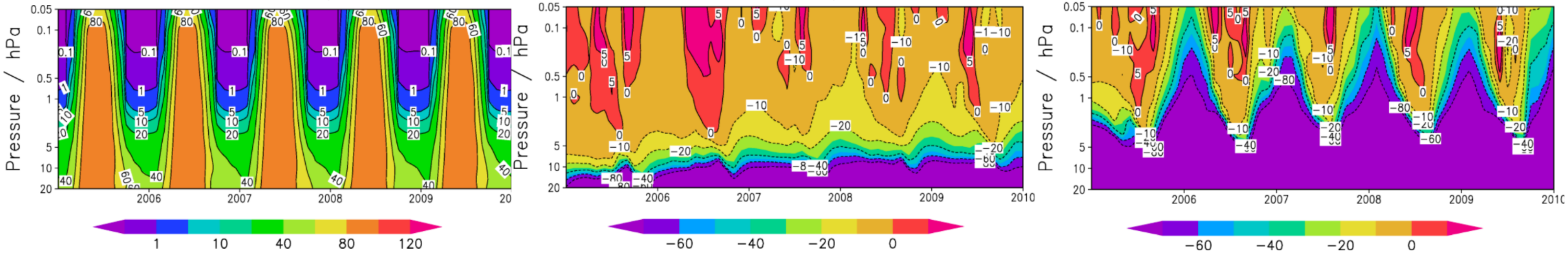

(d) NO_2 as % of NO_x, control run

(e) % change in NO_x, γ_{HNO3} = 0.02

(f) % change in NO_x, γ_{HNO3} = 1

Figure 3.8 Effect of HNO_3 removal on other species: % difference in NO_2 mixing ratio between control run and runs (a) HNO_3 measured, (b) HNO_3 T, (c) HNO_3 max, (d) NO_2 as a percentage of total NO_x and % difference in total NO_x mixing ratio for (e) HNO_3 T and (f) HNO_3 max. All data are shown zonally averaged at 80° S. The colour bars should be interpreted with care since non-linear colouring has been used to accentuate some features.

HO_2, meanwhile, is produced from the reaction of H and O_2 (which requires a third body collision partner) and is equilibrated with OH *via* O_3. Removal of HO_2 therefore implies removal of OH, which will slow production of HNO_3 from NO_2. This provides a link between the chemistry of HO_2 and HNO_3, suggesting that there may be additional implications of both uptake processes occurring simultaneously. This chemistry is summarised in Figure 1.6, reproduced from *Brasseur and Solomon* [1998].

3.2.5 Interactions Between HO_2 and HNO_3

There are clear chemical links between the two species investigated here (see Section 1.2). Figure 3.9 shows the percentage change in HO_2 in the HNO_3 measured and HNO_3 T runs and the percentage change in HNO_3 in the HO_2 run. All runs show some effects of the chemical relationship between the two species. Removal of HO_2 leads to reduced HNO_3 since HO_2 is in equilibrium with OH, which reacts with NO_2 to produce HNO_3. This would reinforce the HNO_3 loss observed if both uptake processes occurred simultaneously. Removal of HNO_3 will have a more subtle effect on HO_2, since the effect on other NO_x species will be delayed until the summer months. Following this seasonal change, reduced NO_x will lead to increased HO_2, since NO_2 reversibly reacts with HO_2 to give HO_2NO_2 (note the similar pattern of NO_2 loss in Figure 3.8 (b) and HO_2 gain in Figure 3.9 (b), particularly the extreme values in 2006 and 2009).

Since the observed change in HO_2 is confined to relatively low altitudes, it is likely subject to biases caused by the lack of treatment of deactivation of MSPs by H_2SO_4. The negligibly small effect of HNO_3 uptake on HO_2 at altitudes above 1 hPa also means that HNO_3 uptake is not likely able to reconcile HO_2 modelling with observations (see Figure 1.5). Coupled with the interactions between reactive species there is clearly scope for a future project to investigate the combined effect of both uptake processes, including a treatment of the interaction between H_2SO_4 and MSP.

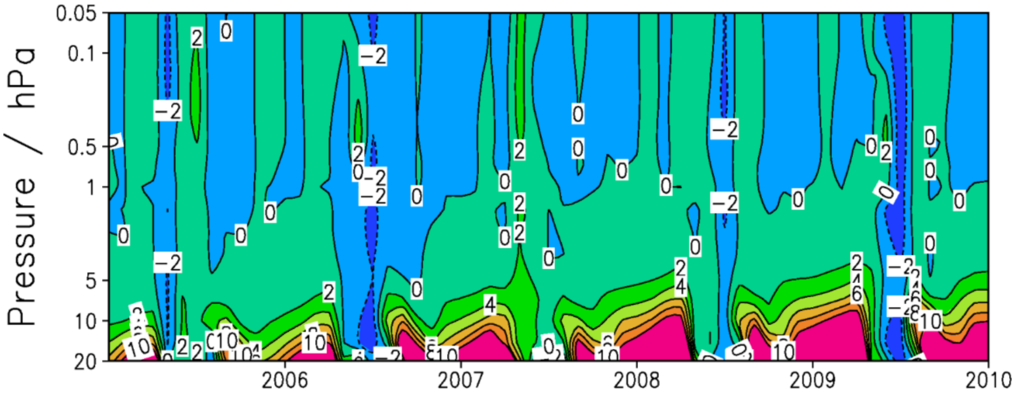

(a) % difference in HO_2 with γ_{HNO3} = 0.002

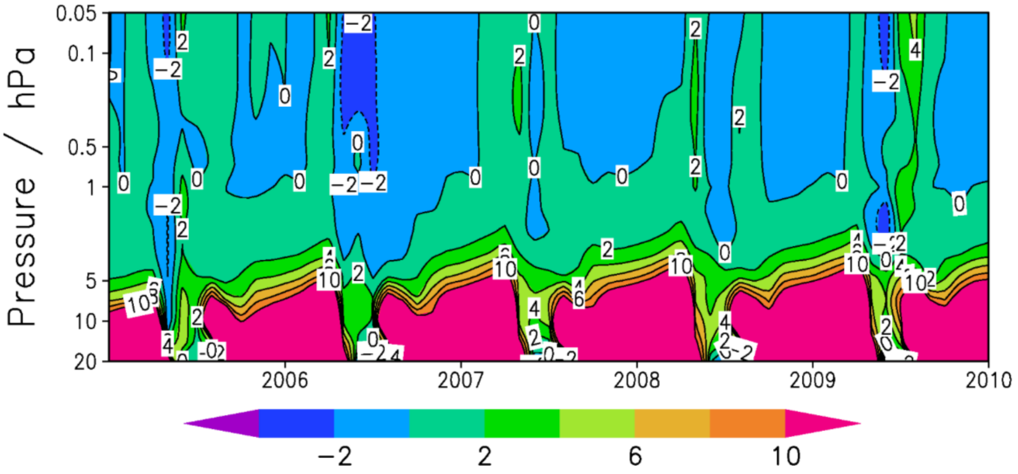

(b) % difference in HO_2 with γ_{HNO3} = 0.02

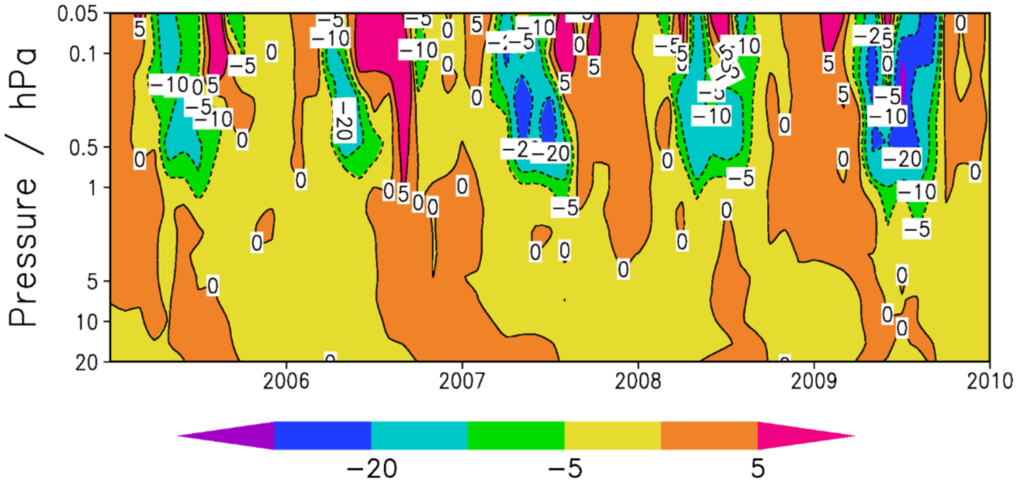

(c) % difference in HNO_3 with γ_{HO2} = 0.2

Figure 3.9 Relationship between HNO_3 and HO_2: % difference in HO_2 mixing ratio zonally averaged at 80 ° S between control run and runs (a) HNO_3 T, (b) HNO_3 max, (c) % difference in HNO_3 between control and HO_2 run. The colour bar on (b) also applies to (a) and both colour bars should be interpreted with care since non-linear colouring has been used to accentuate some features.

3.2.6 Effect of Uptake on MSPs

Uptake of species to a surface has the potential to block active sites, changing the nature of the material and, in the extreme, coating the surface completely. For example it has been shown that acetylene likely covers the surface of IDPs as they sediment through Titan's atmosphere, until at lower altitudes sufficient temperatures are reached for cyclo-trimerisation to convert the acetylene to benzene [*Frankland et al.*, 2016].

In this global modelling study no change to the MSPs has been considered as a result of uptake of HNO_3 or HO_2. It has been shown in the past that an additional 2-5 ppb of alkaline metals globally would be able to completely neutralise stratospheric HNO_3 [*Prather and Rodriguez*, 1988]. Above 2 hPa, where H_2SO_4 should not significantly affect uptake, HNO_3 mixing ratios in the control simulation are typically less than 0.1 ppb (see Figure 3.4 (b)). Assuming that MSPs are 46 % Fe or Mg by mass (olivine composition) then the mixing ratio of these metals in the middle atmosphere is around 5 ppb. This suggests that there will not be sufficient HNO_3 to alter the uptake efficiency of MSPs.

Electronic structure calculations, performed at UoL (see acknowledgements) suggest that HO_2 taken up to MSPs is likely to be highly reactive with gas-phase HO_2, leading to a catalysis of the HO_2 self-reaction, producing H_2O_2 without deactivating MSP active sites. Figure 3.10 shows that when an HO_2 binds to an Fe, a second HO_2 is able to abstract the H atom of the chemisorbed adduct, and that a third HO_2 is then able to displace the O_2 left bound to the surface. All steps of this process are exothermic and lack significant thermodynamic barriers, suggesting that the uptake coefficients measured in the laboratory represent accommodation coefficients for HO_2 from the gas phase onto HO_2 adsorbed to Fe atoms on the particle surface (reaction step from Figure 3.10 (b) to (c)) and that the uptake coefficient will therefore likely increase with decreasing atmospheric temperature.

Interestingly, if the initial HO_2 binds to an Mg site, the H migrates to an adjacent O, forming a very stable structure. Further HO_2 are unable to interact with this Mg and the site is deactivated. This may explain the much smaller γ_{HO2} measured on Mg_2SiO_4 compared to the Fe containing analogues.

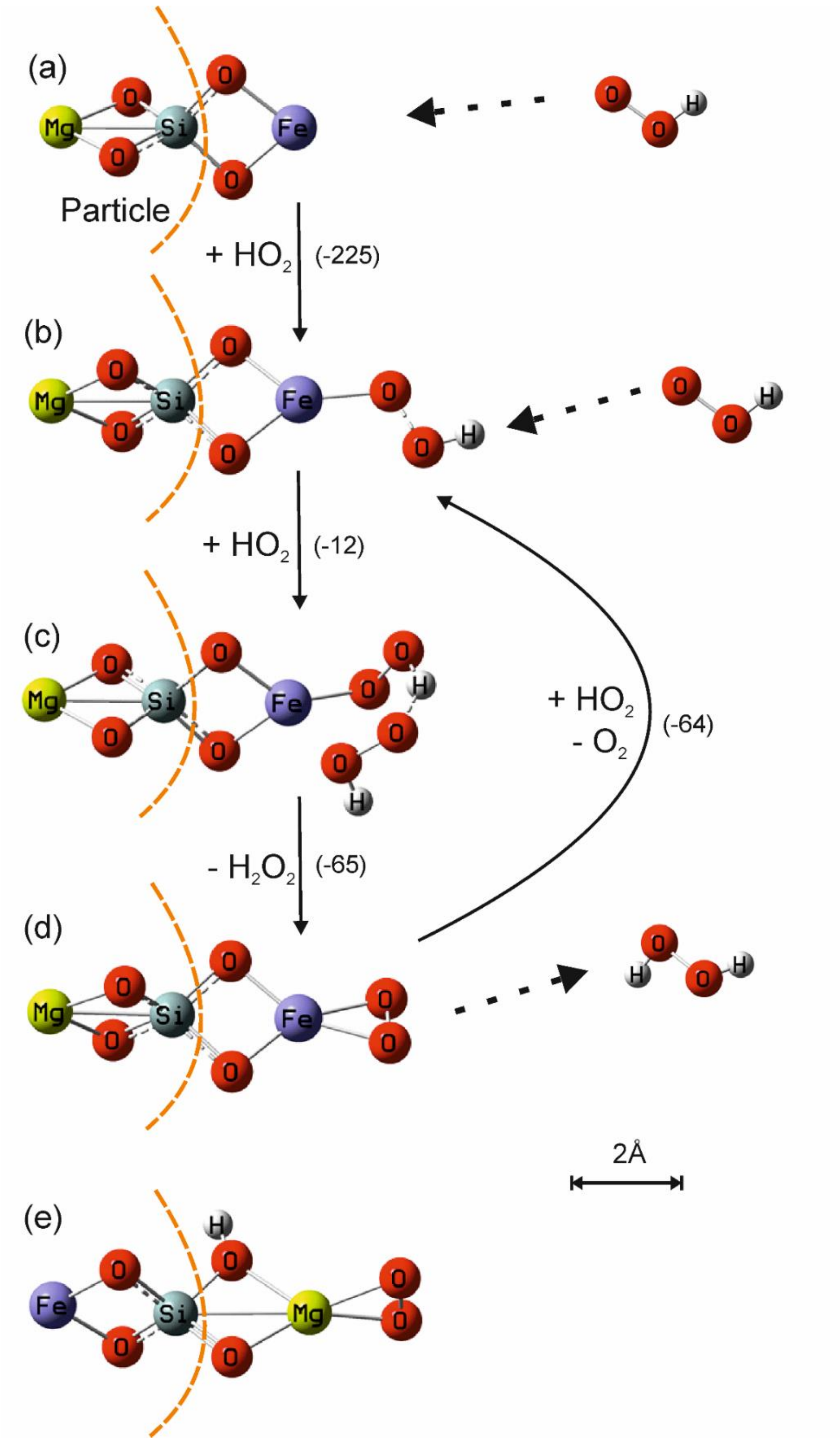

Figure 3.10 Electronic structure calculations at the B3LYP/6-311+g(2d,p) level of theory with enthalpies in kJ mol^{-1} in brackets: (a) HO_2 uptake on an exposed Fe atom on the $MgFeSiO_4$ surface leads to a chemisorbed adduct (b); a second HO_2 can now abstract the adsorbed H atom *via* transition state (c) to form (d), where O_2 is bound to the Fe atom, which can then be displaced by a further HO_2 to yield (b). When HO_2 adds to an exposed Mg atom, chemisorption leads to the very stable structure (e).

3.3 Conclusions

This work has shown that both HNO_3 and HO_2 may be perturbed in the polar vortex by reactive uptake onto MSPs. Whilst the effect on HO_2 is confined to the polar vortex, with other loss processes dominating elsewhere, the effect on HNO_3 was observed over the entire winter hemisphere. This effect is overestimated below 2 hPa, because the model did not include a treatment of the interaction of MSPs with H_2SO_4, which will coat and deactivate the MSP surfaces.

Uptake processes of these few species have wide ranging effects on a variety of chemistry in the middle atmosphere, including feedbacks on each other.

A further study is therefore timely, which investigates these uptake processes in tandem with H_2SO_4 and direct NO_2 uptake. Future studies should also aim to constrain the atmospheric uptake coefficients, particularly their temperature dependences, by comparing output from there more sophisticated modelling studies to atmospheric observations of species which are directly or indirectly impacted by the uptake processes.

Chapter 4

Nucleation of Nitric Acid Hydrates Under Conditions Relevant for Polar Stratospheric Clouds

The phase chemistry and nucleation kinetics of solid Polar Stratospheric Clouds (PSCs) are a significant uncertainty in atmospheric modelling of chemistry in the polar vortex and particularly of the ozone hole [*Brakebusch et al.*, 2013]. As discussed in Sections 1.3 and 2.3.2, nucleation of crystalline phases in PSCs likely proceeds heterogeneously on silica, following dissolution of other components of meteoric smoke particles. Here we present laboratory measurements of heterogeneous nucleation kinetics relevant to PSCs, parameterisations of the data and comparison of the results to the observed concentrations of crystalline aerosols in PSCs.

Kinetic parameterisations assuming Nitric Acid Dyhydrate (NAD) nucleated first showed significant trends. Similar trends where not observed when Nitric Acid Trihydrate (NAT) was assumed to form first, suggesting that NAD is the primary nucleating phase. XRD experiments showed that within 10 min at stratospheric temperatures all crystalline phases had converted to NAT, suggesting that liquid mediated phase transformation had occurred.

Treating the heterogeneous surfaces as having a uniform activity and using the classical nucleation theory to calculate heterogeneous nucleation rate coefficients, J_{het}, leads to an over prediction of crystal concentrations in PSC since the time dependence of nucleation is over predicted. Conversely, parameterising the laboratory data by the cumulative density of sites which are active at temperatures higher than the current temperature, n_s, under predicts crystal concentrations in PSC, possibly since the time dependence is neglected. Further experiments are needed in order to quantify the time dependence of the nucleation process and produce a parameterisation which can be used in atmospheric models.

4.1 Methods

Two drop freeze assay techniques were used to examine nucleation in droplets under conditions relevant to PSCs. The first set of experiments probed the kinetics of nucleation as a function of temperature, concentration of HNO_3, $[HNO_3]$, and availability of heterogeneous SiO_2, thought to be a good analogue for MSPs processed in acid sulfate aerosol (see Section 2.3.2). The second set of experiments examined the phases which following nucleation.

In the first set of experiments, a drop freeze assay technique developed to examine nucleation of H_2O ice in the troposphere was adapted for conditions relevant to PSCs. Nucleation events were observed using a video camera (Microsoft Lifecam HD). Temperature was controlled by a Stirling engine (Grant -Asymptote, EF600). Temperature was measured by a PID sensor (Eurotherm 2416) embedded in the cooling stage of the EF600 and confirmed by a calibrated temperature probe (netsushin PT100), inserted into an aluminium block between the sample and the EF600 cold stage. Temperature and video frame were both logged digitally along with the computer clock so that the temperature in each video frame was known. 20-30 one µl droplets were pipetted (Ependorff, multipette plus) onto a hydrophobic silanised glass slide (Hampton Research HR3-231), a viton o-ring was used as a spacer and the cell was sealed with a second slide (see Figure 4.1 (a)). Nucleation is visible in this system since liquid droplets are transparent, whilst droplets where nucleation has occurred are opaque.

In the second set of experiments, the phase which formed following nucleation was investigated in an X-Ray Diffractometer (XRD, Bruker D8 advance). Droplets were pipetted onto a glass slide and covered with a piece of Kapton film (0.3 mm thickness, Certiprep), separated from the substrate slide by a viton o-ring. The sample was placed on an Al block and cooled by a flow of liquid N_2 (Anton Parr TTK450 temperature controlled stage). Scans with a fixed 2-θ range of 10 °, centred on 36 °, with 1 min integration of signal (*i.e.* one scan K^{-1}) were performed throughout cooling and warming ramps. The minimum temperature was held for 10 min to allow a wide angle scan to be collected.

Suspensions of fumed SiO_2 (99.8 %, Aldrich, BET surface area of 195 m^2 g^{-1}) in ultra-pure H_2O (milli-Q) were made up by stirring for at least 12 hours. These suspensions (or pure H_2O, similarly stirred) were then used to dilute HNO_3 (65%, AnalaR NORMAPUR) to the desired concentration. Control experiments were carried out in which no SiO_2 was added investigated the effect of adding SiO_2.

1 µl droplets were then pipetted onto the substrate slide within the viton spacer, and the cell sealed. This volume of droplet was chosen by estimating the atmospheric n_s and calculating the surface area per droplet required to probe this n_s in laboratory experiments, assuming 1 wt % of a heterogeneous material with a surface area of 200 m^2 g^{-1}.

Experiments were mainly carried out at the highest HNO_3 concentrations reached in the atmosphere in the absence of significant gravity wave activity [*Carslaw et al.*, 1997]. When gravity waves cause rapid cooling of the stratosphere, non-equilibrium conditions can occur whereby higher concentrations are reached [*Meilinger et al.*, 1995]. However, in such rapidly cooling air masses, H_2O ice is likely to form and facilitate β-NAT formation [*Koop et al.*, 1995]. This study aims to investigate formation of solid PSCs under synoptic conditions (without gravity wave perturbations). Concentrations were therefore chosen which covered the region where (at stratospheric temperatures) H_2O ice is not stable ($[HNO_3]$>42 wt %) and similar concentrations where H_2O ice is stable (39 wt % >$[HNO_3]$<42 wt %).

Droplet arrays in both setups were cooled at 3 K min^{-1} from room temperature to 230 K and then at 1 K min^{-1} to 182 K (base temperature for the EF600). Warming was then carried out at 1 K min^{-1} to 250 K , to observe melting of H_2O and Nitric Acid hydrate (NAX) phases. To prevent water ice formation in both experimental setups, a flow of dry zero-grade N_2 (BOC) was passed over the sealed cell during cooling until ~230 K, and the cell isolated at lower temperatures. This cooling rate is significantly faster than the synoptic stratosphere (where cooling of several K can take 10-20 hours [*Hoyle et al.*, 2013]) but has been chosen since longer experiments (at slower cooling rates) would not allow collection of a statistically large dataset within a reasonable time frame.

4.2 Results

4.2.1 Observed Crystallisation

Nucleation events were observed in all EF600 experiments, with transparent droplets turning to opaque crystals. The video frame where opacity was first observed in each droplet was noted and the corresponding stage temperature determined by comparing both data sets to the computer clock. The corresponding S_{NAD} and S_{NAT} values were then calculated using the online Aerosol Inorganic Model (e-AIM) as described in Section 1.3.3 [*Clegg et al.*, 1998].

Figures 4.1 (a-c) show examples of droplet arrays at different stages in the experiment. The droplets do not freeze with any visually discernible spatial pattern, suggesting that the nucleation events are controlled by the contents of the droplets, rather than any temperature gradient across the sample. Observed fraction frozen data from example experiments with addition of SiO_2 are compared to control experiments in Figure 4.1 (d). There is a clear heterogeneous effect when SiO_2 is added. Indeed, the temperature at which events were observed was found to be dependent on the available amount of SiO_2 and on $[HNO_3]$. Figure 4.1 (e) shows the data set compared to the melting curves for H_2O ice and NAD. The temperatures at which events were observed falls off from the NAD melting curve, suggesting a trend in the saturation ratio with respect to NAX, S_{NAX} (see Section 1.3.2).

An atmospheric trajectory showing the equilibrium droplet concentrations against temperature of an air mass with 0.4 ppb HNO_3, 0.1 ppb H_2SO_4 and 4 ppm H_2O is shown in Figure 4.1 (e) (see Section 1.3.2 and Figure 1.10). This shows that the majority of experiments are conducted at $[HNO_3]$ which exist in droplets at equilibrium with the synoptic polar stratosphere. Experiments were also carried out at higher concentrations to evaluate nucleation in a region where H_2O ice was not stable.

In many experiments, several drops nucleate either significantly before or significantly after the majority (see Figure 4.1 (d)). These events are caused by rare, highly active sites or a rare lack of active sites respectively. As only a few of these events are observed they are statistically less significant, representing the tails of the Poisson probability distribution for nucleation [*Herbert et al.*, 2014]. Figure 4.1 (e) shows only the 25-80 % frozen data for clarity and some data was systematically disregarded in parameterising the kinetics of nucleation (see Section 4.2.2 for details).

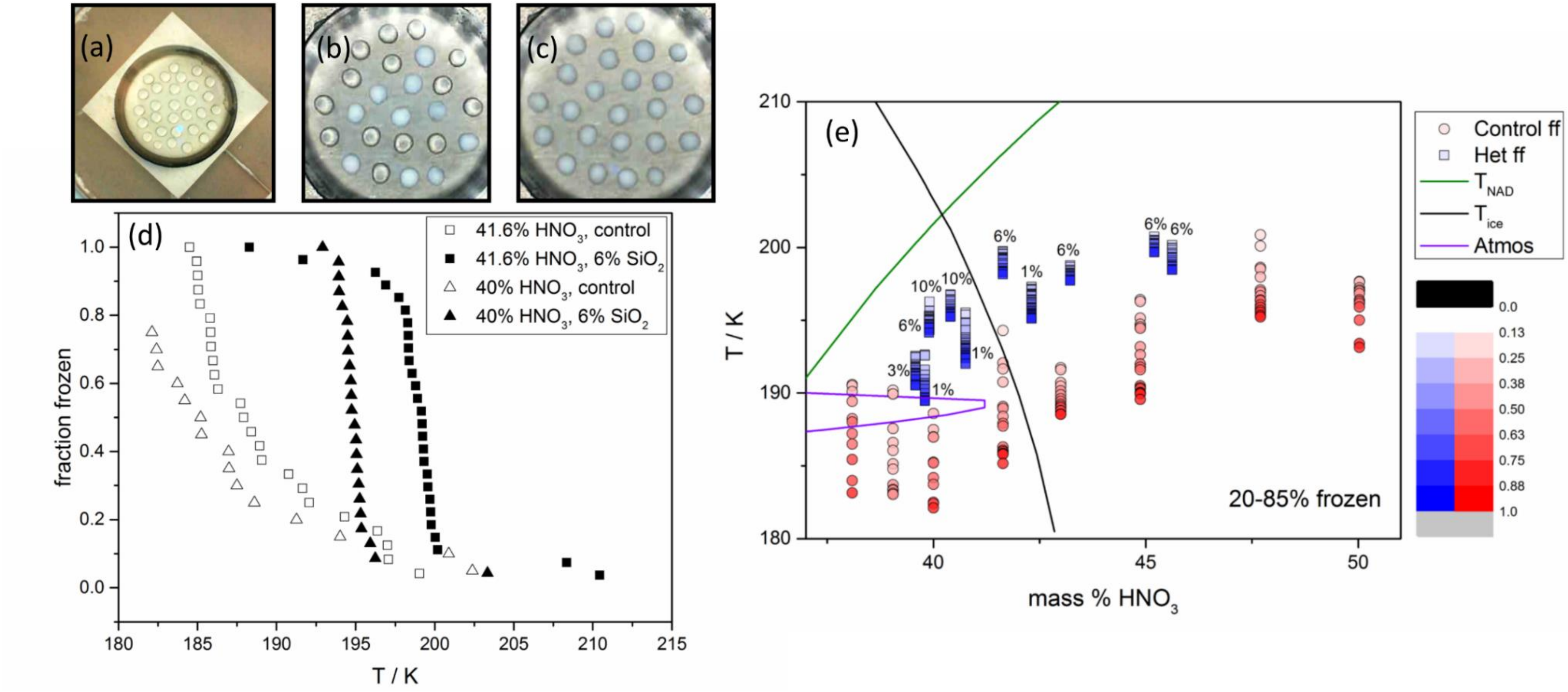

Figure 4.1 (a) an array of particles sealed in the experimental cell, situated on the aluminium cooling stage of an EF600 Stirling engine and fitted with a PT100 temperature sensor. (b) a partially crystallised array of droplets during cooling. (c) a partially melted array of droplets during warming. (d) fraction of droplets frozen at each temperature for control and heterogeneous experiments at several HNO_3 concentrations. (e) Observed fraction frozen (20-85 %) for control (red circles) and heterogeneous (blue squares) experiments. The colour of each point indicates the fraction frozen. Labels indicate the mass percentage of SiO_2 in the aqueous suspension used to dilute the HNO_3. The melting temperatures for NAD and H_2O ice and the equilibrium concentration reached in an atmospheric trajectory (see Section 1.3.2, Figure 1.10 for details) are included for comparison.

Crystalline phases were observed in XRD patterns measured during cooling ramps, at base temperature and on warming. On warming, different experiments show a reproducible XRD pattern. Several patterns measured on warming from 182-183 K are compared to potential constituent phases in Figure 4.2. Good agreement is apparent with a pattern generated from the structure of *β*-NAT [*Taesler et al.*, 1975]. There is some offset in 2-θ, possibly because of sample height displacement. The geometry of the system is such that the stated 2-θ is valid for the surface of the supporting slide. However, the 1 µl droplets used here are around 1 mm deep, so XRD signal from the droplets occurs at slightly lower 2-θ. Patterns observed on cooling and at base temperature vary between experiments (data not shown), suggesting that the rate of heterogeneous nucleation for several phases is competitive or that phase transformation is sometimes too rapid to allow observation of the initially formed phase.

The dependence of nucleation efficiency on the amount of heterogeneous material present is also significant since it implies that contamination of the system is unlikely to be responsible for the observed heterogeneous effect. Possible contamination by material less representative of stratospheric aerosol could lead to a “false positive” identification of an atmospherically relevant material. On the basis of the trends observed here, however, it appears that the SiO_2 was responsible for nucleation in these experiments.

The observations from XRD experiments suggest that, whilst the final phase formed is *β*-NAT, more complex mixtures of phases initially form and subsequently relax to the thermodynamically most stable phase on the timescale of these laboratory experiments (several minutes), which are significantly shorter than the lifetimes of PSCs (days to weeks [*Höpfner et al.*, 2006a]). Phase transformation is likely facilitated by nucleation of several crystalline phases followed by liquid mediated transfer of material to the thermodynamically most stable phase. The observation, in XRD patterns measured on cooling, of competitive nucleation between multiple phases is significant, since multiple nucleation events would be required for this process to occur. This has been proposed in the past in order to explain the dependence of phases formed on the presence of residual liquids [*Murray and Bertram*, 2008]. This is significant since in the atmosphere the residual H_2SO_4 in droplets may remain liquid and be available to mediate phase transformation.

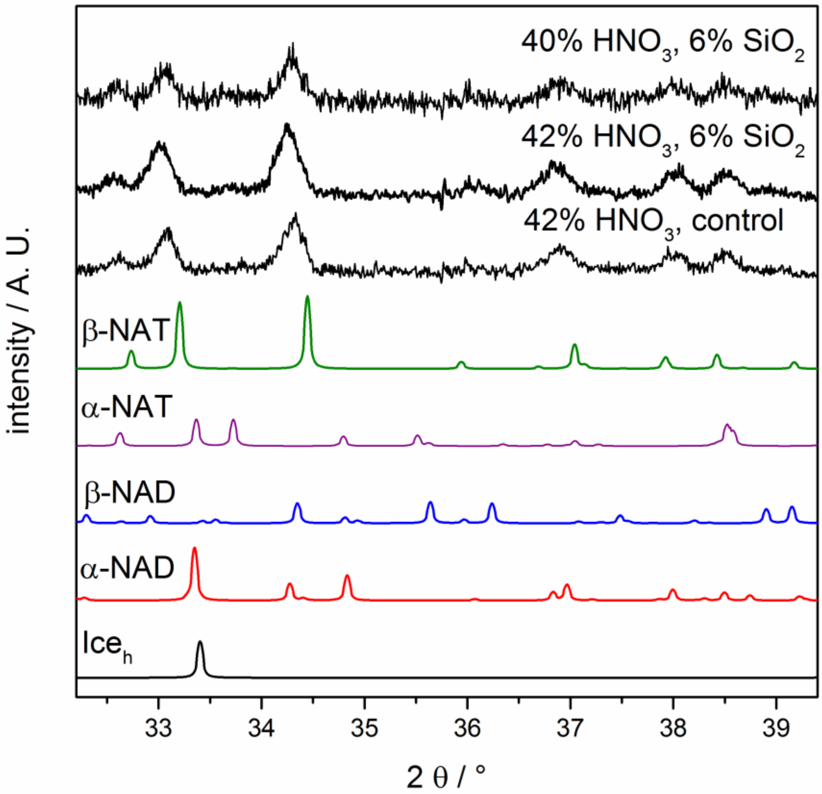

Figure 4.2 X-Ray Diffraction (XRD) patterns measured on warming of arrays of droplets (at 182-183 K) compared to patterns generated from structures of possible consituent phases [*Lebrun et al.*, 2001a; *Lebrun et al.*, 2001b; *Taesler et al.*, 1975; *Weiss et al.*, 2016]. In each experiment the patern resembles that of *β*-NAT with an offset in 2-θ, most likely due to the significant displacement in sample height as the X-Rays pass through the droplets.

As droplets are warmed the crystalline phases melt, with the aqueous phase concentration following the melting curve. The result is that there is a gradual reduction in the crystalline content of droplets, making exact melting points difficult to determine from camera images (See Figure 4.X (c)). The edges of droplets become less clear and a radial gradient in the shade of the material becomes evident for all droplets simultaneously. Taking the mean temperature and standard deviation of the first frame in each experiment where this is clear gives a measure of the start of observable melting of 231.2 ± 0.7 K (in agreement with the H_2O ice / NAT eutectic point at 230.4 K, see Figure 1.11). This suggests that on warming there is some H_2O ice present, and that the melting of NAT becomes observable only when the H_2O ice has melted. The temperature at which crystalline material is no longer visible is within 2 K of melting temperature for each experiment (data not shown). The intensity of *β*-NAT peaks in XRD experiments also reduce, indicating melting, over a similar temperature range. The observation that melting begins around the eutectic point of H_2O ice and NAT suggests that the temperature control is effective, and the variability about that point can be used as an indication of the uncertainty in temperature measurements. For the EF600 temperature stage This measurement and comparison of the calibrated PT100 with the EF600 internal thermocouple has been used to estimate the maximum uncertainty in temperature at ± 2 K. The observation that melting finishes near the temperature where the solid phase is no longer stable shows that the droplet concentration is accurate, i.e. there has not been significant dissolution of either the SiO_2 nuclei or of the substrate slide during the course of the experiment.

4.2.2 Nucleation Kinetics

The trends in observed nucleation with $[HNO_3]$ and available SiO_2 immediately evident in the observed nucleation events have been evaluated kinetically. Since the experimental cooling rates used in this study were limited to a regime much faster than those experienced in the synoptic atmosphere, both the nucleation rate coefficients, J_{het} (which overestimate the importance of time dependence for a non-uniform surface), and the cumulative density of sites active at a given temperature, n_s (which neglects time dependence), have been evaluated for the full data set (see Section 1.3.3 for details).

In determining experimental J_{het} values, observed fraction frozen data were averaged over five events. This gave a mean and 95 % confidence interval of T and S_{NAX} over which J_{het} was calculated from equation (1.7). Up to 2 sporadic points were removed from the beginning or end of each data set until the range defined by the uncertainty (propagated from the 95 % confidence intervals) in the S_{NAD} was not consistent with values less than one and so that no data points were separated by more than 2 K. For each resulting J_{het} value, Equation (1.5) was solved for φ, which was then plotted against S_{NAD} and S_{NAT} as shown in Figure 4.3. There is a clear trend of activity with S_{NAD}, whilst the data with respect to S_{NAT} show no discernible trend. The trend in φ with S_{NAD} has been parameterised by a quadratic equation, fitted to the data weighted by the 95 % confidence intervals. This parameterisation is used to evaluate nucleation in an atmospheric context in Section 4.3. In terms of both S_{NAD} and S_{NAT}, where the substrate is assumed to facilitate heterogeneous nucleation the surface appears to nucleate more efficiently than the particulate SiO_2.

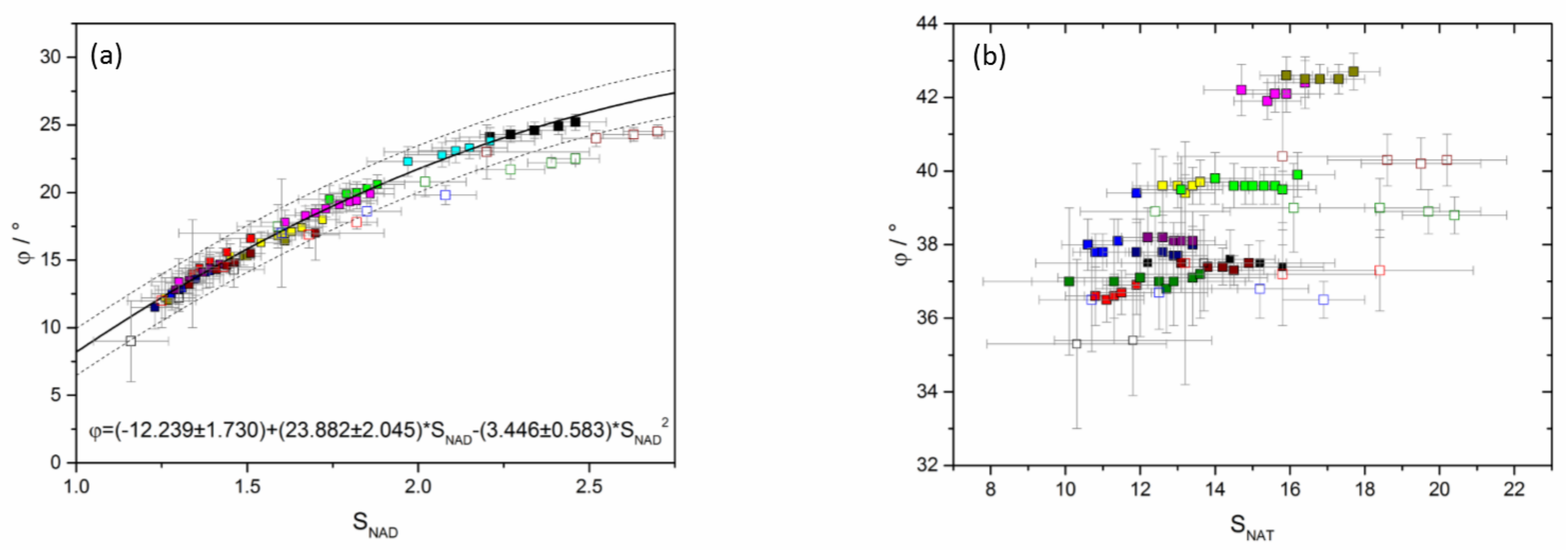

Figure 4.3 Contact angle, *φ, vs*. S_{NAX} for the mean of J_{het} over 5 observed events (see equation 1.5). Error bars are propagated from the 95 % confidence intervals of the mean temperature at which events occurred. Filled points represent experiments where SiO_2 was added, while open points show control experiments (assuming that the aqueous HNO_3 solutions froze by heterogeneous nucleation on the hydrophobic silanised substrates). The trend with S_{NAD} has been parameterised (solid line shows the fit and dashed lines the confidence interval) for evaluation in atmospheric models.

Figure 4.4 shows the relationship between n_s (calculated by equation (1.8)) and S_{NAD} and S_{NAT}. Whilst there is a clear trend in S_{NAD}, the data show significant scatter when plotted against S_{NAT}. Error bars were calculated by simulating a range of concentrations of heterogeneous nuclei and distributing their surface area randomly amongst the droplets. Repeating this process many times for different concentrations, a distribution of concentrations is found which can explain the observed fraction frozen and a 95 % confidence interval on the fraction frozen given by that distribution [*Harrison et al.*, 2016]. At greater $[HNO_3]$, the data fall away from this trend. This may suggest a change in mechanism but is complex since this trend with $[HNO_3]$ was not observed in the parameterisation with φ. An asymptotic fit was performed to the n_s vs. S_{NAD} data at atmospherically relevant $[HNO_3]$, weighted to the 95 % confidence intervals, which can be used to assess the kinetics of this process in the atmosphere.

The observation of trends in both models with S_{NAD} but not S_{NAT} is compelling evidence that the phase which nucleates first is one of the NAD polymorphs. This is consistent with Ostwald's law of stages, which states that the phase which nucleates first will be that with the smallest energetic barrier to nucleation, rather than the most stable phase [*Malkin et al.*, 2012]. A process of transformation from thin films of NAD to NAT has been demonstrated in the past, however temperatures above 200 K were required [*Grothe et al.*, 2008]. The presence of a liquid phase, mediating transfer of material from one crystallite to the other, may increase the rate of this process at lower temperatures. This provides an important reconciliation between the observation that PSCs are composed of *β*-NAT [*Höpfner et al.*, 2006b; *Voigt et al.*, 2000], whilst the rates of nucleation of that phase have been found to be too slow to explain the extent of solid PSCs [*Knopf et al.*, 2002].

Interestingly, the control experiments seem to follow similar trends in nucleation kinetics when the substrate is assumed to be the heterogeneous nucleus. This agreement between nucleation behaviours suggests that these different forms of silica have a similar ability to heterogeneously nucleate NAD. Whilst it has been shown that Junge layer droplets contain solid silica [*Murphy et al.*, 2014], the exact nature of the surfaces of these particles has not been probed. The observation that several kinds of silica nucleate similarly in these experiments suggests that the atmospheric silica may also nucleate similarly, giving confidence that the nucleation kinetics measured in this study can be applied in atmospheric modelling of PSCs.

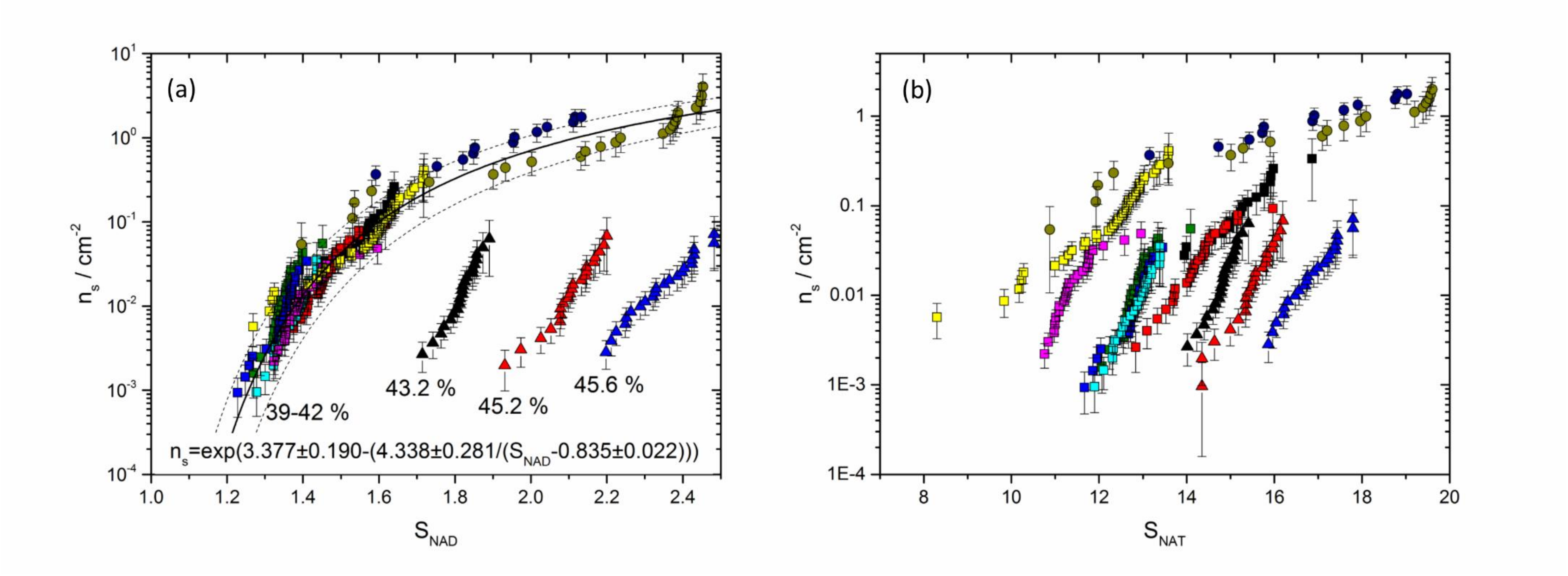

Figure 4.4 n_s vs. (a) S_{NAD} (labelled with *[HNO_3]*) and (b) S_{NAT}. Square and triangular points show experiments with SiO_2 in suspension while circles are used for control experiments, assuming that nucleation occurs on the hydrophobic silanised glass substrate. Triangular points show experiments at *[HNO_3]* greater than those expected to exist in the synoptic polar stratosphere. Error bars were calculated by simulating a range of concentrations of heterogeneous nuclei and distributing their surface area randomly amongst the droplets (see *Harrison et al.* [2016] for details). The clear trend in S_{NAD} at atmospherically relevant *[HNO_3]* (square points only) has been parameterised for evaluation in atmospheric models.

4.3 Implications for Nucleation of Nitric Acid Hydrates on Polar Stratospheric Clouds

A 1-Dimensional atmospheric box model has been developed to investigate the implications of the observed nucleation kinetics in an atmospheric context. The model simulated cooling from 200 to 180 K at a rate of 0.23 K hour^{-1}, consistent with the synoptic polar stratosphere (*i.e.* without perturbation by gravity wave cooling) [*Hoyle et al.*, 2013]. Concentrations of 10 ppb HNO_3, 0.1 ppb H_2SO_4 and 4 ppm H_2O were simulated and the equilibrium concentration of droplets and S_{NAT} and S_{NAD} calculated using the e-AIM model (see Section 1.3.2). Droplet concentration was initially set at 20 cm^{-3}, each containing a heterogeneous surface area of 5×10^{-10} cm^2 (estimated based on recent global simulations of MSPs (pers. comms. J. M. C. Plane, University of Leeds, 2016 after *Bardeen et al.* [2008]). This surface area is calculated from numerical simulations of the growth and transport of meteoric smoke particles, assuming that all particles are spherical and that the meteoric input to the Earth's atmosphere is 44 ton day^{-1}. The true value may be rather larger, since there is significant uncertainty in the meteoric input (a potential factor of 2 increase in mass of MSPs [*Carrillo-Sánchez et al.*, 2015]) and since particles are likely to be fractal agglomerates of smaller spheres (potentially an order of magnitude increase [*Saunders et al.*, 2007; *Saunders and Plane*, 2011]).

Two parameterisations of nucleation kinetics were included separately in the box model. As described in Section 4.2.2, NAD was assumed to nucleate first but rapidly transform to NAT. The number of NAT crystals predicted by each model was then compared to that given by assuming a constant nucleation rate per atmospheric volume, $J_{het,vol} = 8 \times 10^{-6}$ cm^{-3} hour^{-1} for all time steps where $S_{NAT}>1$ [*Grooß et al.*, 2005]. This $J_{het,vol}$ produces 1×10^{-4} cm^{-3} crystals by 191 K, in agreement with atmospheric observations [*Voigt et al.*, 2005]. Processes other than nucleation (*e.g.* growth and sedimentation of crystals) were not included.

In the first model, the φ parameterisation shown in Figure 4.3 was used to calculate a saturation dependent J_{het} from equation (1.5). This was then taken together with the available number of liquid droplets and the heterogeneous surface area in each droplet to calculate a number of nucleation events in each time step. The cumulative number of crystals is shown in Figure 4.5. This model produces significantly more crystals than the atmospheric observations, due to the overestimation of time dependence inherent in assuming a uniform ability to induce heterogeneous nucleation.

In the second model, the n_s parameterisation shown in Figure 4.4 was used to calculate a fraction frozen in each time step of the box model by equation (1.8). This was then combined with the number of liquid droplets remaining from the previous time step to calculate concentrations of crystals, which are plotted in Figure 4.5. The n_s model cannot produce as many crystals as are observed in the atmosphere, even when extrapolated past the S_{NAD} region in which it was constrained by the laboratory data.

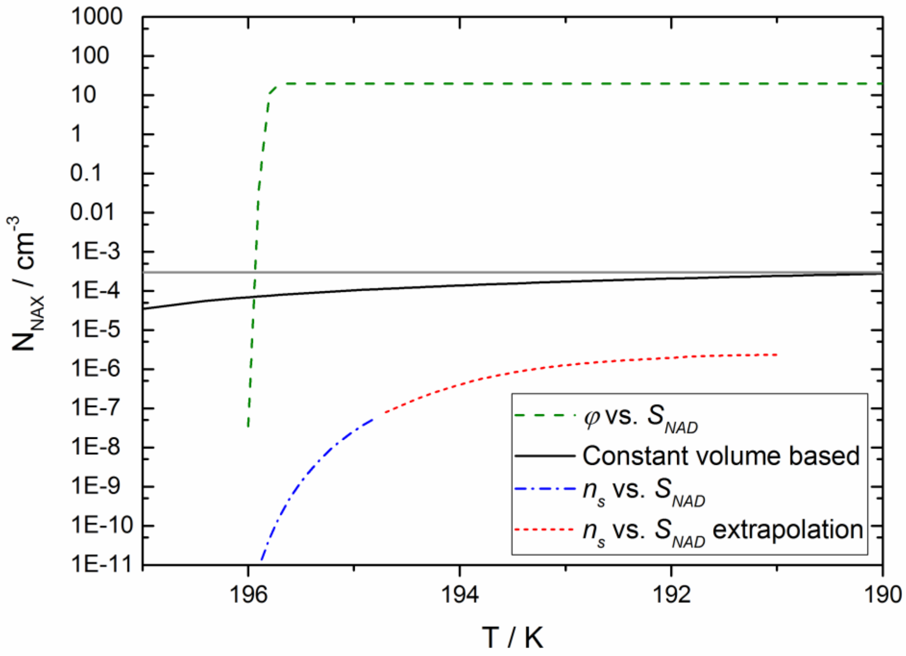

Figure 4.5 Number of crystals formed in a 1D atmospheric box model using various parameterisations. The solid, horizontal, grey line indicates the concentration observed in the atmosphere [*Voigt et al.*, 2005]. The solid black line shows the prediction of a constant, volume based nucleation rate parameterisation. The dashed lines show two models based on parameterisations of the laboratory data presented in this study. Since these two lines bound the observed concentration of crystals, the nucleation of NAD on silica could be an accurate model for crystallisation of PSCs.

The fact that the number of crystals produced by the n_s and φ models bounds the atmospheric observation suggests that nucleation of NAD on silica is a likely candidate for the mechanism by which PSCs crystallise. In addition both parameterisations predict that droplets will supercool by approximately 1.5 K below the temperature at which T_{NAT} is stable. This suggests a basis for recent observations that adding a 1.5 K bias to all aerosol processes in an atmospheric model improved agreement with observations of O_3 [*Brakebusch et al.*, 2013].

The results of the atmospheric modelling demonstrate the importance of quantifying the time dependence of nucleation in this case. The assumption that the surface is uniformly active in the φ parameterisation leads to an overestimation of the importance of time dependence and crystallisation which is far too rapid, whereas neglecting the time dependence entirely through an n_s parameterisation produces too few crystals.

Quantifying the time dependence of nucleation requires consideration of the heterogeneous ability of a surface to facilitate nucleation. One way to do this would be to extend the CNT approach by fitting a distribution of contact angles to the data [*Hoyle et al.*, 2013]. This should in principle be possible with the current data set, and is a key topic for future work.

A second approach is based on the finding that the temperature dependence of the nucleation rate coefficient controls the cooling rate dependence of nucleation [*Herbert et al.*, 2014]. This leads to the Framework for Reconciling Observable Stochastic Time dependence (FROST), which involves modelling the natural logarithm of J_{het} as a linear function of the temperature, where the gradient, λ / K^{-1}, and intercept, ϕ, of the linear dependence is an empirical quantity determined from experimental data:

$$\ln(J_{het}) = -\lambda T + \phi$$

ϕ is related to the probability of a site having a particular activity, whilst λ determines the time dependence. ΔN_{NAX} is then given by equation (1.7), evaluated and summed across a distribution of differently active surface sites. λ and ϕ can be determined from experiments so long as the cooling rate is varied by an order of magnitude. The large temperature range which must be covered (approximately 180-280 K) in order to assess nucleation in this system means that slower cooling rates than the 1 K min^{-1} used here lead to extremely time consuming experiments. Faster cooling rates are also not possible due to the limited cooling power of the apparatus. λ and ϕ can also be determined from constant temperature experiments, which should in principle be possible here, by cooling as rapidly as possible to a temperature where nucleation is expected to occur, then observing nucleation over time at a constant temperature. Such experiments are also a key topic for future work.

4.4 The Effect of H_2SO_4 in the Atmosphere

In the atmosphere, droplets actually follow pathways through a 3 dimensional phase diagram. H_2SO_4 is mentioned in Section 4.2.1 as a possible liquid medium which could facilitate transfer of material between crystallites of different phases. It is worth noting, though, that any effect of H_2SO_4 on the kinetics of nucleation has been neglected here by performing experiments in HNO_3 / H_2O binary solutions.

In the polar vortex Junge layer aerosol, composed of 70 wt % H_2SO_4 in aqueous solution, take up HNO_3 and H_2O from the gas phase as the ambient temperature decreases (see Section 1.3.2, Figure 1.10). Droplets reach saturation with respect to NAT at around 194 K, when the equilibrium concentration of HNO_3 is only 2 wt %, and with respect to NAD at 193 K and 4 wt %, all with equilibrium H_2SO_4 concentrations in excess of 50 wt %. Although the data presented here show significant trends at similar S_{NAX}, changes in the nature of the heterogeneous substrate or interference with kinetic pathways could cause significant changes in the nucleation kinetics when H_2SO_4 is present.

Performing nucleation experiments across the entire 3-Dimensional phase diagram would be prohibitively time consuming and has not been undertaken here. There is, however, clearly a need for future studies to investigate any possible impacts of H_2SO_4 on this system.

4.5 Conclusions

Nucleation kinetics have been observed on a reasonable analogue for MSPs, fumed SiO_2, partially dissolved in PSC aerosol. Nucleation was found to occur at higher temperatures when greater concentrations of heterogeneous material were added, suggesting that it was this heterogeneous material which controlled the nucleation kinetics.

Nucleation was found to follow distinct trends in S_{NAD} but no discernible trend in S_{NAT} when the data were fitted to several theoretical frameworks. Interestingly, the control experiments also fitted to these trends, suggesting that nucleation in these experiments was controlled by the hydrophobic silanised glass slides used as substrates, and that this significantly different material acted similarly to the fumed SiO_2 as a NAX nucleus.

Experiments with XRD detection showed that on cooling and at base temperature, an initially complex and poorly reproducible mixture of phases converts consistently to β-NAT, likely through liquid mediated transfer of material between crystallites of different phases, on timescales much shorter than those for which PSCs persist in the atmosphere. This provides a reconciliation of the observations that PSCs are composed of β-NAT [*Höpfner et al.*, 2006b; *Voigt et al.*, 2000], but that nucleation rates of that phase are too slow to explain the extent of crystalline PSCs [*Knopf et al.*, 2002].

The observed rates of nucleation have been applied in a 1D atmospheric model and the concentration of crystals formed compared to observations of PSCs. It was found that a parameterisation of the material through CNT as having a single, saturation dependent contact angle overestimated the atmospheric concentration of crystals, whilst a parameterisation using the density of sites which were active at a given temperature underestimated the observations.

These results suggest that nucleation of NAD on silica is a possible candidate for the mechanism of PSC crystallisation. Future work should focus on quantifying the time dependence of heterogeneous nucleation on analogues for MSPs, and applying that nucleation in a global model, assuming that nucleation produces NAD which then rapidly converts to NAT.

Chapter 5
Conclusions

Meteoric material has a variety of impacts on the physical and chemical state of atmospheric constituents. Chapter 1 of this thesis sets the scene, laying out the state of the field for some of these processes and identifying problems which were investigated in the rest of the thesis.

Chapter 2 addresses the science question of suitable analogues for Interplanetary Dust Particles (IDPs) and Meteoric Smoke Particles (MSPs) in atmospheric science. Materials were prepared by chemical synthesis from precursors and mechanical grinding of terrestrial minerals and meteorites. The elemental composition, crystallographic, surface and size distribution properties of the products were analysed using a suite of techniques. The materials were then compared to current understanding of IDPs and MSPs. A summary of materials which were successfully identified as analogues for this meteoric material is given in Section 2.3.2.

Chapter 3 addresses reactive uptake of HNO_3 and HO_2 from the gas phase to the surface of MSPs and the possibility that this could alter the atmospheric abundance of these species. Uptake coefficients measured in the laboratory were used to parameterise the impact of MSPs on HNO_3 and HO_2 in WACCM-CARMA. Comparison of model runs with and without reactive uptake was used to characterise changes in the availability of HNO_3 and HO_2. Impacts on the atmospheric abundance were indeed observed. However, the effects were in atmospheric locations where measurements of the gas phase concentration are relatively sparse, so the sensitivity of the atmosphere to reactive uptake to MSPs could not be used to quantify the meteoric input to the Earth.

Chapter 4 addresses measurements of the nucleation kinetics of Nitric Acid hydrate (NAX) phases on SiO_2 particles as an analogue for MSPs under conditions relevant to Polar Stratospheric Clouds (PSCs). Droplets of HNO_3 in aqueous solutions and with suspended SiO_2 were cooled and nucleation events observed. The nucleation was then parameterised using two theoretical models and a box model of equilibrium droplet concentration used to compare the results to observations of crystal concentrations and a parameterisation commonly used in atmospheric models. This was found to be a possible mechanism for nucleation of PSCs. However, a specific recommendation of a kinetic parameterisation for this process in global modelling studies cannot yet be made since the results showed that the time dependence of the process, which has not yet been quantified, may be important.

More detailed conclusions for each chapter are given below.

5.1 Synthesis and Characterisation of Analogues for Interplanetary Dust and Meteor Smoke Particles

Materials useful as analogues for both IDPs and MSPs were identified from the candidates proposed (see Table 2.1).

Ground meteorites and terrestrial minerals were identified as useful analogues for components of IDPs. The differential ablation of meteors is controlled by the melting points of their component phases. Hence the crystallographic and compositional properties of the analogues are key. Individual terrestrial minerals (Olivine, Albite, Labradorite and Anorthite) were shown to be useful as analogues for constituents of IDPs since their elemental composition and crystallographic properties were similar to observations of micrometeorites collected from the South Polar water well (which are the most comprehensive source of information available to researchers regarding the nature of IDPs).

Ground samples of the Allende (CV3) and Murchison (CM2) chondritic meteorites, were found to have elemental composition similar to micrometeorites. The Chergach (H5) chondritic meteorite was found to be similar in composition of some elements to IDPs and to be composed of phases which are known to be present in IDPs. The similarity of Chergach to IDPs suggests that ordinary chondrites can under some circumstances be useful analogues for IDPs. This is significant because ordinary chondrites are much more widely available in meteorite collections than carbonaceous chondrites (CCs). The North West Africa 5515 (NWA, CK4) meteorite was found to represent and outlier in the distribution of IDPs, having extremely high Ca content. This is significant because it demonstrates that CCs are not necessarily good analogues for the majority of IDPs but also because investigating outliers in the distribution can be useful for understanding processes which are rare but can be important (the relatively refractory nature of Ca containing phases such as anorthite means that they are ablated from relatively few IDPs, yet Ca species have been observed in the mesosphere).

Chemical synthesis methods were described which were able to produce amorphous silicates and crystalline iron oxides and oxy-hydroxides which are candidates for the composition of MSP particles. The complex surface morphology of some of these materials means that they have very large available surface area (several hundreds of m^2 g^{-1}), making them ideal for surface science studies.

General recommendations for which analogue to use in certain situations is given in Section 2.3.2.

5.2 Reactive Uptake of HNO_3 and HO_2 in the Middle Atmosphere

Significant uptake of both HNO_3 and HO_2 was observed on the amorphous $MgFeSiO_4$ described in Chapter 2 as useful analogues for MSPs (see Table 3.2).

Comparison of WACCM runs (see Table 3.1) with reactive uptake show that HNO_3 and HO_2 are likely perturbed compared to a control in the polar vortex by reactive uptake onto MSPs. Whilst the effect on HO_2 is confined to the polar vortex, with other loss processes dominating elsewhere, the effect on HNO_3 was observed over the entire winter hemisphere. This effect is overestimated below 2 hPa, because the model did not include a treatment of the interaction of MSPs with H_2SO_4, which will coat and deactivate the MSP surfaces. Increasing the uptake coefficient to account for the effect on the uptake of lower atmospheric temperatures shows increased reductions in atmospheric species. This increase with the uptake coefficient is more sensitive to the uptake coefficient at lower uptake coefficients than when the value approaches unity.

Uptake processes of these few species have wide ranging effects on a variety of chemistry in the middle atmosphere, including feedbacks on each other. Removal of HNO_3 in the winter leads to losses of NO_x species in the summer (since HNO_3 is readily photolysed to NO_2 and OH). Removal of reactive nitrogen is known to have significant impacts on the ozone hole, since growth and sedimentation of PSCs has a similar affect, known as denitrification. Removal of NO_x leads to increased HO_2 since HO_2 is removed by reaction with NO_2 and reduced to OH by NO. HNO_3 is also reduced when HO_2 is removed since HO_2 is in equilibrium with OH (*via* reaction with O_3) and OH reacts with NO_2 to produce HNO_3.

5.3 Nucleation of Nitric Acid Hydrates Under Conditions Relevant to Polar Stratospheric Clouds

Nucleation of NAX phases was found to occur at higher temperatures when greater concentrations of heterogeneous SiO_2 were added, suggesting that this heterogeneous material can control the kinetics of nucleation.

Nucleation was found to follow distinct trends in the saturation ratio with respect to Nitric Acid Dihydrate, S_{NAD}, but no discernible trend in saturation ratio with respect to Nitric Acid Trihydrate, S_{NAT}, when the data were fitted to several theoretical frameworks. The control experiments also fitted to these trends, suggesting that nucleation in these experiments was controlled by the hydrophobic silanised glass slides used as substrates, and that this significantly different material acted similarly to the fumed SiO_2 as a NAX nucleus.

Experiments with XRD detection showed that on cooling and at base temperature, an initially complex and poorly reproducible mixture of phases converts consistently to the β- polymorph of NAT. This likely proceeds through liquid mediated transfer of material between crystallites of different phases, on timescales much shorter than those for which PSCs persist in the atmosphere. This provides a reconciliation of the observations that PSCs are composed of β-NAT, but that nucleation rates of that phase are too slow to explain the extent of crystalline PSCs.

The observed rates of nucleation have been applied in a 1D atmospheric model and the concentration of crystals formed compared to observations of PSCs. It was found that a parameterisation of the material through CNT as having a single, saturation dependent contact angle overestimated the atmospheric concentration of crystals, whilst a parameterisation using the density of sites which were active at a given temperature underestimated the observations.

These results suggest that nucleation of NAD on silica is a possible candidate for the mechanism of PSC crystallisation since it was shown to control the nucleation and to be capable of producing sufficient concentrations of crystals in an atmospheric setting.

5.4 Synthesis of Results

As meteoric material is processed in and transported through the Earth's atmosphere it also impacts a range of aspects of the environment. These include effects on the gas phase abundances of species and the physical state of polar stratospheric clouds. Kinetics of each of these processes were quantified here using appropriate analogues for the meteoric material in question and their atmospheric significance investigated with a view to constraining the amount of meteoric material which reaches Earth each day. The results suggest that whilst these processes do represent sensitivities of the atmosphere to the availability of meteoric material, further work is required before these can be used as a means to quantitatively constrain the meteoric input.

Chapter 6
Future Work

As discussed in Chapter 5, the work described in this thesis represents significant progress in quantifying some of the impacts of meteoric material on Earth's atmosphere. Significant open questions remain regarding some of these processes. These include controlled synthesis of analogues for Interplanetary Dust Particles (IDPs) made from mixtures of single minerals, laboratory measurements of the temperature dependence of uptake coefficients, quantification of the time dependence of heterogeneous nucleation of Nitric Acid hydrate (NAX) phases by SiO_2 as an analogue for Meteoric Smoke Particles (MSPs) and more sophisticated modelling of atmospheric processes.

6.1 Future Laboratory Studies

The analogues for IDPs discussed in Chapter 2 could be further developed by combining mixtures of single minerals to create aggregate particles. This would facilitate production of large quantities of IDP analogues from readily available precursors. Some form of fixative would be required to hold the constituent particles together and this would have to be considered in any application of these analogues.

Laboratory studies able to measure the temperature dependence of the uptake coefficient would be invaluable in informing atmospheric modelling. Designing an instrument able to make these measurements is extremely difficult. The importance of diffusion and wall losses in the flow tube technique reported in Chapter 3 would be compounded by cooling the system. A Knudsen cell could be cooled, though maintaining vacuum pressure in the Knudsen regime could be an issue. A low pressure dual flowtube system reported by *Frankland et al.* [2016] was able to measure acetylene uptake as a function of temperature with implications for the atmosphere of Titan. This alternative method, with appropriate detection of HNO_3 by mass spectrometry and HO_2 by FAGE, should be applied to measuring uptake coefficients in the atmospherically relevant temperature regime, potentially from room temperature to dry ice conditions (180 K, relevant to the upper stratosphere / lower mesosphere where uptake has been shown to be important).

As discussed in Chapter 4, heterogeneous nucleation of NAX phases on SiO_2 has the potential to produce the concentration of NAX crystals observed in the atmosphere. In order to correctly predict the atmospheric crystal concentration based on the laboratory results, however, the time dependence of the nucleation must be quantified. Experiments either observing the nucleation rates at fixed temperature or observing with a varied cooling rate could allow this quantification. Varied cooling rates need to span at least a factor of 10. Experiments should focus to begin with on a single set of HNO_3 and SiO_2 concentrations (40 % HNO_3 and 6 % SiO_2 would place these results well in relation to the current data set) but then ideally confirm that the results hold for a broader range of conditions. A further important development would be to examine the effect of H_2SO_4 in solution. The nucleation rate is dependent on diffusion to form the initial critical cluster of molecules with the structure of the solid, so the viscosity change implied by the presence of sulfuric acid could affect the observed nucleation. This should be approached in two ways; small amounts (<5 %) H_2SO_4 can be added to the solutions used here and a fully atmospheric concentration (5-20 % HNO_3, 50-25 % H_2SO_4) can be employed (S_{NAD} is similar under these conditions to that measured here). Examining the entire phase diagram is clearly not time efficient, but it may be possible to modify the kinetics observed here from a relatively small number of experimental observations.

It would also be extremely valuable to measure the uptake coefficient for H_2SO_4 on meteoric smoke. This could be achieved using the dual flow tube system developed by *Frankland et al.* [2016] which at dry ice temperature (~180 K) and low pressure (~10 torr) would be a good approximation of the relevant atmospheric conditions. An inherent difficulty in these experiments is the low volatility of H_2SO_4. Detection of low gas phase concentrations of this material can be facilitated by a Chemical Ionisation Mass Spectrometry (CIMS) instrument, which would need to be constructed.

6.2 Future Atmospheric Modelling Studies

Following these laboratory measurements there is also scope for significant further modelling and comparison to measurements. As shown in Chapter 3, there is significant chemical interplay between HNO_3 and HO_2 so that modelling studies looking at both uptake processes in tandem are timely. Comparison of the output of these studies to atmospheric observations could help to constrain the atmospheric uptake coefficient and ultimately the availability of MSPs in the atmosphere. In addition these studies should include a treatment of deactivation of interaction of MSPs by H_2SO_4 in the lower stratosphere. This has been achieved by *Neely et al.* [2011] by treating three separate arrays of MSPs, sulfate aerosol and ‘cores’ (MSPs in sulfate) in a similar manner to that used here. Treatment of the deactivation of MSPs by sulfate aerosol could then be achieved simply by treating uptake to the MSP field but not the cores.

Preferably informed by low temperature measurements of the uptake coefficients, model runs should be conducted which include a description of all of these uptake processes and the resulting change in a wide range of atmospheric species should be investigated. For the species discussed here (particularly HO_2) there are not sufficient atmospheric measurements to constrain the impact of uptake. However, many more measurements exist of species which will be affected indirectly, such as O_3, which is very widely measured and involved in the chemistry of both HNO_3 and HO_2 (see Figure 1.6).

Full treatment of these processes would then allow a model to incorporate partial dissolution of MSPs in stratospheric droplets, nucleation of NAX in PSCs on the SiO_2 remaining and resulting transport of MSPs into the troposphere. This would also give a firm mechanistic and kinetic understanding of the impact of heterogeneous chemistry in PSCs, which has been shown to be critical for modelling of the ozone hole. The outcome of these studies should be compared to the observations extinction due to MSPs, refractory aerosols in the stratosphere and to measurements of meteoric material in ice cores, in order to constrain the meteoric input to the Earth.

List of References

Bardeen, C. G., O. B. Toon, E. J. Jensen, D. R. Marsh, and V. L. Harvey (2008), Numerical simulations of the three-dimensional distribution of meteoric dust in the mesosphere and upper stratosphere, *J. Geophys. Res.: Atmos.*, *113*(D17), D17202

Biermann, U. M., T. Presper, T. Koop, J. Mößinger, P. J. Crutzen, and T. Peter (1996), The unsuitability of meteoritic and other nuclei for polar stratospheric cloud freezing, *Geophys. Res. Lett.*, *23*(13), 1693-1696

Bigg, E. K. (2012), Sources of insoluble inclusions in stratospheric sulfate particles, *Meteorit. Planet. Sci.*, *47*(5), 799-805

Blanchard, M. B., D. E. Brownlee, T. E. Bunch, P. W. Hodge, and F. T. Kyte (1980), Meteoroid ablation spheres from deep-sea sediments, *Earth Plan. Sci. Lett.*, *46*(2), 178-190

Bogdan, A., M. J. Molina, M. Kulmala, A. R. MacKenzie, and A. Laaksonen (2003), Study of finely divided aqueous systems as an aid to understanding the formation mechanism of polar stratospheric clouds: Case of HNO_3/H_2O and H_2SO_4/H_2O systems, *J. Geophys. Res.: Atmos.*, *108*(D10), 4302

Bowen, N. L. (1913), The melting phenomena of the plagioclase feldspars, *Amer. J. Sci.*(210), 577-599

Brakebusch, M., C. E. Randall, D. E. Kinnison, S. Tilmes, M. L. Santee, and G. L. Manney (2013), Evaluation of Whole Atmosphere Community Climate Model simulations of ozone during Arctic winter 2004–2005, *J. Geophy. Res.: Atmos.*, *118*(6), 2673-2688

Brasseur, G. P., and S. Solomon (1998), *Aeronomy of the middle atmosphere: chemistry and physics of the stratosphere and mesosphere*, D. Reidel publishing company, Dordrecht, holland

Burchell, M. J., J. Mann, J. A. Creighton, A. T. Kearsley, G. Graham, and I. A. Franchi (2006), Identification of minerals and meteoritic materials via Raman techniques after capture in hypervelocity impacts on aerogel, *Meteorit. Planet. Sci.*, *41*(2), 217-232

Burgess, R., I. P. Wright, and C. T. Pillinger (1991), Determination of sulphur-bearing components in C1 and C2 carbonaceous chondrites by stepped combustion, *Meteoritics*, *26*(1), 55-64

Campbell, P., and T. Deshler (2014), Condensation nuclei measurements in the midlatitude (1982–2012) and Antarctic (1986–2010) stratosphere between 20 and 35 km, *J. Geophys. Res.: Atmos.*, *119*(1), 137-152

Carrillo-Sánchez, J. D., J. M. C. Plane, W. Feng, D. Nesvorný, and D. Janches (2015), On the size and velocity distribution of cosmic dust particles entering the atmosphere, *Geophys. Res. Lett.*, *42*(15), 6518-6525

Carslaw, K. S., J. A. Kettleborough, M. J. Northway, S. Davies, R.-S. Gao, D. W. Fahey, D. G. Baumgardner, M. P. Chipperfield, and A. Kleinböhl (2002), A vortex-scale simulation of the growth and sedimentation of large nitric acid hydrate particles, *J. Geophys. Res.: Atmos.*, *107*(D20)

Carslaw, K. S., T. Peter, and S. L. Clegg (1997), Modeling the composition of liquid stratospheric aerosols, *Rev. Geophys.*, *35*(2), 125-154

Choël, M., K. Deboudt, J. Osán, P. Flament, and R. Van Grieken (2005), Quantitative determination of low-Z elements in single atmospheric particles on boron substrates by automated scanning electron microscopy−energy-dispersive X-ray spectrometry, *Analyt. Chem.*, *77*(17), 5686-5692

Chu, B. (2008), Dynamic light scattering, in *Soft matter characterization*, edited by R. Borsali and R. Pecora, pp. 335-372, Springer Netherlands, Dordrecht

Clarke, R., E. Jarosevich, B. Mason, J. Nelen, M. Gomez, and J. R. Hyde (1971), The Allende, Mexico, Meteoroite Shower*Rep.*, Smithsonian Institution Press, Washington.

Clegg, S. L., P. Brimblecombe, and A. S. Wexler (1998), Thermodynamic model of the system $H^+-NH_4^+-SO_4^{2-}-NO_3^--H_2O$ at tropospheric temperatures, *J. Phys. Chem. A*, *102*(12), 2137-2154

Consolmagno, G. J., D. T. Britt, and R. J. Macke (2008), The significance of meteorite density and porosity, *Chem. der Erde - Geochem.*, *68*(1), 1-29

Court, R. W., and M. A. Sephton (2011), The contribution of sulphur dioxide from ablating micrometeorites to the atmospheres of Earth and Mars, *Geochim. Cosmochim. Acta*, *75*(7), 1704-1717

Curtius, J., et al. (2005), Observations of meteoric material and implications for aerosol nucleation in the winter Arctic lower stratosphere derived from in situ particle measurements, *Atmos. Chem. Phys.*, *5*(11), 3053-3069

Dhomse, S. S., R. W. Saunders, W. Tian, M. P. Chipperfield, and J. M. C. Plane (2013), Plutonium-238 observations as a test of modeled transport and surface deposition of meteoric smoke particles, *Geophys. Res. Lett.*, *40*(16), 4454-4458

Ebert, M., R. Weigel, K. Kandler, G. Günther, S. Molleker, J. U. Grooß, B. Vogel, S. Weinbruch, and S. Borrmann (2016), Chemical analysis of refractory stratospheric aerosol particles collected within the arctic vortex and inside polar stratospheric clouds, *Atmos. Chem. Phys.*, *16*(13), 8405-8421

Engel, I., B. P. Luo, M. C. Pitts, L. R. Poole, C. R. Hoyle, J. U. Grooß, A. Dörnbrack, and T. Peter (2013), Heterogeneous formation of polar stratospheric clouds – Part 2: Nucleation of ice on synoptic scales, *Atmos. Chem. Phys.*, *13*(21), 10769-10785

Feng, W., D. R. Marsh, M. P. Chipperfield, D. Janches, J. Höffner, F. Yi, and J. M. C. Plane (2013), A global atmospheric model of meteoric iron, *J. Geophys. Res.: Atmos.*, *118*(16), 9456-9474

Frankland, V. L., A. D. James, J. D. Carillo-Sánchez, T. P. Mangan, K. Willacy, A. R. Poppe, and J. M. C. Plane (2016), Uptake of acetylene on cosmic dust and production of benzene in Titan's atmosphere, *Icarus*, *278*, 88-99

Frankland, V. L., A. D. James, W. Feng, and J. M. C. Plane (2015), The uptake of HNO_3 on meteoric smoke analogues, *J. Atmos. Sol.-Terr. Phys.*, *127*, 150-160

Frisch, M. J., G. W. Trucks, H. B. Schlegel, G. E. Scuseria, M. A. Robb, J. R. Cheeseman, G. Scalmani, V. Barone, B. Mennucci, and G. A. Petersson (2009), Gaussian 09, revision A. 1, *Gaussian Inc., Wallingford, CT*

Fuchs, L. H., K. J. Jensen, and E. J. Olsen (1973), *Mineralogy, mineral-chemistry, and composition of the Murchison (C2) meteorite*, Smithsonian Institution Press

Funke, B., et al. (2011), Composition changes after the "Halloween" solar proton event: the High Energy Particle Precipitation in the Atmosphere (HEPPA) model versus MIPAS data intercomparison study, *Atmos. Chem. Phys.*, *11*(17), 9089-9139

Gómez Martín, J. C., D. L. Bones, J. D. Carrillo-Sánchez, A. D. James, J. M. Trigo-Rodríguez, B. Fegley Jr., and J. M. C. Plane (2016 - Unpublished results), Novel experimental simulations of the atmospheric injection of meteoric metals

Greshake, A., W. KlÖCk, P. Arndt, M. Maetz, G. J. Flynn, S. Bajt, and A. Bischoff (1998), Heating experiments simulating atmospheric entry heating of micrometeorites: Clues to their parent body sources, *Meteorit. Planet. Sci.*, *33*(2), 267-290

Grooß, J. U., G. Günther, R. Müller, P. Konopka, S. Bausch, H. Schlager, C. Voigt, C. M. Volk, and G. C. Toon (2005), Simulation of denitrification and ozone loss for the Arctic winter 2002/2003, *Atmos. Chem. Phys.*, *5*(6), 1437-1448

Grothe, H., H. Tizek, and I. K. Ortega (2008), Metastable nitric acid hydrates-possible constituents of polar stratospheric clouds?, *Faraday Disc.*, *137*(0), 223-234

Gualtieri, A. F., and P. Venturelli (1999), In situ study of the goethite-hematite phase transformation by real time synchrotron powder diffraction, in *Amer. Mineral.*, edited, p. 895

Hanisch, F., and J. N. Crowley (2001), Heterogeneous reactivity of gaseous nitric acid on Al_2O_3, $CaCO_3$, and atmospheric dust samples: A Knudsen cell study, *Journal Phys. Chem. A*, *105*(13), 3096-3106

Harrison, A. D., T. F. Whale, M. A. Carpenter, M. A. Holden, L. Neve, D. O'Sullivan, J. Vergara Temprado, and B. J. Murray (2016), Not all feldspars are equal: a survey of ice nucleating properties across the feldspar group of minerals, *Atmos. Chem. Phys.*, *16*(17), 10927-10940

Hayward, D. O., D. A. King, and F. C. Tompkins (1967), Variation of sticking probabilities with temperature and coverage, and desorption spectra for nitrogen on tungsten films, *Proc. Royal Soc. London. Series A. Math. Phys. Sci.*, *297*(1450), 321-335

Hedin, J., et al. (2014), The MAGIC meteoric smoke particle sampler, *J. Atmos. Sol.-Terr. Phys.*, *118, Part B*, 127-144

Herbert, R. J., B. J. Murray, T. F. Whale, S. J. Dobbie, and J. D. Atkinson (2014), Representing time-dependent freezing behaviour in immersion mode ice nucleation, *Atmos. Chem. Phys.*, *14*(16), 8501-8520

Hervig, M. E., L. E. Deaver, C. G. Bardeen, J. M. Russell Iii, S. M. Bailey, and L. L. Gordley (2012), The content and composition of meteoric smoke in mesospheric ice particles from SOFIE observations, *J. Atmos. Sol.-Terr. Phys.*, *84–85*, 1-6

Hervig, M. E., L. L. Gordley, L. E. Deaver, D. E. Siskind, M. H. Stevens, J. M. Russell, S. M. Bailey, L. Megner, and C. G. Bardeen (2009), First satellite observations of meteoric smoke in the middle atmosphere, *Geophys. Res. Lett.*, *36*(18), L18805

Hilchenbach, M., et al. (2016), Comet 67P/Churyumov–Gerasimenko: Close-up on Dust Particle Fragments, *Astrophys. J. Lett.*, *816*(2), L32

Hiranuma, N., N. Hoffmann, A. Kiselev, A. Dreyer, K. Zhang, G. Kulkarni, T. Koop, and O. Möhler (2014), Influence of surface morphology on the immersion mode ice nucleation efficiency of hematite particles, *Atmos. Chem. Phys.*, *14*(5), 2315-2324

Höpfner, M., et al. (2006a), MIPAS detects Antarctic stratospheric belt of NAT PSCs caused by mountain waves, *Atmos. Chem. Phys.*, *6*(5), 1221-1230

Höpfner, M., et al. (2006b), Spectroscopic evidence for NAT, STS, and ice in MIPAS infrared limb emission measurements of polar stratospheric clouds, *Atmos. Chem. Phys.*, *6*(5), 1201-1219

Hörz, F., M. E. Zolensky, R. P. Bernhard, T. H. See, and J. L. Warren (2000), Impact features and projectile residues in aerogel exposed on Mir, *Icarus*, *147*(2), 559-579

Hoyle, C. R., I. Engel, B. P. Luo, M. C. Pitts, L. R. Poole, J. U. Grooß, and T. Peter (2013), Heterogeneous formation of polar stratospheric clouds – Part 1: Nucleation of nitric acid trihydrate (NAT), *Atmos. Chem. Phys.*, *13*(18), 9577-9595

Hutchison, R. (2004), *Meteorites: A petrologic, chemical and isotopic synthesis*, Cambridge University Press, Cambridge, UK

James, A. D., D. R. Moon, W. Feng, P. S. J. Lakey, V. L. F. Frankland, D. E. Heard, and J. M. C. Plane (2016), The uptake of HO_2 on meteoric smoke analogues, *J. Geophy. Res.: Atmos. - submitted draft*

Janches, D., L. P. Dyrud, S. L. Broadley, and J. M. C. Plane (2009), First observation of micrometeoroid differential ablation in the atmosphere, *Geophys. Res. Lett.*, *36*(6), L06101

Jessberger, E. K., T. Stephan, D. Rost, P. Arndt, M. Maetz, F. J. Stadermann, D. E. Brownlee, J. P. Bradley, and G. Kurat (2001), Properties of interplanetary dust: information from collected samples, in *Interplanetary Dust*, edited by E. Grün, B. Å. S. Gustafson, S. Dermott and H. Fechtig, pp. 253-294, Springer Berlin Heidelberg, Berlin, Heidelberg

Jucks, K. W., D. G. Johnson, K. V. Chance, W. A. Traub, and R. J. Salawitch (1999), Nitric acid in the middle stratosphere as a function of altitude and aerosol loading, *J. Geophys. Res.: Atmos.*, *104*(D21), 26715-26723

Junge, C. E., C. W. Chagnon, and J. E. Manson (1961), Stratospheric Aerosols, *J. Met.*, *18*(1), 81-108

Kearsley, A. T., M. J. Burchell, M. C. Price, G. A. Graham, P. J. Wozniakiewicz, M. J. Cole, N. J. Foster, and N. Teslich (2009), Interpretation of Wild 2 dust fine structure: Comparison of Stardust aluminum foil craters to the three-dimensional shape of experimental impacts by artificial aggregate particles and meteorite powders, *Meteorit. Planet. Sci.*, *44*(10), 1489-1509

Keyser, L. F., S. B. Moore, and M. T. Leu (1991), Surface reaction and pore diffusion in flow-tube reactors, *J. Phys. Chem.*, *95*(14), 5496-5502

Knopf, D. A., T. Koop, B. P. Luo, U. G. Weers, and T. Peter (2002), Homogeneous nucleation of NAD and NAT in liquid stratospheric aerosols: insufficient to explain denitrification, *Atmos. Chem. Phys.*, *2*(3), 207-214

Kohout, T., et al. (2014), Density, porosity and magnetic susceptibility of the Košice meteorite shower and homogeneity of its parent meteoroid, *Planet. Space Sci.*, *93–94*, 96-100

Koop, T., U. M. Biermann, W. Raber, B. P. Luo, P. J. Crutzen, and T. Peter (1995), Do stratospheric aerosol droplets freeze above the ice frost point?, *Geophys. Res. Lett.*, *22*(8), 917-920

Kremser, S., et al. (2016), Stratospheric aerosol—Observations, processes, and impact on climate, *Rev. Geophys.*, *54*(2), 278-335

Kvissel, O. K., Y. J. Orsolini, F. Stordal, I. S. A. Isaksen, and M. L. Santee (2012), Formation of stratospheric nitric acid by a hydrated ion cluster reaction: Implications for the effect of energetic particle precipitation on the middle atmosphere, *J. Geophys. Res.: Atmos.*, *117*(D16), D16301

Lakey, P. S. J., I. J. George, L. K. Whalley, M. T. Baeza-Romero, and D. E. Heard (2015), Measurements of the HO_2 uuptake coefficients onto single component organic aerosols, *Envi. Sci. Tech.*, *49*(8), 4878-4885

Larsen, N., et al. (2004), Formation of solid particles in synoptic-scale Arctic PSCs in early winter 2002/2003, *Atmos. Chem. Phys.*, *4*(7), 2001-2013

Lebrun, N., F. Mahe, J. Lamiot, M. Foulon, and J. C. Petit (2001a), A new crystalline phase of nitric acid dihydrate, *Acta Cryst. Sect. C*, *57*(10), 1129-1131

Lebrun, N., F. Mahe, J. Lamiot, M. Foulon, J. C. Petit, and D. Prevost (2001b), Kinetic behaviour investigations and crystal structure of nitric acid dihydrate, *Acta Cryst. Sect. B*, *57*(1), 27-35

Lisse, C. M., et al. (2006), Spitzer spectral observations of the deep impact ejecta, *Science*, *313*(5787), 635-640

Liu, P. S. K., and T. Deshler (2003), Causes of concentration differences between a scanning mobility particle sizer and a condensation particle counter, *Aerosol Sci. Tech.*, *37*(11), 916-923

Livesey, N. J., W. G. Read, L. Froidevaux, A. Lambert, G. L. Manney, H. C. Pumphrey, M. L. Santee, M. J. Schwartz, S. Wang, and R. E. Cofield (2011), Version 3.3 Level 2 data quality and description document, in *JPL D-33509*, edited, JPL, Pasadena, CA, US

Love, S. G., and D. E. Brownlee (1993), A direct measurement of the terrestrial mass accretion rate of cosmic dust, *Science*, *262*(5133), 550-553

Luo, B. P., C. Voigt, S. Fueglistaler, and T. Peter (2003), Extreme NAT supersaturations in mountain wave ice PSCs: A clue to NAT formation, *J. Geophys. Res.: Atmos.*, *108*(D15)

Malkin, T. L., B. J. Murray, A. V. Brukhno, J. Anwar, and C. G. Salzmann (2012), Structure of ice crystallized from supercooled water, *Proc. Nat. Ac. Sci.*, *109*(4), 1041-1045

Mann, G. W., K. S. Carslaw, M. P. Chipperfield, S. Davies, and S. D. Eckermann (2005), Large nitric acid trihydrate particles and denitrification caused by mountain waves in the Arctic stratosphere, *J. Geophys. Res.: Atmos.*, *110*(D8)

Mann, S., S. L. Burkett, S. A. Davis, C. E. Fowler, N. H. Mendelson, S. D. Sims, D. Walsh, and N. T. Whilton (1997), Sol−Gel synthesis of organized matter, *Chem. Mater.*, *9*(11), 2300-2310

Matthews, P. S. J., M. T. Baeza-Romero, L. K. Whalley, and D. E. Heard (2014), Uptake of HO_2 radicals onto Arizona test dust particles using an aerosol flow tube, *Atmos. Chem. Phys.*, *14*(14), 7397-7408

Maurette, M., C. Jehanno, E. Robin, and C. Hammer (1987), Characteristics and mass distribution of extraterrestrial dust from the Greenland ice cap, *Nature*, *328*, 699 - 702

McCusker, L. B., R. B. Von Dreele, D. E. Cox, D. Louer, and P. Scardi (1999), Rietveld refinement guidelines, *J. Appl. Cryst.*, *32*(1), 36-50

Meilinger, S. K., T. Koop, B. P. Luo, T. Huthwelker, K. S. Carslaw, U. Krieger, P. J. Crutzen, and T. Peter (1995), Size-dependent stratospheric droplet composition in Lee wave temperature fluctuations and their potential role in PSC freezing, *Geophys. Res. Lett.*, *22*(22), 3031-3034

Millán, L., S. Wang, N. Livesey, D. Kinnison, H. Sagawa, and Y. Kasai (2015), Stratospheric and mesospheric HO_2 observations from the Aura Microwave Limb Sounder, *Atmos. Chem. Phys.*, *15*(5), 2889-2902

Montgomery, J. A., M. J. Frisch, J. W. Ochterski, and G. A. Petersson (2000), A complete basis set model chemistry. VII. Use of the minimum population localization method, *J. Chem. Phys.*, *112*(15), 6532-6542

Murphy, D. M., K. D. Froyd, J. P. Schwarz, and J. C. Wilson (2014), Observations of the chemical composition of stratospheric aerosol particles, *Quart. J. Royal Met. Soc.*, *140*(681), 1269-1278

Murray, B. J., and A. K. Bertram (2008), Inhibition of solute crystallisation in aqueous H^+-NH^{4+}-SO_4^{2-}-H_2O droplets, *Phys. Chem. Chem. Phys.*, *10*(22), 3287-3301

Murray, B. J., D. O'Sullivan, J. D. Atkinson, and M. E. Webb (2012), Ice nucleation by particles immersed in supercooled cloud droplets, *Chem. Soc. Rev.*, *41*(19), 6519-6554

Nachbar, M., D. Duft, T. P. Mangan, J. C. Gomez Martin, J. M. C. Plane, and T. Leisner (2016), Laboratory measurements of heterogeneous CO_2 ice nucleation on nanoparticles under conditions relevant to the Martian mesosphere, *J. Geophys. Res.: Plan.*(121), e004978

Neely, R. R., J. M. English, O. B. Toon, S. Solomon, M. Mills, and J. P. Thayer (2011), Implications of extinction due to meteoritic smoke in the upper stratosphere, *Geophys. Res. Lett.*, *38*(24), L24808

Nesvorný, D., D. Janches, D. Vokrouhlický, D. Pokorný, W. F. Bottke, and P. Jenniskens (2011), Dynamical model for the zodiacal cloud and sporadic meteors, *Astrophys. J.*, *743*(2), 129

Nesvorný, D., P. Jenniskens, H. F. Levison, W. F. Bottke, D. Vokrouhlický, and M. Gounelle (2010), Cometary origin of the zodiacal cloud and carbonaceous micrometeorites. Implications for hot debris disks, *Astrophys. J.*, *713*(2), 816

Opeil Sj, C. P., G. J. Consolmagno Sj, D. J. Safarik, and D. T. Britt (2012), Stony meteorite thermal properties and their relationship with meteorite chemical and physical states, *Meteorit. & Planet. Sci.*, *47*(3), 319-329

Ozaki, M., S. Kratohvil, and E. Matijević (1984), Formation of monodispersed spindle-type hematite particles, *J. Coll. Interf. Sci.*, *102*(1), 146-151

Peter, T., and J. U. Grooß (2012), Chapter 4: Polar stratospheric clouds and sulfate aerosol particles: Microphysics, denitrification and heterogeneous chemistry, in *Stratospheric Ozone Depletion and Climate Change*, edited, pp. 108-144, The Royal Society of Chemistry

Pickett, H. M., et al. (2008), Validation of Aura Microwave Limb Sounder OH and HO_2 measurements, *J. Geophys. Res.: Atmos.*, *113*(D16), D16S30

Plane, J. M. C. (2012), Cosmic dust in the earth's atmosphere, *Chem. Soc. Rev.*, *41*(19), 6507-6518

Plane, J. M. C., W. Feng, and E. C. M. Dawkins (2015), The mesosphere and metals: chemistry and changes, *Chem. Rev.*, *115*(10), 4497-4541

Plane, J. M. C., J. C. Gómez-Martín, W. Feng, and D. Janches (2016), Silicon chemistry in the mesosphere and lower thermosphere, *J. Geophys. Res.: Atmos.*, *121*(7), 3718-3728

Plane, J. M. C., et al. (2014), A combined rocket-borne and ground-based study of the sodium layer and charged dust in the upper mesosphere, *J. Atmos. and Sol.Terr. Phys.*, *118, Part B*, 151-160

Prather, M. J., and J. M. Rodriguez (1988), Antarctic ozone: Meteoric control of HNO_3, *Geophys. Ress Letts*, *15*(1), 1-4

Rapp, M., J. M. C. Plane, B. Strelnikov, G. Stober, S. Ernst, J. Hedin, M. Friedrich, and U. P. Hoppe (2012), In situ observations of meteor smoke particles (MSP) during the Geminids 2010: constraints on MSP size, work function and composition, *Ann. Geophys.*, *30*(12), 1661-1673

Rietmeijer, F. J. M. (2000), Interrelationships among meteoric metals, meteors, interplanetary dust, micrometeorites, and meteorites, *Meteorit. Planet. Sci.*, *35*(5), 1025-1041

Rietmeijer, F. J. M. (2015), The smallest comet 81P/Wild 2 dust dances around the CI composition, *Meteorit. Plan. Sci.*, *50*(10), 1767-1789

Robertson, S., S. Dickson, M. Horányi, Z. Sternovsky, M. Friedrich, D. Janches, L. Megner, and B. Williams (2014), Detection of meteoric smoke particles in the mesosphere by a rocket-borne mass spectrometer, *J. Atmos. Sol.-Terr. Phys.*, *118, Part B*, 161-179

Sandford, S. A., and J. P. Bradley (1989), Interplanetary dust particles collected in the stratosphere: Observations of atmospheric heating and constraints on their interrelationship and sources, *Icarus*, *82*(1), 146-166

Saunders, R. W., S. Dhomse, W. S. Tian, M. P. Chipperfield, and J. M. C. Plane (2012), Interactions of meteoric smoke particles with sulfuric acid in the Earth's stratosphere, *Atmos. Chem. Phys.*, *12*(10), 4387-4398

Saunders, R. W., P. M. Forster, and J. M. C. Plane (2007), Potential climatic effects of meteoric smoke in the Earth's paleo-atmosphere, *Geophys. Res. Lett.*, *34*(16), L16801

Saunders, R. W., et al. (2010), An aerosol chamber investigation of the heterogeneous ice nucleating potential of refractory nanoparticles, *Atmos. Chem. Phys.*, *10*(3), 1227-1247

Saunders, R. W., and J. M. C. Plane (2006), A laboratory study of meteor smoke analogues: Composition, optical properties and growth kinetics, *J. Atmos. Sol.-Terr. Phys.*, *68*(18), 2182-2202

Saunders, R. W., and J. M. C. Plane (2011), A photo-chemical method for the production of olivine nanoparticles as cosmic dust analogues, *Icarus*, *212*(1), 373-382

Scott, R. F., and M. Jones (2006), *Journals: Captain Scott's last expedition*, OUP, Oxford

Siskind, D. E., M. H. Stevens, C. R. Englert, and M. G. Mlynczak (2013), Comparison of a photochemical model with observations of mesospheric hydroxyl and ozone, *J. Geophys. Res.: Atmos.*, *118*(1), 195-207

Solomon, S. (1999), Stratospheric ozone depletion: A review of concepts and history, *Rev. Geophys.*, *37*(3), 275-316

Sorensen, C. (2001), Light scattering by fractal aggregates: a review, *Aerosol Sci. Tech.*, *35*(2), 648-687

Stefanutti, L., L. Sokolov, S. Balestri, A. R. MacKenzie, and V. Khattatov (1999), The M-55 Geophysica as a platform for the airborne polar experiment, *J. Atmos. Ocean. Tech.*, *16*(10), 1303-1312

Stone, D., and D. M. Rowley (2005), Kinetics of the gas phase HO_2 self-reaction: Effects of temperature, pressure, water and methanol vapours, *Phys. Chem. Chem. Phys.*, *7*(10), 2156-2163

Sugimoto, T., A. Muramatsu, K. Sakata, and D. Shindo (1993), Characterization of hematite particles of different shapes, *J. Coll. Interf. Sci.*, *158*(2), 420-428

Summers, M. E., and D. E. Siskind (1999), Surface recombination of O and H_2 on meteoric dust as a source of mesospheric water vapor, *Geophys. Res. Lett.*, *26*(13), 1837-1840

Taesler, I., R. G. Delaplane, and I. Olovsson (1975), Hydrogen bond studies. XCIV. Diaquaoxonium ion in nitric acid trihydrate, *Acta Cryst. Sect. B*, *31*(5), 1489-1492

Taylor, S., J. H. Lever, and R. P. Harvey (1998), Accretion rate of cosmic spherules measured at the South Pole, *Nature*, *392*(6679), 899-903

Taylor, S., G. Matrajt, and Y. Guan (2012), Fine-grained precursors dominate the micrometeorite flux, *Meteorit. Planet. Sci.*, *47*(4), 550-564

Toppani, A., G. Libourel, C. Engrand, and M. Maurette (2001), Experimental simulation of atmospheric entry of micrometeorites, *Meteorit. Planet. Sci.*, *36*(10), 1377-1396

Verronen, P. T., M. E. Andersson, D. R. Marsh, T. Kovács, and J. M. C. Plane (2016), WACCM-D: Whole Atmosphere Community Climate Model with D-region ion chemistry, *J. Adv. Model. Earth Syst.*, *8*, In Press

Verronen, P. T., M. L. Santee, G. L. Manney, R. Lehmann, S. M. Salmi, and A. Seppälä (2011), Nitric acid enhancements in the mesosphere during the January 2005 and December 2006 solar proton events, *J. Geophy. Res.: Atmos.*, *116*(D17), D17301

Voigt, C., et al. (2005), Nitric Acid Trihydrate (NAT) formation at low NAT supersaturation in Polar Stratospheric Clouds (PSCs), *Atmos. Chem. Phys.*, *5*(5), 1371-1380

Voigt, C., et al. (2000), Nitric Acid Trihydrate (NAT) in polar stratospheric clouds, *Science*, *290*(5497), 1756-1758

Vondrak, T., J. M. C. Plane, S. Broadley, and D. Janches (2008), A chemical model of meteoric ablation, *Atmos. Chem. Phys.*, *8*(23), 7015-7031

Weigel, R., C. M. Volk, K. Kandler, E. Hösen, G. Günther, B. Vogel, J. U. Grooß, S. Khaykin, G. V. Belyaev, and S. Borrmann (2014), Enhancements of the refractory submicron aerosol fraction in the Arctic polar vortex: feature or exception?, *Atmos. Chem. Phys.*, *14*(22), 12319-12342

Weisberg, M. K., C. Smith, G. Benedix, L. Folco, K. Righter, J. Zipfel, A. Yamaguchi, and H. C. Aoudjehane (2008), The Meteoritical Bulletin, No. 94, September 2008, *Meteorit. Planet. Sci.*, *43*(9), 1551-1584

Weisberg, M. K., C. Smith, G. Benedix, C. D. K. Herd, K. Righter, H. Haack, A. Yamaguchi, H. C. Aoudjehane, and J. N. Grossman (2009), The Meteoritical Bulletin, No. 96, September 2009, *Meteorit. Planet. Sci.*, *44*(9), 1355-1397

Weiss, F., F. Kubel, Ó. Gálvez, M. Hoelzel, S. F. Parker, P. Baloh, R. Iannarelli, M. J. Rossi, and H. Grothe (2016), Metastable nitric acid trihydrate in ice clouds, *Angew. Chem.*, *55*(10), 3276-3280

Yung, Y. L., and W. B. DeMore (1999), *Photochemistry of planetary atmospheres*, Oxford University Press on Demand, Oxford

Zobrist, B., T. Koop, B. P. Luo, C. Marcolli, and T. Peter (2007), Heterogeneous ice nucleation rate coefficient of water droplets coated by a nonadecanol monolayer, *J. Phys. Chem. C*, *111*(5), 2149-2155

Zolensky, M. E., and D. Lindstrom (1992), Mineralogy of 12 large "chondritic" interplanetary dust particles, in *Lun. Plan. Sci.*, edited, pp. 161-169, Lunar and Planetary Institute, Houston